DISSERTATION

INTERFLOW DYNAMICS AND THREE-DIMENSIONAL MODELING OF TURBID DENSITY CURRENTS IN IMHA RESERVOIR, SOUTH KOREA

Submitted by

Sang Do An

Department of Civil and Environmental Engineering

In partial fulfillment of the requirements

For the Degree of Doctor of Philosophy

Colorado State University

Fort Collins, Colorado

Fall 2011

Doctoral Committee:

Advisor: Pierre Y. Julien

Christopher I. Thornton
Subhas K. Venayagamoorthy
Ellen E. Wohl

ABSTRACT

INTERFLOW DYNAMICS AND THREE-DIMENSIONAL MODELING OF TURBID DENSITY CURRENTS IN IMHA RESERVOIR, SOUTH KOREA

This study reports a detailed research identifying the turbid density flow regimes and propagation dynamics of density currents in Imha Reservoir in South Korea during Typhoon Ewiniar. We employ a high resolution 3-D numerical model (FLOW-3D), based on non-hydrostatic Navier-Stokes equations, to investigate the propagation of density flows resulting from the complicated reservoir morphometry and various mixing processes. The 3-D numerical model was modified to simulate particle-driven density currents. The particle dynamics algorithm builds upon the original FLOW-3D code in two ways: (1) improve the original buoyant flow model to compute the changes in density via particle deposition; and (2) include multiple sediment sizes in mixtures as a function of particle size. The influences of inflow characteristics and seasonal changes of thermal structure of the reservoir on the turbid density currents intruding into Imha Reservoir are studied.

A series of numerical simulations of lock-exchange are validated with laboratory experiments on: (1) gravity currents propagating into a two-layered fluid; (2) gravity currents propagating into a stratified fluid; and (3) particle-driven gravity currents. The model predictions of propagation speed compared very well with laboratory experiments and analytical solutions. Two numerical approaches (Reynolds Averaged Navier-Stokes model and large-eddy simulation) are equally effective and robust in predicting propagation speed and interfacial instability compared to the laboratory experiments. The simulation of gravity currents intruding into a stratified fluid matched the theoretical solution derived from an energy model. The modified FLOW-3D model successfully captured the decreasing propagation speed due to the different deposition rates of

different particle sizes, compared to experimental measurements. We extended our simulations to include the effects of particle sizes on the propagation dynamics of gravity currents. The type of gravity currents depends on particle sizes and can be subdivided into three zones: (1) When d_s is less than about $10\,\mu\mathrm{m}$, the particle-driven gravity currents behave like IGC (Intrusive Gravity Currents) and all sediments can remain in suspension. Thus the suspended sediments can increase the density of the currents enough to travel a longer distance; (2) When $d_s > 40\,\mu\mathrm{m}$, particles will rapidly settle, resulting in a decrease in excess density of the gravity currents. So, such density currents lose their momentum quickly and rapidly vanish; and (3) When $10\,\mu\mathrm{m} < d_s < 40\,\mu\mathrm{m}$, some particles will settle quickly, but others remain suspended for a long time, affecting the propagation dynamics of the currents. Modeling gravity currents in this regime particle sizes must account for particle dynamics and settling.

We applied the FLOW-3D coupled with the particle dynamics algorithm to Imha Reservoir in South Korea. The model application was validated against field measurements during Typhoon Ewiniar in 2006. In the field validation, absolute mean error (AME) and root mean squared error (RMSE) for the prediction in water temperature profiles were calculated to be 1.0 ^{o}C and 1.3 ^{o}C, respectively. For turbidity predictions, AME and RMSE were 37 and 47 NTU (nephelometric turbidity units) between the simulated and the measured turbidity at stations G3, G4, and G5.

We showed the influence of inflow characteristics (discharge, temperature, sediment concentration, and particle size distribution) on the fate of density currents in Imha Reservoir. Two threshold values in particle size ($10\,\mu\mathrm{m}$ and $40\,\mu\mathrm{m}$) were identified, consistent with previous findings from the simulations of Gladstone's experiments. The simulations indicate that when the particle sizes d_s are less than $10\,\mu\mathrm{m}$, most of the sediment inflows at the inlet point (G2) will be transported to Imha Dam (G4) in suspension by interflows. When the particle sizes d_s are greater than $40\,\mu\mathrm{m}$, they will rapidly settle before reaching the dam. Therefore, highly concentrated turbid interflows could only occur when d_s is less than the threshold value of $10\,\mu\mathrm{m}$. The numerical

results also present three flow regimes determining the intrusion types of density currents: (1) river inflows will form interflows when the sediment concentration C_i is less than 2000 mg/l; (2) when C_i is between 2000 mg/l and 3000 mg/l, they will form multiple intrusions (i.e., interflows and underflows); and (3) when C_i is greater than 3000 mg/l, they will plunge and propagate as underflows. These threshold values (2000 mg/l and 3000 mg/l) can be used to practically predict the formation of turbid density currents, flow type, and intrusion level in Imha Reservoir.

ACKNOWLEDGEMENTS

This dissertation could not have been completed without the support of many people. I would like to thank these individuals for their help and support. First of all, I would like to express my deepest gratitude to my advisor, Professor Julien for his great guidance and encouragement during my years at CSU. He showed faith in me whenever I doubted my ability to complete my research on time. I feel honored to have had a change to study under Dr. Julien. I also would like to thank my committee members. I extend special thanks to Dr. Venayagamoorthy. Although his demands were challenging, his great guidance helped me achieve fantastic results. I am deeply grateful to Dr. Thornton. I could improve my research with the engineering knowledge that I gained from him. I am very grateful to Dr. Wohl for the large amount of time she put in to improve my dissertation writing.

I would like to extend my appreciation to the K-water (Korea Water Resources Corporation) for offering the opportunity to study at CSU and providing financial support during the years. Special thanks to Drs. Jinsoo Kim, Youngjin Kim, Taesang Ryu, Byoungdong Oh, and Myeonggi Park for their support and faith in me.

I want to extend thanks to friends and colleagues; Jaehoon, Hyeyun, Jungkyu, Kyungseop, Kiyoung, Jazuri, and Shazwani for their friendship.

Finally, I would like to extend my deepest gratitude to my family. To my lovely wife, Younkyung and my two little boys, Seongho and Juneho. Without their love and encouragement, I could not have finished this dissertation. I also want to share this delight with all friends whom I met in Fort Collins.

TABLE OF CONTENTS

List of Figures

List of Tables

Chapter 1

Introduction

1.1 Motivation

As shown in Figure 1.1, flood-induced density currents that contain high sediment concentrations have recently been observed in many reservoirs of South Korea. The number of reservoirs experiencing turbidity problems has been rising due to the increase of rainfall intensity and frequency (Yum *et al.* 2008).

(a) Downstream of Soyang Reservoir (2006) (b) Imha Reservoir (2003)

Figure 1.1 (a) Discharge of highly turbid water during Typhoon Ewiniar 2006 at downstream of Soyang Reservoir; (b) High turbidity surface water downstream of Imha Reservoir during 2003 Typhoon Maemi.

High turbidity inflows into a reservoir pose many problems. Turbid waters may contain organic particles harboring bacteria or viruses that may induce waterborne diseases. Thus, the highly concentrated turbid waters require additional costs. The fact that the disinfectants can form unintended byproducts that threaten the safety of drinking water has been drawn public attention

to water quality. Furthermore, the very fine particulate sediments, which are included in the turbid water, limit the penetration of light into a reservoir by scattering (Kirk 1985). This affects the aquatic plants' ability to photosynthesize. Less light results in degrading the habitat for invertebrates, amphibians and fish (Henley *et al.* 2000). On the other hand, if turbid waters enter a reservoir with highly concentrated phosphorus and nitrogen, they may cause eutrophication, which deteriorates water quality (Smith *et al.* 1999). Long-term discharge of turbid waters downstream of reservoirs can cause environmental damages including fish mortality and the reduction of aquatic organisms (Crosa *et al.* 2009).

The dynamics of turbid density currents in a reservoir is a complex phenomenon affected by many factors: sediment concentration, temperature, reservoir thermal stratification, discharge, etc. (Fernandez and Imberger 2006). Generally, the turbid density currents are triggered by severe flood events during summer. After major rainfall events, the tributary inflows typically reach 17 ^{o}C ~ 18 ^{o}C in temperature, and include sediments transported from the watersheds (Ford and Johnson 1983). The low water temperature and high sediment concentration contribute to the density of inflowing water. If a receiving reservoir is warm and clear, the turbid inflows usually plunge, and then propagate as a density current along the hypolimnion (i.e., the bottom layers that consist of the denser and colder water), moving along the bottom as underflows. By contrast, when the tributary inflows are warmer than the receiving reservoir, water rises to the surface of the reservoir and propagates as overflows. On the other hand, when the receiving reservoir becomes thermally stratified, the turbid inflows may intrude into the metalimnion (i.e., the thermal gradient layers between the epilimnion and the hypolimnion) as interflows (see Figure 1.2; Ford and Johnson 1983), which is the subject of this dissertation.

The flow pattern of turbid density currents is determined by their dynamics, varying in response to the characteristics of turbid inflows and a receiving reservoir. These characteristics include variable stratification, sediment particle size, unsteady tributary inflows, and river morphology (Ford and Johnson 1983; Chung *et al.* 2009).

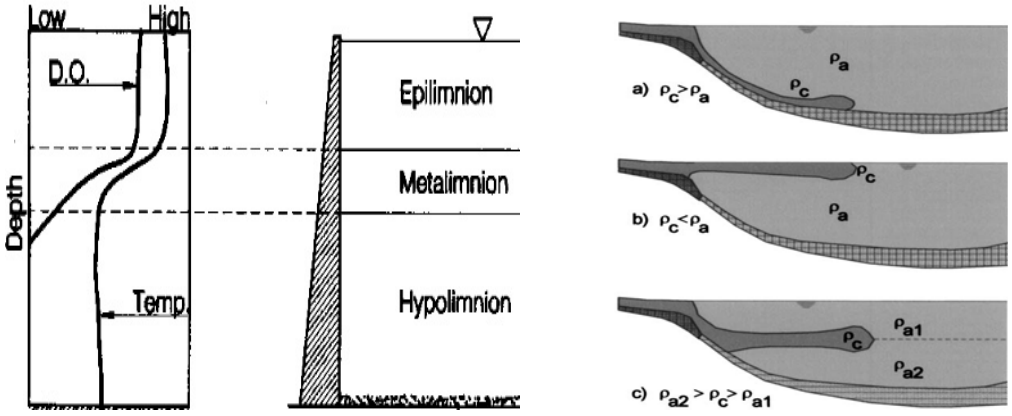

Figure 1.2 Possible density flow patterns depending on the density of the inflowing water relative to the vertical stratification structure of a reservoir; (Left) Typical thermal stratification in summer; (Right) the density of inflowing water ρ_c in a unstratified reservoir (ρ_a) and in a reservoir stratified from (ρ_{a1}) to (ρ_{a2}) in form of a) underflow, b) overflow, and c) interflow (from Cesare *et al.* 2006; Morris and Fan 1998).

The complex dynamics of turbid density currents has drawn considerable engineering interest for many years. Early studies were focused on analytical research and experimental studies. Ellison and Turner (1959) contributed to the theory and physical understanding of density currents through laboratory experiments. Turbid density currents occur in many countries: USA (Effler *et al.* 2006), Japan (Chikita and Okumura 1990; Liu and Lou 2005), Taiwan (Chen *et al.* 2006), and South Korea (Chung *et al.* 2009). Thus, the many experiments focused on the turbid density currents in reservoirs. The results from the experimental and mathematical studies inspired the development of numerical models for the propagation and mixing of density currents.

Many numerical simulations of the density currents have been carried out with one- or two-dimensional models due to fast simulation runtime and fewer data for the model setup. The three-dimensional models have recently attracted attention due to their better physical representation of complex reservoir geometries. Several three-dimensional models have been documented. They have been applied to water quality simulations, providing physical understanding on a full seasonal limnological process in a reservoir.

In South Korea, Imha Reservoir has suffered from long flood-induced high turbidity currents since 2002. The highest turbidity values were recorded during Typhoon Rusa in 2002 and Maemi in 2003 with 880 NTU and 1200 NTU, respectively. The successive highly concentrated turbid inflows and the long detention time in the reservoir affect phytoplankton community, ichthyofauna and fish growth (Ardjosoediro and Ramnarine 2002; Han *et al.* 2007; Shin *et al.* 2009).

Several actions were taken to reduce the reservoir turbidity. The first countermeasure focused on erosion control in the watershed. The erosion control began with a closer look at highly erodible sources: upland farming areas, construction sites, and unvegetated slopes. Real-time gauging stations were installed at five stations to monitor the propagation of turbid density currents. A selective withdrawal method can be applied to the rapid release of the turbid water at a different layer efficiently after flood events (Morris and Fan 1998). As such, the intake tower of Imha Dam was remodeled into a selective withdrawal type in 2006. The intake tower was initially designed and constructed as a surface withdrawal type for supplying warm water to downstream irrigation land, and thus could protect crops from freeze damage. Operating conditions for a selective intake tower should vary by the change of stratification, the patterns of turbid density currents, and the characteristics of the runoff events (Gelda and Effler 2007). These complex impacts on the turbid density currents make it more difficult to establish typical operation rules for the selective withdrawal facilities.

1.2 Research Objectives

This study employs a three-dimensional numerical model for the simulation of turbid density currents horizontally propagating into a morphologically complex reservoir. This model will provide improved three-dimensional predictions in temporal and spatial evolutions with the

longitudinal dispersion and the lateral mixing in meander loops. The objectives of this research are summarized as the following:

1. Test and compare a numerical model with laboratory experiments. The numerical code, FLOW-3D was selected for density currents propagating into: (1) a two-layered fluid; and (2) a stratified fluid. The performance ability of the numerical model in predicting the propagation speed will be justified by comparing with laboratory experiments and analytical solutions. Here two numerical approaches (RANS and LES) will be explored to find an efficient and robust numerical method for the turbulence simulation of density flows.
2. Develop a particle dynamics algorithm which can be coupled with the FLOW-3D model for the simulations of particle-driven gravity currents.
3. Apply and validate the numerical model to Imha Reservoir.
4. Develop analytical solutions for practical predictions of the intrusive speed and intrusion depth of turbid density currents propagating into Imha Reservoir. Also develop a parametric analysis on the influence of: (1) sediment particle size; (2) sediment concentration; and (3) reservoir stratification on the fate of density currents in Imha Reservoir.

Chapter 2

Literature Review

2.1 Fundamentals of Density Currents

Turbid density currents occur as a result of inflow momentum and buoyant forces caused by density differences between tributary inflows and receiving reservoir waters. Figure 2.1 shows a general turbid density flow pattern induced by a severe rainfall event in a large reservoir of South Korea.

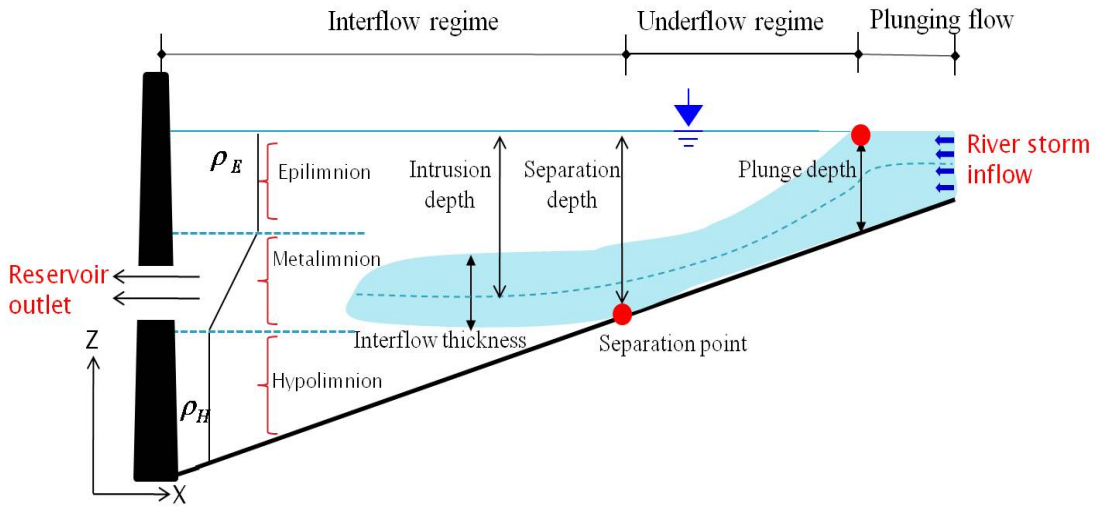

Figure 2.1 Density flow regimes of flood-induced turbidity flows in a stratified reservoir.

Large tributary inflows during heavy rainfall events may be generally denser than the receiving water of the reservoir because the inflows may have large suspended sediments and relatively colder temperature than that of the reservoir.

The denser inflows will push the ambient water ahead until the buoyant forces become dominant. The negative buoyancy force will lead them to plunge down to the reservoir bottom at the plunge point determined by the balance between the momentum of the inflow and the baroclinic pressure caused by the difference in density between the ambient water and the inflows (Alavian *et al.* 1992; Gu *et al.* 1996). After the plunge point, the flows will propagate as underflows. Theoretically, the propagation speed of the underflow can be calculated using the momentum equation in two layered flows (similar to the open channel flow theory) with the additional buoyancy force. If a reservoir is stratified, the underflow may leave the river bottom and intrude into the reservoir body (e.g., metalimnion) from the elevation where the density of the underflow is equal to that of the water layer of the reservoir (i.e., at the level of neutral buoyancy). The more detailed description on the basics for density currents can be found in the research of Alavian *et al.* (1992), Ford and Johnson (1983), and Fischer *et al.* (1979).

2.1.1. Basic Definitions

This section describes the physical properties of gravity currents. We present several dimensionless parameters frequently used to provide important quantitative information on the turbid density flows.

Density

The densities of gravity currents can be defined as a function of temperature and sediment concentration. Gill (1982) proposed the formulation for the density variation due to temperature change in Equation (2.1). If the density increases due to adding sediments into water, total density can be defined as Equation (2.2).

$$\rho_w(T) = 999.8452594 + 6.793952\times10^{-2}\,T_w - 9.0952902\times10^{-3}\,T_w^2 + 1.001685\times10^{-4}\,T_w^3 - 1.120083\times10^{-6}\,T_w^4 + 6.536332\times10^{-9}\,T_w^5 \quad (2.1)$$

$$\rho_m = \rho_w(T)\left[1 + (G-1)\,C_v\right] \quad (2.2)$$

where T = water temperature °C ; $\rho_w(T)$ = water density at the temperature T ; ρ_m = mixture density; G = he specific gravity of a sediment particle; and C_v = volumetric sediment concentration. We can estimate the density of the inflow entering into the reservoir using the Equations (2.1) and (2.2). Table 2.1 shows temperature of clear water having an equivalent density to the water mixture depending on sediment concentration.

Table 2.1 Density of mixture water depending on temperature and sediment concentration.

Temp °C	Clear Water Density (kg/m^3)	Sediment Concentration (mg/*l*)					
		100	250	1000	2500	5000	10000
		Mixture Density (kg/m^3)					
4	999.978	1000.04	1000.13	1000.60	1001.53	1003.09	1006.20
5	999.969	1000.03	1000.13	1000.59	1001.53	1003.08	1006.20
10	999.705	999.77	999.86	1000.33	1001.26	1002.82	1005.93
15	999.104	999.17	999.26	999.73	1000.66	1002.22	1005.33
20	998.209	998.27	998.36	998.83	999.77	1001.33	1004.44
25	997.051	997.11	997.21	997.67	998.61	1000.17	1003.29
30	995.654	995.72	995.81	996.28	997.21	998.78	1001.90

Density stratification

The density structure of a water body plays an important role in density current dynamics. Density currents generally form due to a density difference between density current (ρ_d) and ambient water (ρ_a). Boussineq flows state that the density differences are sufficiently small (usually less than 3%) to neglect inertia (i.e., for fluid acceleration). A densimetric gravitational acceleration results from the difference in specific weight between the density flows and ambient

waters ($g\,\Delta\rho$ where $\Delta\rho = \rho_d - \rho_a$). The specific weight difference (also called buoyancy) per unit mass ($g\,\Delta\rho / \rho_d$) can be expressed as a reduced gravitational acceleration ($g' = g\,\Delta\rho / \rho_d$).

If an ambient fluid is stably stratified, the density stratification is described by the profile $\rho_a(z)$ as shown in Figure 2.2. The density increases linearly downwards as defined by

$$-\,g\,\frac{d\rho_a}{dz} = \text{constant} \tag{2.3}$$

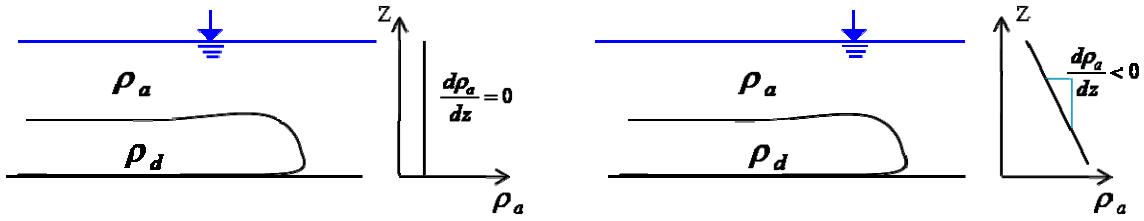

(a) Unstratified ambient fluid (b) Stratified ambient fluid

Figure 2.2 Sketch of density variation in a stratified and unstratified ambient fluid.

Considering gravity currents propagating in a stratified ambient fluid, the gravity currents will oscillate in simple harmonic with angular frequency (Turner 1979) defined with

$$N = \left(-\frac{g}{\rho}\frac{\partial \rho}{\partial z} \right)^{1/2} \tag{2.4}$$

This indicates the frequency referred to Brunt-Väisälä frequency or simply the buoyancy frequency.

Richardson Number

Richardson (1920) proposed a dimensionless number that expresses the ratio of the square of buoyancy frequency (N) to the square of velocity gradient. Thus, the gradient Richardson number is defined as

$$Ri = \frac{N^2}{\left(\frac{\partial u}{\partial z}\right)^2 + \left(\frac{\partial v}{\partial z}\right)^2} = \frac{-\frac{g}{\rho}\frac{\partial \rho}{\partial z}}{\left(\frac{\partial u}{\partial z}\right)^2 + \left(\frac{\partial v}{\partial z}\right)^2} \tag{2.5}$$

The gradient Richardson number Ri can be used to determine the dynamic instability of the flow. The laboratory results showed that flow becomes unstable due to the dynamic instability when $Ri < Rc$ where Rc is a stability threshold value, $Ri \approx 0.25$ (Geyer and Smith 1987; Miles 1961; Miles and Howard 2006; Taylor 1931).

In addition, the overall Richardson number (or bulk Richardson number, Ri_o) is defined as the ratio of buoyancy to kinetic energy of inflows. A large overall Richardson number Ri_o means that the buoyancy becomes dominant, resulting in less mixing across the interface between turbidity currents and ambient flows. It can be expressed using the scales of length L and velocity U.

$$Ri_o = \frac{g^{'}L}{U^2} \tag{2.6}$$

where g' = a reduced gravitational acceleration ($g' = g\Delta\rho/\rho_d$); $\Delta\rho$ = the density difference between the density current and ambient water ($\Delta\rho = \rho_d - \rho_a$); and L = generally vertical length scale, generally indicates water depth h.

Densimetric Froude Number

The densimetric Froude number is similar to the Froude number. The densimetric Froude number is the inverse square root of Ri_o.

$$F_o = \frac{U}{(g^{'}L)^{1/2}} \tag{2.7}$$

The ratio also explains the relationship between the gravitational forces resisting mixing to the inertial forces of the flow.

2.1.2. Role of Buoyancy

The effects of buoyancy forces which arise as a result of the density difference between density currents and ambient water were investigated by Turner (1979) and Alavian *et al.* (1992). The buoyant forces play a crucial role in both determining the propagation speed and depth of the density current. Figure 2.3 shows the gravity current propagating on a sloping bottom. On an inclined surface, the g' can be divided with two components (i.e., $g' \sin\theta$ and $g' \cos\theta$), where θ is the slope angle. The component $g' \sin\theta$ is the force driving the current down a slope. It means that the propagation speed of the density current is proportional to its density. When the component $g' \sin\theta$ is balanced by bottom boundaries and interfacial shears, the underflow becomes uniform. The other component $g' \cos\theta$ is related with the hydrostatic pressure gradient perpendicular to the interface relevant to interfacial mixing.

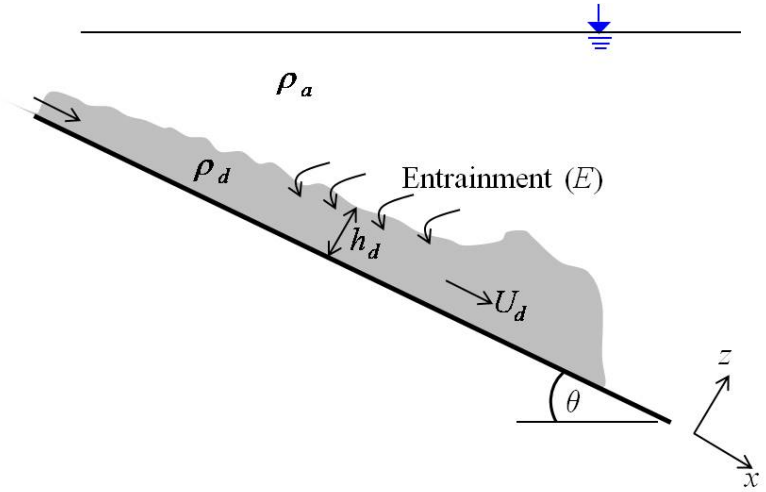

Figure 2.3 Sketch of a gravity current on a slope (from Turner 1979).

The turbulence across the interface brings mixing, and thus causes clear water entrainment into the density current from the upper zone. Turner (1979) used the overall Richardson number Ri_o for a measure of the stabilizing effect of the density gradient relative to the shear. Ri_o can be defined as

$$Ri_{\mathrm{o}} = \frac{g' h_d \cos\theta}{U_d^2} \tag{2.8}$$

where U_d = mean velocity and h_d = the depth of a gravity current.

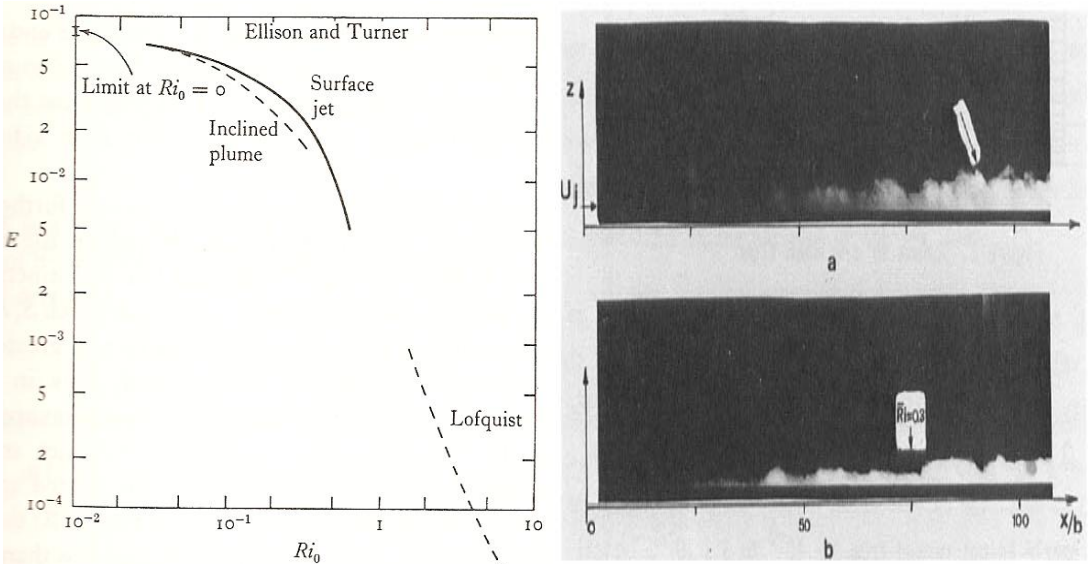

Figure 2.4 (Left) Rate of entrainment into a turbulent stratified flow as a function of overall Richardson number (from Ellison and Turner 1959); (Right) the side views of the mixing zone of jet plumes (using smoke for visualization), (a) neutral with Ri_o = 0.0, (b) stratified with Ri_o = 0.3 (from Hopfinger 1978).

Ellison and Turner (1959) and Lofquist (1960) plotted experimental results for the entrainment parameter E as a function of the overall Richardson number Ri_{o} in Figure 2.4. Figure 2.4 (left) demonstrates that a larger Ri_{o} induces less entrainment across the interface between the turbidity current and the ambient flow. It is well known that a large Ri_o suppresses interfacial turbulence inducing mixing. Hopfinger (1978) empirically investigated buoyancy effects and concluded that a stratified flow suppresses the growth of the turbulent layer compared to a neutral flow (Figure 2.4, right). Alavian *et al.* (1992) concluded that this buoyancy has a double role in both accelerating the propagation speed and destabilizing by one component g' sin θ and turbulence damping and stabilizing by the other component g' cos θ. Fernandez and Imberger (2006) also reported that the

entrainment parameter E in underflows is governed by a balance between drag forces, buoyancy forces, and Richardson number.

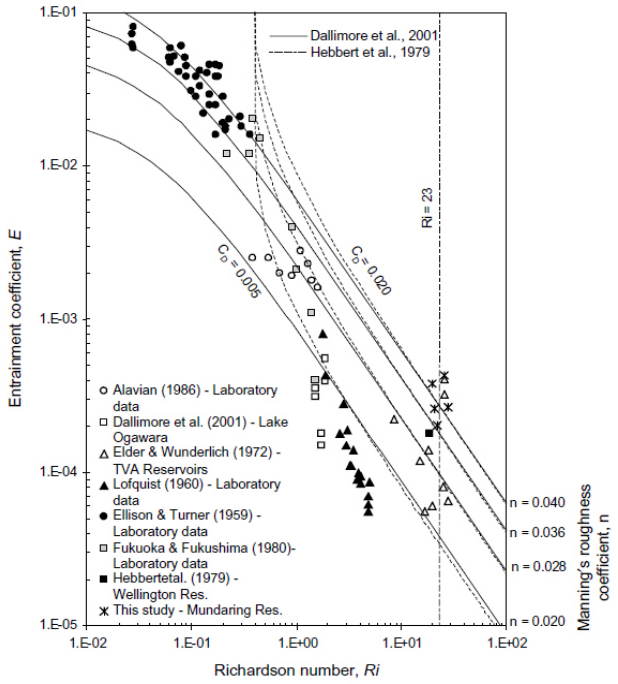

Figure 2.5 The Entrainment coefficient (*E*) as a function of Richardson number (*Ri*) plotting with previous study results (from Fernandez and Imberger 2006).

2.1.3. Density Variation by Sediments Deposition

The effects of sediments on density variation are more complicated than that of temperature due to variations of sediment concentration, resulting from deposition via particle settling (Gladstone and Pritchard 2010; Hürzeler *et al.* 1996) and sediment entrainment via erosion at a bottom (Parker *et al.* 1987). Parker *et al.* (1987) carried out several experimental tests on turbidity currents and observed that the sediment entrainment and water entrainment depend on the Richardson number. Hürzeler *et al.* (1996) observed that reversing buoyancy gravity currents can occur if there is a loss of substantial sediments. Gladstone and Pritchard (2010) confirmed dense underflows are able to change into overflow after sufficient deposition of sediment particles.

Figure 2.6 shows the laboratory experiments of Gladstone *et al.* (1998). They showed that the propagation dynamics of particle-driven gravity currents (PDGC) were strongly influenced by the size of particles. They carried out a series of experiments using mixtures containing two sizes of silicon carbide particles (25 μm and 69 μm). Their experiments showed that gravity currents driven by fine particles traveled faster and further than gravity currents driven by coarse particles.

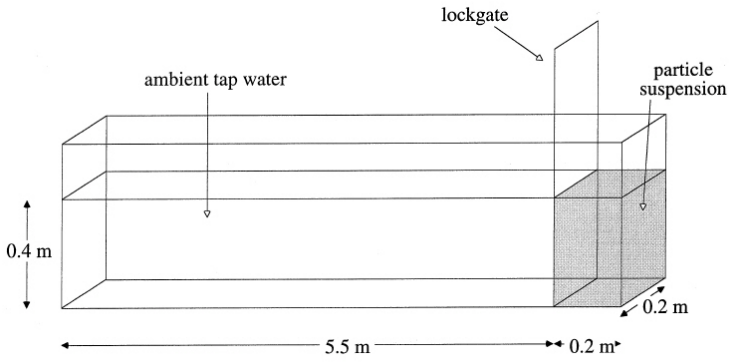

Figure 2.6 A simplified diagram of the experiments of Gladstone *et al.* (1998).

Although we know that particle deposition may affect the dynamics of turbid density currents in a reservoir, it is very difficult to apply a particle settling effect to a reservoir simulation. The tributary inflows causing density currents in a reservoir contain time-varying sediment inflows with different particle size distributions. In theory, the settling velocity for each particle can be calculated using Stokes' Law. However, the applicability of the formulations for determining settling velocity is still questionable, because many other factors (e.g., turbulence, stratification) can influence the settling velocity.

2.1.4. Effects of Density Stratification

Yick *et al.* (2009) presented a combined experimental and numerical investigation of particle settling in a linearly stratified fluid at low Reynolds numbers. They observed that stratification influenced particle settling by increasing drag and suggested a new formula for the drag coefficient in a salt-stratified fluid.

$$C_D = \left(\frac{12}{Re} + \frac{6}{1+\sqrt{2Re}} + 0.4 \right) (1 + \alpha \, Ri_v^{1/2}) \qquad (2.9)$$

where $\alpha = 1.9$; $Re = \omega_s d_s / \nu$; and Ri_v = the viscous Richardson number defined as

$Ri_v = d_s^3 N^2 / (\omega_s \nu)$.

K-water (2004) carried out the study on the effectiveness of flocculants to prompt particle settling. The study observed that the particle settling accelerated by flocculation was retarded when the particles enter into the thermocline, which is a stratified layer. Even after 6 hours, the particles were observed not to fall down (see Figure 2.7). They concluded that the injection of the flocculants could accelerate settling velocity of turbidity particles in a reservoir. However, the acceleration by flocculants could be limited by strong stratified layers of a reservoir.

(a) (b) (c) (d)

Figure 2.7 An experiment on the particle settling influenced by a thermal stratification; (a) 1hour later after turbidity mixing, (b) after 6 hours, (c) after 24 hours, (d) initial thermal stratification (K-water 2004).

Quay *et al.* (1980) investigated vertical diffusion rates by tritium tracer experiments in the thermocline and hypolimnion of two sampling lakes, located in northwestern Ontario. The value of vertical diffusion rates (K_z) was estimated to be 5×10^{-5} cm^2/s and 8×10^{-4} cm^2/s in the thermoclines. In the hypolimnion, K_z was determined to be 1.7×10^{-3} cm^2/s and 1.8×10^{-2} cm^2/s. It was 20 ~ 30 times greater than those in the thermocline. They also found that the vertical diffusion rates of mass

and heat were different. The heat is diffusing vertically faster than mass in the thermocline and at more similar rates in the hypolimnion. The experiments also showed that the vertical diffusion rate (K_z) has an inverse proportionality to the square of buoyancy frequency.

2.2 Analysis of Density Currents

2.2.1 Overflow

Overflow happens when the tributary inflows have a lighter density than that of ambient reservoir water. Several research topics relevant to the overflow can be found in the literature. Overflow can be generally induced by the intrusion of lighter fluid flows (e.g., an oil spill, a thermal effluent). Elder and Wunderlich (1972) investigated the overflows in the reservoirs of the Tennessee Valley Authority system using tracer techniques. Johnson and Merritt (1979) observed that the inflows from the upstream Colorado River formed overflow density currents and propagated into Lake Powell during a summer stratification period (July-September). They also observed underflows by cold inflows during the winter. Adams *et al.* (1975) and Safaie (1979) reproduced overflows using thermal discharges. Harleman and Stolzenbach (1972) developed a theoretical model to predict the overflows caused by a heated discharge from power generation. Oil slicks have been also studied as a phenomenon of density overflows (Van Houten 1976; Wilkinson 1972). When analyzing overflows usually three factors: namely separation point, depth, and propagation speed are considered to be important, shown in Figure 2.8.

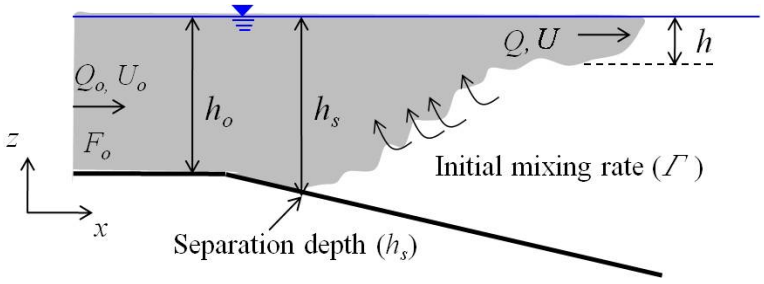

Figure 2.8 Buoyant surface jet over sloping bottom (from Fleenor 2001).

Inflows lighter in density than the receiving water body will propagate and push the ambient water of the water body until the inflows become dominated by buoyancy forces and will finally go up to the top of the surface of the receiving water body at a separation point. Safaie (1979) studied surface density plumes discharged horizontally over a sloping bottom. An empirical equation for the separation depth (h_s) was presented by the study.

$$h_s = 0.914\, h_s (F_{\mathrm{o}})^{1/2} \tag{2.10}$$

where h_s = separation water depth; h_o =inflow depth; and F_{o} = the inflow densimetric Froude number, defined as

$$F_{\mathrm{o}} = \frac{U_{\mathrm{o}}}{(g' h_{\mathrm{o}})^{1/2}} \tag{2.11}$$

where U^{o} = inflow velocity and g' = the reduced gravitational acceleration $(g\Delta\rho/\rho_a)$, where $\Delta\rho$ is the density difference between density current and ambient ($\Delta\rho = \rho_a - \rho_d$). Equation (2.10) also shows that if F_{o} is smaller than the value of 1.2, then h_{s} will be lower than h_{o}. This means that the separation point moves up into the inflowing tributary river, which looks likes a salt wedge in an estuary. The value of the local densimetric Froude number at the separation point was estimated to be 2.5 through the experimental tests.

Safaie (1979) used the source densimetric Froude number, $F_{\mathrm{o}}(\mathrm{A})$, to find a critical value for the overflow occurrence. In the study, no jet attachment was observed when the source densimetric Froude number was less than 2.5. The source densimetric Froude number is defined as

$$F_{\mathrm{o}}(\mathrm{A}) = \frac{U_{\mathrm{o}}}{(g' \mathrm{A}_{\mathrm{o}}^{1/2})^{1/2}} \tag{2.12}$$

where $\mathrm{A}_{\mathrm{o}} = h_{\mathrm{o}} \cdot W$ and W = river width. He developed an equation for the initial mixing at the separation point using the source densimetric Froude number. The dilution rate is defined as the flow discharge after separation point divided by the flow discharge before separation point.

$$\Gamma = \frac{Q}{Q_o} = \left\{1 + \left(\frac{F_o^2(\mathrm{A}) - 6.25}{5.22F_o - 6.25}\right)\left(\frac{h^2}{h_o^2} - 1\right)\right\}^{1/2} \tag{2.13}$$

where Γ = dilution rate in the overflows; Q_o = inflow discharge; and Q = overflow discharge.

Stigebrandt (1978) observed the same phenomenon, the separation point moves up into the inflowing tributary river, under these conditions (i.e., $F_o < 1.0$). He indentified the flow patterns during winter, especially ice-covered periods. The flow patterns depend on the densimetric Froude number and the geometry of a river mouth when the river water is warmer than the surface water in a lake (i.e., the river water is lighter than the lake, see Figure 2.9).

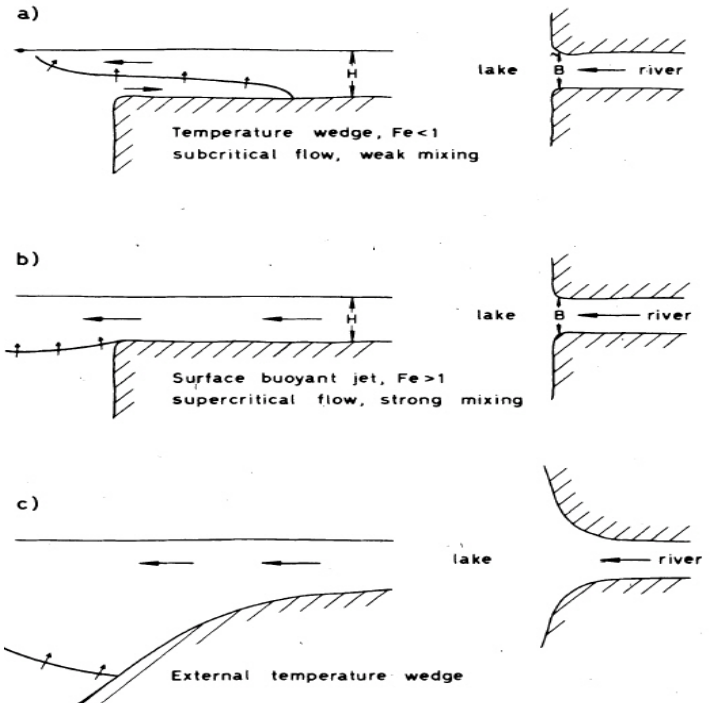

Figure 2.9 Outline of different dynamical possibilities when a river meets a lake. Density of the river water is less than that of the lake water (from Stigebrandt 1978).

If $F_o < 1.0$, the lake water will intrude up into the inflowing river. This phenomenon looks like the salt wedge in an estuary and can be regarded as a temperature wedge. If $F_o > 1.0$, the river water will propagate into the lake like a jet without the intrusion of the lake water into the river. It

is known that the mixing in the temperature wedge pattern is less than in the surface buoyant jet. Stigebrandt (1978) discussed the separation of the inflows when the river inflows enter a lake along geometrically smooth boundaries. He called this phenomenon the external temperature wedge.

Koh (1976) studied gravitational spreading flows induced by the two dimensional continuous releases. He obtained the propagation speed U_d for the flow assuming shear is small.

$$U_d = \frac{L_s}{t} = \left(\frac{\frac{6}{\pi} g' q_o}{1 + \frac{3}{2} C_p} \right) \tag{2.14}$$

where L_s = overflow length; t = time scale; C_p = coefficient to account for non-hydrostatic pressure distribution; and q_o = unit discharge. He considered the water effluent warmer than ambient water and characterized the overflow by an inflow densimetric Froude number (F_o). He proposed the velocity of the overflow density current is a function of the inflow densimetric Froude number and the inflow velocity.

$$U / U_d = 2^{1/3} (F_o)^{-2/3} \tag{2.15}$$

where U = inflow velocity and U_d = overflow propagation speed. When we try to use these equations for predicting the overflow, we have to use these equations with caution. Although the heat transfer from a surface and wind-driven vertical mixing can affect the movement of overflow, the equations neglect those kinds of effects. Overflows containing high turbidity have not been observed in deep reservoirs of South Korea since the turbid density currents generally occur during summer stratification and the density of river inflows is heavier than that of the reservoir epilimnion. Thus, they may form interflows or underflows in the reservoir.

2.2.2 Plunging Point and Underflow

When the inflow is denser than the receiving water of a reservoir, the inflow will plunge and propagate across the reservoir bottom (Simpson 1987). The location of the plunging point is determined by the relationship between the inflow momentum, the buoyancy force (resulting from the pressure gradient across the interface dividing the inflow from the reservoir water), and other forces (e.g., shear forces at bottom, surface, and interface). After the inflow passes the plunging point, the density flow moves down to the bottom and propagates as an underflow. Morris and Fan (1998) provided a general description of an evolution of the density current to become underflows (Figure 2.10).

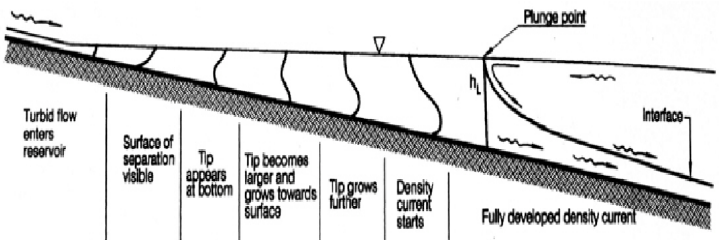

Figure 2.10 Transition from homogeneous flow to density currents (Morris and Fan 1998).

Plunging Point

For the past several decades, many researchers have attempted to determine the plunging location using experimental and theoretical approaches (Akiyama and Stefan 1984; Dai *et al.* 2009; Farrell and Stefan 1988; Hauenstein and Dracos 1984; Hebbert *et al.* 1979; Jain 1981; Lee and Yu 1997; Parker and Toniolo 2007; Savage and Brimberg 1975). Most of the formulas predict the plunge location by calculating plunge depth, which can be expressed as a general form:

$$h_p = \left(\frac{1}{F_p^2}\right)^{1/3} \left(\frac{q_o^2}{g'}\right)^{1/3} \tag{2.16}$$

where h_p = the hydraulic depth at the plunge point; F_p = densimetric Froude number at the plunge point; q_o = unit discharge for rectangular channel. The experimental results conducted by the investigators showed that the plunging flow occurs at the value of F_p ranging from 0.3 to 0.78 for a mild slope. Singh and Shah (1971) carried out experimental studies using a tilting flume and found $F_p = 0.67$, which was also confirmed by Lee and Yu (1997) and Farrell and Stefan (1986). Savage and Brimberg (1975) concluded that the plunge flow occurred at average, $F_p = 0.5$. Lee and Yu (1997) showed that the plunge point can migrate downstream with time to reach to stable condition ($F_p = 1.0$ at initial plunging position, and $F_p = 0.6$ at stable position).

Akiyama and Stefan (1984) summarized equations proposed by several investigators for determining the plunge depth. Some equations considered the effects of ratio of interfacial to bed friction ($\alpha = f_i / f_b$), bed friction, and dilution coefficient (λ), on the plunge depth. When we use Equation (2.16) to predict a plunging location in a reservoir, we have to know about two important things. First, h_p is a hydraulic depth calculated by dividing a cross sectional area by reservoir width. It does not mean the average or maximum water depth. Second, the Equation (2.16) was derived for a constant width channel. However, the width of most reservoirs is significantly variable. Therefore, Equation (2.16) might not be accurate for determining the plunge depth for a reservoir. Furthermore, the fact that density currents vary depending on time and space poses a question for applicability of the equation to a reservoir.

Propagation Speed

Von Kármán (1940) first derived a formula for the propagation speed of a front of a steady density flow. He used Bernoulli's equation, assuming a perfect fluid and irrotational flow to get.

$$U_d = \sqrt{2g'h_d} = 1.41\sqrt{g'h_d} \tag{2.17}$$

where U_d = the propagation speed of density flow and h_d = the depth of density flow.

Laboratory experiments were carried out for the front speed of the density flow moving along a horizontal surface (Middleton 1966a). The propagation speed can be defined as a general form:

$$U_d = C\sqrt{g' h_d} \tag{2.18}$$

Benjamin (1968) investigated the value of C based on inviscid-fluid theory. He showed the importance of the fractional depth (h_d / H), where the H is a total water depth and the H_d is the depth of the density current. Considering the energy-conserving flow, he obtained the formula predicting the propagation velocity as a function of the fractional depth (h_d / H).

$$C = \frac{U_d}{\sqrt{g' h_d}} = \left(\frac{(H - h_d)(2H - h_d)}{H(H + h_d)} \right)^{1/2} \tag{2.19}$$

The maximum value of C is given when the h_d / H approaches zero. On the other hand, the value of C decreases with increasing the h_d / H. When the h_d / H is 0.5, C approaches $1/\sqrt{2}$. The value of C ranges from $\sqrt{2}$ to $1/\sqrt{2}$ when the h_d / H increases from 0 to 0.5.

$$U_d = (\sqrt{2} \sim 1/\sqrt{2})\sqrt{g' h_d} \tag{2.20}$$

Keulegan (1957) studied the motion of saline water from locks into horizontal fresh water channels (see Figure 2.11). He suggested the relation between the velocity of a density current head (U_f) and the depth of the flow head (d_2).

$$U_f = 0.76\sqrt{\frac{\Delta\rho}{\rho_m} g d_2} \tag{2.21}$$

where $\Delta\rho =$ the excess of density of the density current head, $\rho_m =$ the average value of the densities, and $d_2 =$ the max depth at the head.

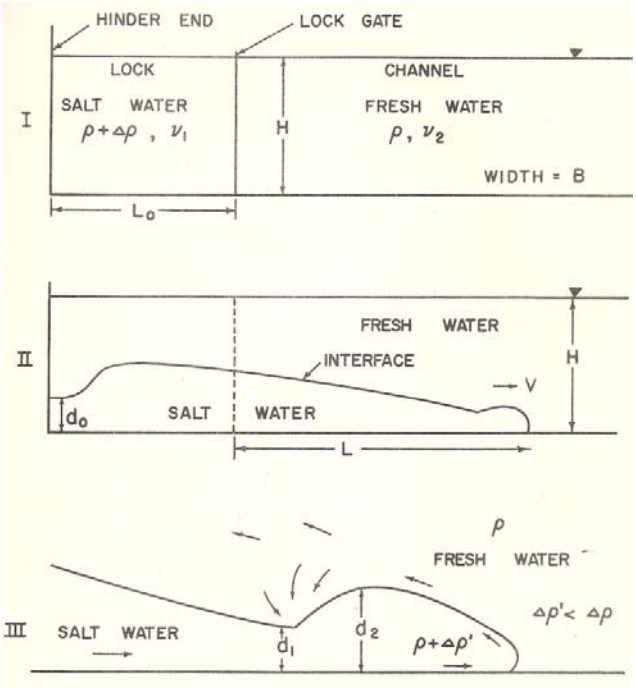

Figure 2.11 Notation diagram. (Ⅰ) Lock & Channel, (Ⅱ) Advancing front, (Ⅲ) Idealized shape of saline front (from Keulegan 1957).

Middleton (1996a) performed experiments on density currents formed by plastic beads and salt solution and presented the formula for predicting propagation speed given by

$$U_f = 0.75\sqrt{\frac{\Delta\rho}{\rho} g d_2} \tag{2.22}$$

He developed the velocity formula (i.e., equation for the head of the density currents analogous to the Equation (2.21) proposed by Keulegan (1957) for saline surges. He also found that Keulegan's formula was valid only for the bottom slopes up to 4%. Middleton (1996a) showed that the ratio U_f / U_d was close to unity at very mild slopes but became smaller than unity at the slopes steeper than 1%. He explained that the loss of salt water by strong mixing into the ambient water resulted in the decrease in the velocity of the head and the continuous transfer of salt water (i.e., denser water) from the body of the density current was required to keep constant velocity of the head. Thus, the body velocity can be slightly greater than the head.

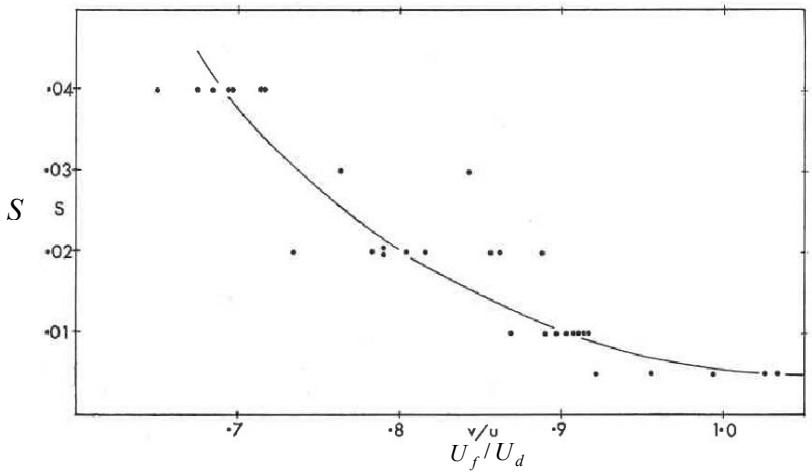

Figure 2.12 The ratio U_f/U_d, where U_f is the velocity of the head and U_d is the velocity of uniform flow established behind the head on the same slope, related to the slope, *S* (from Middleton 1996a).

Britter and Linden (2006) carried out laboratory experiments with a wide range of slope angles. They found the front velocity of a density flow, non-dimensionalized by the buoyancy flux, was independent of the slope. The experiments showed the relationship below:

$$\frac{U_f}{(g_o^{'}q)} = 1.5 \pm 0.2 \quad \text{for } 5^o \le \theta \le 90^o \tag{2.23}$$

where $q =$ unit discharge; $\theta =$ the angle of a bottom slope; and $g_o^{'} = g[2(\rho_2 - \rho_1)/(\rho_1 - \rho_2)]$ in which $\rho_1 =$ fresh water density and $\rho_2 =$ the density of a gravity current.

The early theory for turbidity current flow was developed in terms of steady and uniform flow, due to the theoretical simplicity of the assumptions. Many studies have dealt with the average velocity of uniform flow of a density current using a Chézy type equation (Komar 1973; Kuenen 1952; Kullenberg 1954; Middleton 1996b).

$$U_d = \acute{C}\sqrt{g' h_d} \tag{2.24}$$

$$\acute{C} = \sqrt{\frac{8g'}{f}} \tag{2.25}$$

where U_d =the mean velocity of an uniform density current (underflow); $\acute{C}$ =a modified Chézy coefficient;and $g' = \Delta\rho / \rho$; R =the hydraulic radius for a rectangular channel $\left[R = W h_d / (W + 2h_d)\right]$ in which W = channel width; h_d =the depth of a density current; and $f = f_o + f_i$ where f_o and f_i are the resistance of geometry boundaries and fluid interfaces, respectively. For large-scale turbidity currents in a reservoir, the resistance of geometry boundary (f_o) may be estimated using a hydraulically rough boundary similar to an open channel. In the case of the fluid interfacial resistance (f_i), it is much more difficult to predict. Lofquist (1960), Middleton (1966b), and Dermissis and Partheniades (1984) found that the (f_i) depended on both the Froude and Reynolds numbers. In addition to the proportional relationship between (f_i) and Froude number, Lofquist (1960) concluded that f_i should be proportional to $Re^{-3/5}$ through a number of experimental data using salinity.

Polk *et al.* (1971) investigated field data in rivers with thermal wedges formed by discharge of power plants and they used an analytical model to determine resistance factors. They concluded the value of f_i and f_o ranged from 0.008 ~ 0.013 and 0.026 ~ 0.036, respectively. Harleman and Stolzenbach (1972) studied for density flows developed by the heated water disposal from a power generation. They plotted data on interfacial friction factors against the Reynolds number of the density currents Re_d (see Figure 2.13).

$$f_i = \sqrt{\frac{96}{Re_d}} \qquad (\text{if } Re_d < 10^3) \tag{2.26}$$

$$\frac{1}{\sqrt{f_i}} = 2.01 \log\left(Re_d \sqrt{f_i}\right) - 0.8 \qquad (\text{if } Re_d > 10^3) \tag{2.27}$$

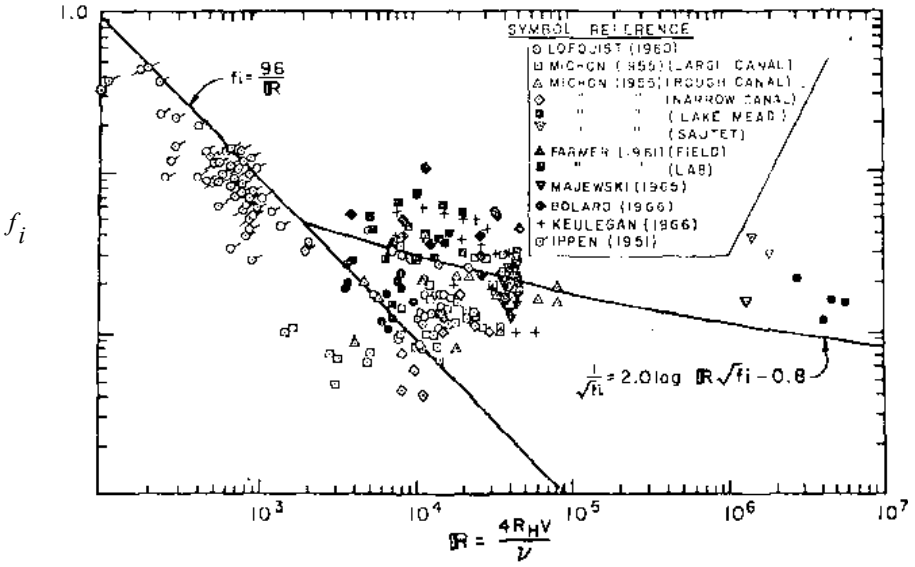

Figure 2.13 Interfacial friction (f_i) **versus densimetric Reynolds number** $Re_d = U_d h_d / \nu$ **(from Harleman and Stolzenbach 1972).**

Lofquist (1960) and Middleton (1966b) found that the (f_i) decreases with increasing Re_d and decreasing Fr_d. However, Dermissis and Partheniades (1984) could not find any unique correlation between an interfacial friction and either Re_d or Fr_d. They concluded that an average (f_i) could be best correlated with the number of $Re_d\ Fr_d^2$ and with the relative density difference (i.e., $\Delta\rho / \rho$) used as an independent parameter.

Keulegan (1949) defined an interfacial stability number (ϑ)

$$\vartheta = \left(\frac{\nu g \Delta\rho}{U_d^3 \rho} \right)^{1/3} = \left(\frac{1}{Fr_d^2 Re_d} \right)^{1/3} \tag{2.28}$$

where $Fr_d = U_d / \sqrt{(\Delta\rho / \rho) g h_d}$ and $Re_d = U_d h_d / \nu$. The occurrence of mixing across the interface depends on the critical Keulegan number (ϑ_c). The average experimental value of ϑ_c for laminar flow was estimated to be $\vartheta_c = 1/Re_d^{1/3}$ and $\vartheta_c = 0.18$ for turbulent flow. The flow will be stable (i.e., mixing is small), if $\vartheta > \vartheta_c$. On the contrary, when $\vartheta < \vartheta_c$, the interfacial mixing happens.

More practical approaches to determine the mean velocity of the turbidity current in a reservoir were found in Julien (1998), Komar (1973), and Middleton (1993).

$$U_d = \sqrt{\frac{8g'h_d S_o}{f_d(1+\alpha_d)}} \tag{2.29}$$

where $S_o =$ the bottom slope. For the case of laminar flow (i.e., $Re_d < 10^3$),

$$f_d(1+\alpha_d) = 1.64 f_d = \frac{58}{Re_d} \tag{2.30}$$

In the case of turbulent flow (i.e., $Re_d > 10^3$), $f_d \approx 0.01$ and $\alpha_d \approx 0.5$. On the basis of field data, Morris and Fan (1998) presented that the total friction value (f) was typically estimated to be about 0.025 for Chinese reservoirs.

2.2.3 Interflow

Interflow (or intrusive gravity current) intruding into a stratified reservoir body occurs when the underflow reaches an elevation at which the densities of the underflow and ambient water are equal. It will leave the bottom and propagate horizontally at this elevation. When it intrudes into a reservoir, the turbulence induced by the boundary will quickly dissipate and only fluid interfacial resistance affects the mixing as an internal shear force. The propagation speed of interflow will be slow with decreasing inflow momentum and particles will settle or stay at that layer for a long time depending on the size of particles.

Many investigators carried out laboratory studies of the velocity structure in an intrusive gravity current (Benjamin 1968; De Rooij *et al.* 1999; Faust and Plate 1984; Holyer and Huppert 1980). Figure 2.14 shows a schematic diagram of an intrusive gravity current with head speed (U_f).

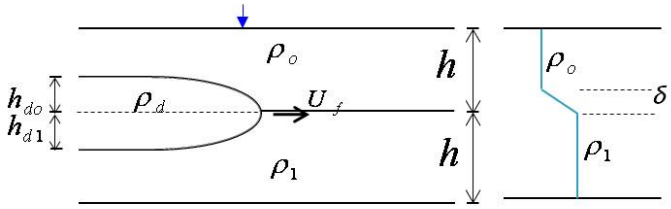

Figure 2.14 (Left) A sketch of an intrusion density flow. (Right) A typical vertical density profile, in which δ represents the height of the interface negligible thin.

Lowe *et al.* (2002) derived the theoretical head speed of the currents based on the analysis of Holyer and Huppert (1980), and De Rooij *et al.* (1999) assuming the flow to be energy-conserving and applied Bernoulli's equation along streamlines of the intrusion currents.

$$U_f^2 = 2g_o^{'}h_{do}\left(\frac{h^2}{(h-h_{do})^2}+\frac{g_o^{'}}{g}\right)^{-1} \tag{2.31}$$

$$U_f^2 = 2g_1^{'}h_{d1}\left(\frac{h^2}{(h-h_{d1})^2}+\frac{g_1^{'}}{g}\right)^{-1} \tag{2.32}$$

where the reduced gravities are defined by $g_o^{'} = g(\rho_d - \rho_0)/\rho_0$ and $g_1^{'} = g(\rho_1 - \rho_d)/\rho_1$. Because in this situation $\rho_d = 0.5(\rho_o + \rho_1)$, the $g_o^{'}$ can be simplified to $g_o^{'} = \frac{1}{2}g\left[(\rho_o/\rho_1)^{-1} - 1\right]$ and $g_1^{'} = \frac{1}{2}g\left[1-(\rho_o/\rho_1)\right]$. When the density differences between the two fluids are small (i.e., Boussinesq fluids), the values of $g_o^{'}/g$ and $g_1^{'}/g$ were assumed to be zero. Thus, the Equations (2.31) and (2.32) can be approximated as

$$U_f = \sqrt{2g_o^{'}h_{do}}\left(1-\frac{h_{do}}{h}\right) \tag{2.33}$$

$$U_f = \sqrt{2g_o^{'}h_{d1}}\left(1-\frac{h_{d1}}{h}\right) \tag{2.34}$$

They also expected that an intrusion depth in each layer will be close to half-depth in each of the ambient layers, thus

$$h_{do} = h_{d1} = \frac{h}{2} \tag{2.35}$$

Therefore, the front speed of the intrusive gravity current is defined by

$$\frac{U_f}{\sqrt{g_o' h}} = \frac{1}{2} \tag{2.36}$$

They performed experiments in a rectangular Plexiglas tank shown in Figure 2.15. They confirmed the front speed corresponded to the energy-conserving front speed proposed in Equations (2.33) and (2.34).

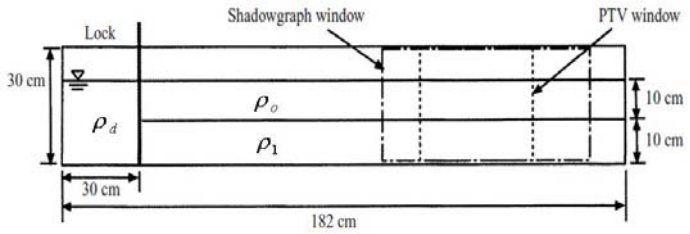

Figure 2.15 The experimental setup for intrusive gravity currents into a two-layer fluid (from Lowe *et al.* 2002).

Kao (1977) derived the front propagating speed along a sharp interface between two homogeneous fluids on the basis of the Bernoulli theorem, as shown in Figure 2.16. He found the front speed,

$$U_f = \sqrt{2 \frac{\rho_1 - \rho_d}{\rho_d} \frac{\rho_d - \rho_o}{\rho_1 - \rho_o} g\, h_d} \tag{2.37}$$

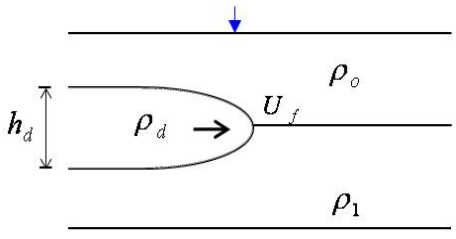

Figure 2.16 Internally spreading currents between a stably stratified interface (from Kao 1977).

For defining more complicated flow types in a two-layer fluid, three dimensionless parameters (σ, ε, Δ) were introduced in Sutherland *et al.* (2004). The dimensionless parameter σ is defined as the relative density difference between the gravity current and ambient fluid layers, given by

$$\varepsilon = \frac{\rho_d - \overline{\rho}}{\rho_1 - \rho_o} \tag{2.38}$$

Here, the depth-weighted average density $\overline{\rho} = (\rho_o h_o + \rho_1 h_1)/H$, and ρ_d is the density of fluid in the lock. Therefore, the experiments with $\varepsilon = 0$ correspond to cases in which the density of the lock fluid is equal to the depth-weighted average density of the upper and lower layers ($\overline{\rho} = \rho_d$). Another parameter σ is used to characterize the relative density difference between the upper and lower layers, defined as

$$\sigma = (\rho_1 - \rho_o)/\rho_o \tag{2.39}$$

The relative depth of the upper and lower layer ambient fluids compared with total depth is characterized with the parameter Δ given by

$$\Delta = \frac{(h_o - h_1)}{H} \tag{2.40}$$

For example, experiments with $\Delta = 0$ correspond to cases in which the upper and lower layers have equal depth. Holyer and Huppert (1980) extended the theory derived by Benjamin (1968) to describe the dynamics of interfacial gravity currents. Sutherland *et al.* (2004) adapted the theory of Holyer and Huppert (1980) to develop an empirical prediction for propagation speed, given by

$$U_d = 0.25\,\overline{H}\left[1 + \frac{2\Delta}{\overline{H}^2}\varepsilon + \frac{1-2\Delta^2}{\overline{H}^4}\varepsilon^2\right]\sqrt{g\sigma H} \tag{2.41}$$

where $\overline{H} = (1-\Delta^2)^{1/2}$. They defined the symmetry degree of intrusion into a two-layer fluid using ε and Δ. When the fluid density contained behind the lock gate is equal to the depth-weighted

average densities of ambient two layer fluid, the intrusive gravity current is regarded as a symmetrical flow, $\varepsilon = 0$. More perfect symmetrical intrusive gravity currents occur when $\varepsilon = 0$ and $\Delta = 0$, while asymmetrical cases happen with $\varepsilon \neq 0$. For the perfect symmetrical intrusive gravity currents ($\varepsilon = 0$ and $\Delta = 0$), the Equation (2.41) can be simplified to $U_d = 0.25 / \sqrt{g\sigma H}$. This is identical to the analytical solution of Lowe *et al.* (2002).

The change from underflow to interflow may cause initial mixing and entrainment so that the densities of the underflow and interflow may not be same. Wells and Nadarajah (2008) found the entrainment ratio (E) also affects the location of intrusion. They presented theory and carried out laboratory experiments to describe the depth where a density current intrudes into a linear stratified water layer. They found the relationship between intrusion depth and the entrainment ratio E, the buoyancy flux in the density current, the value of N, given by

$$Z = E^{-1/3} B^{1/3} / N \tag{2.42}$$

where Z= the depth of the intrusion scale; E= entrainment coefficient (E= 3±1, from laboratory experiments); B= buoyancy flux(= $g_i' Q$); and N =buoyancy frequency.

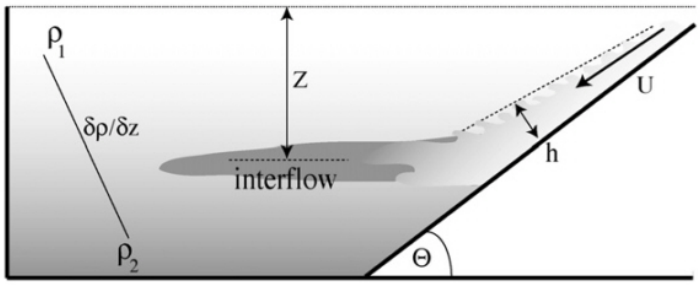

Figure 2.17 A sketch of a subsurface intrusion from a density current. The initial density current has a velocity U and depth h and flows down a slope of angle before intruding into the stratified waters at a depth Z below the surface (from Wells and Nadarajah 2008).

Imberger *et al.* (1976) proposed a dimensionless parameter (R) to predict interflow dynamics. They assumed the interflow has neutral buoyancy and symmetrical conditions between the inflow

and outflow. They also assumed the inflow momentum is small. They defined the dimensionless parameter (R), which is shown as

$$R = F_i Gr^{1/3} \tag{2.43}$$

where F_i = internal Froude number ($F_i = q_i / N_i L^2$); L = a reservoir length; Gr = Grashof number ($Gr = N_i^2 L^4 / \kappa_v^2$); q_i = unit discharge at intrusion takeoff point (after intrusion); and κ_v = average vertical eddy viscosity in which N = the buoyancy frequency averaged over intrusion depth, defined as

$$N = \left(-\frac{g\,\partial\rho}{\rho_i \partial z} \right)^{1/2} = \left(\frac{g_i'}{h_i} \right)^{1/2} \tag{2.44}$$

where ρ_i = density at centerline of intrusion; and $\partial\rho$ = change in density over h_i The Prandtl number is defined as

$$Pr = \kappa_v / \kappa_T \tag{2.45}$$

where κ_T = average vertical diffusivity of heat. Using the dimensionless parameter (R) and the Prandtl number (Pr), the flow regimes are defined as

1. In case of R> 1, it is controlled by a balance between inertial and buoyancy forces.

   The intrusion length (L_i) is

   $$L_i = 0.44(q_i N)^{1/2} t \tag{2.46}$$

   The intrusion speed (U_i) is

   $$U_i = 0.44(q_i N)^{1/2} = 0.19(g_i' h_i)^{1/2} \tag{2.47}$$

   The intrusion depth (h_i) is

$$h_i = 2.99\left(\frac{q_i^2}{g_i'}\right)^{1/3} \tag{2.48}$$

2. In case of $Pr^{-5/6} < R < 1$, it is dominated by both viscosity and buoyancy.

$$L_i = 0.57LR^{2/3}t^{5/6} \tag{2.49}$$

$$U_i = 0.57LR^{2/3}t^{-1/6} \tag{2.50}$$

$$h_i = 5.5L_iGr^{-1/6} \tag{2.51}$$

3. In case of $R < Pr^{-5/6}$, it is dominated by both viscosity and diffusion and h_i is of the order $LGr^{-1/6}R^{1/5}$. The coefficient C, however, is not defined.

$$L_i = CLR^{3/4}Gr^{-1/8} \tag{2.52}$$

2.3 Numerical Simulations

Numerical simulation provides insight into time and spatially varying physical process in a reservoir. In the case of hydrodynamic modeling for a large water body (e.g., lake or reservoir), numerical simulation can be more attractive than laboratory experiments due to the complicated geometry and unsteady hydrological and hydraulic data. Early numerical simulations began with 1-D models, which are the simplest models averaged by horizontal direction (Figure 2.18). Many researchers applied the 1-D models to vertical stratified reservoirs (Balistrieri *et al*. 2006; Bell *et al*. 2006; Fang, 2004; Gosink, 1987). Such 1-D models are easy to set up with fewer boundary condition data, but require more parameterization. The 1-D models are not capable of simulating the entire process varying from plunging flow to interflow or overflow. Thus, large research has been focused on the development of multi-dimensional numerical models.

CE-QUAL-W2, two-dimensional (2-D) laterally averaged hydrodynamic water quality model, was developed by the U.S. Army Corps of Engineers and was successfully applied to water

quality modeling in many reservoirs (Cole and Wells 2006; Chung and Gu 1998; Williams 2007). Ahlfeld *et al.* (2003) observed interflow in the Wachusett Reservoir and presented the relation between interflow travel time and reservoir stratification through numerical simulations using CE-QUAL-W2. Yoon *et al.* (2008) simulated turbidity flow in Daecheong Reservoir and compared it with real-time monitoring data. They suggested the parameterization of particle settling velocity could induce significant error, because one constant value for settling velocity could not represent the settling velocity for all particles.

CE-QUAL-W2 is useful to analysis longitudinal and vertical movements of density currents during a long period with less runtime, because the model employs lateral homogeneity and hydrostatic pressure assumptions. These assumptions, however, may lead to inaccurate simulations in applying the model to the field, in which significant vertical movement occurs (Gu *et al.*1996). The 2-D model also shows a typical limitation on calculating travel time of density flow and reproducing the dynamic changes of the turbidity profiles at certain sites (Cantero *et al.* 2003; Patterson *et al.* 2005).

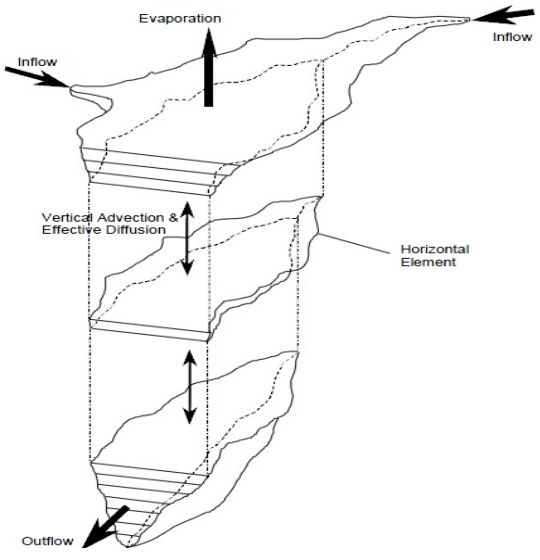

Figure 2.18 Discretization of a reservoir into horizontal layers for laterally averaged simulations (from Fleenor 2001).

The development and application of several three-dimensional (3-D) hydrodynamic models: ELCOM (Hodges and Dallimore 2007), UnTRIM (Cheng and Casulli 2001), and EFDC (Hamrick 1992; Tetra Tech Inc. 2007; Çalışkan and Elçi 2008) have been documented in the literature. Çalışkan and Elçi (2008) applied a 3-D model (EFDC) to investigate the effects of selective withdrawal. They found the discrepancies between measured and simulated results and concluded that these were attributable to a hydrostatic assumption. The governing equations of 3-D models include Reynolds Averaged Navier Stokes (RANS) equations, mass conservation equations, free-surface equations, equation of state relating density to temperature and sediments, and a conservation equation for each scalar variable. To simplify the governing equations, the models use the Boussinesq and hydrostatic assumptions and the water is assumed to be incompressible. The hydrostatic assumption neglects vertical acceleration and non-hydrostatic pressure gradients, so that it is generally employed for a reservoir in which horizontal length scales are larger than vertical scales (Hodges 2009). The 3-D model had been successfully applied to water quality simulations, providing physical understanding on a full seasonal limnological process in a reservoir.

Although the models were successfully used to reproduce reservoir hydrodynamics, seasonal temperature distribution, mixing, and intrusion of density currents, those 3-D models still have limitations to be an effective tool to regulate high turbidity currents in a reservoir. The effectiveness of engineering methods for regulating high turbidity problems in a reservoir cannot be assessed with 3-D models using the hydrostatic assumption. Because the engineering methods such as selective discharge, flushing, blocking curtains, or de-stratification probably induce a significant vertical acceleration, the three-dimensional (3-D) models using a hydrostatic assumption cannot provide accurate simulation for the complex movement (Antar and Moodie 2003; Lai *et al.* 2003; Çalışkan and Elçi 2008). Laval *et al.* (2003), and Wadzuk and Hodges (2004) suggested that non-hydrostatic pressure plays a crucial role in controlling internal wave evolution, which can influences mixing in a density stratified water body. Chen (2005) compared hydrostatic and non-hydrostatic pressure components in shallow waters and found that the non-hydrostatic

pressure gradient affects the velocity field and is not negligible even in case of shallow waters. Weilbeer and Jankowski (2000) conducted a series of numerical experiments to investigate hydrodynamical processes in the vicinity of structures using a 3-D non-hydrostatic model. Fringer *et al.* (2006) presented the numerical results of lock-exchange gravity currents using SUNTANS model and discussed the difference between hydrostatic and non-hydrostatic results. Figure 2.19 indicates that the hydrostatic simulation cannot capture the formation of the Kelvin-Helmholtz billows and does not reproduce propagation speed correctly. In contrast, the non-hydrostatic simulation captured both the propagation speed and the Kelvin-Helmholtz billows correctly. Their test shows that the hydrodynamical models simplified with the hydrostatic assumption cannot be applied to flow phenomena having large vertical velocities and accelerations.

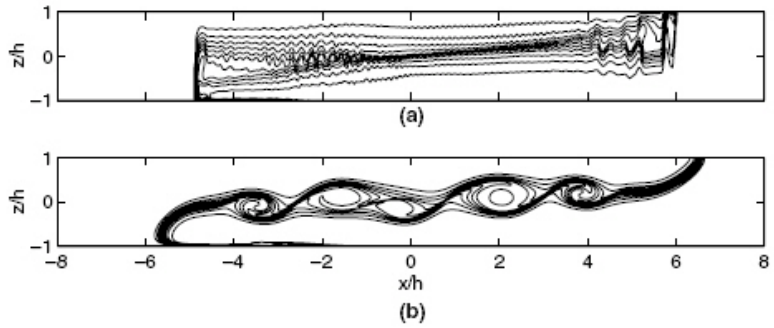

Figure 2.19 Comparison of the density contours from the (a) hydrostatic simulation and (b) non-hydrostatic simulation of the lock-exchange test, which were captured at same time. (from Fringer *et al.*, 2006).

Chapter 3

Numerical Model Description

3.1 Introduction

Computational Fluid Dynamics (CFD) has been widely applied in the various engineering branches of fluid mechanics due to its high accuracy. However, the application of the CFD model to the research for turbid density currents in a reservoir is a relatively new approach because the hydrodynamics of turbid density currents propagating into a stratified reservoir are very complex and numerically expensive to simulate.

In this study, three-dimensional computational fluid dynamic simulations were obtained with a CFD code (FLOW-3D). Some subroutines were incorporated into the FLOW-3D to reflect the change in density by suspended sediments and water temperature. FLOW-3D, developed by Flow Science, Inc., Santa Fe, USA, is a commercial code capable of fluid-boundary tracking and resolves fluid-fluid and fluid-air interfaces using its grid systems (a fixed, Eulerian approach, and structured, well ordered by a rectangular cell mesh). The model provides the transient, 3-D numerical solutions to multi-scale, multi-physics flow problems, especially showing the capabilities for accurately simulating free-surface flows with the improved Volume of Fluid (VOF) technique (Hirt and Nichols 1981). In addition of the VOF technique, the structured FAVOR (Fractional Area-Volume Obstacle Representation method) is used to get better geometric

representations of complex geometries in the grid system, based on rectangular cell meshes (Hirt 1993).

The FAVOR method is also employed to eliminate the flow loss, which may be caused by the Cartesian grid systems. The Cartesian grid representations of a curved flow regime generally can result in considerable numerical flow losses due to a zigzag approximation for the interface between flows and obstacles. The FAVOR method can eliminate the zigzag direction changes by smoothly blocking out fractional portions of grid cell faces and volumes.

The model numerically solves governing equations using the finite-difference (or finite-volume) approximations. In the FAVOR technique, each cell has all variables at its center except velocity, which is recorded at the cell-faces. Most terms in the governing equations are evaluated explicitly (i.e., using the current time-level values of the local variables). It presents a very simple and efficient numerical algorithm, while needing the use of a restricted time-step (i.e., a shorter time-step size than that of an implicit approach) to maintain numerical stability. However, the model employs the implicit approach in the treatment of pressure forces, where the pressures are coupled with velocities implicitly by using time-advanced pressures in the momentum equations and time-advanced velocities in the continuity equation.

This semi-implicit formulation of the finite-difference formulas provides efficient solutions, but the semi-implicit formulation, which consists of coupled sets of equations, needs the application of an iterative technique to gain its solutions. The model provides two numerical methods. A successive over-relaxation (SOR) method is the simplest method and a special alternating-direction, line-implicit method (SADI), a more implicit method, is also available in the model.

3.2 Governing Equations

The model simultaneously solves the governing equations for three-dimensional motion of fluids, the conservation of mass, and the transport of scalar variables.

Momentum equation:

Using the Boussinesq approximation for small density differences, the governing equations of momentum are written as follows:

$$\frac{\partial u_i}{\partial t} + u_j \frac{\partial u_i}{\partial x_j} = -\frac{1}{\rho_r}\frac{\partial p}{\partial x_i} + \frac{\partial}{\partial x_j}\left(\nu \frac{\partial u_i}{\partial x_j} - \overline{u_i' u_j'} \right) + g_i \frac{\rho - \rho_r}{\rho_r} \tag{3.1}$$

where u_i = mean velocity components (i.e., u, v, w in a Cartesian coordinate system); x_j = Cartesian space (x, y, z); $\overline{u_i' u_j'}$ = Reynolds stress; ρ_r = reference density; g_i = gravitational acceleration components in each direction; ν = kinematic viscosity; and ρ = density of gravity currents, which should be determined as a function of temperature and sediment concentration. The density change by water temperature and concentration of sediments can be calculated using Equation (2.1) and Equation (2.2).

Continuity equation:

$$\frac{\partial u_i}{\partial x_i} = 0 \tag{3.2}$$

Scalar transport equation:

$$\frac{\partial \phi}{\partial t} + \frac{\partial}{\partial x_i}(u_i \phi) = \frac{\partial}{\partial x_i}\left(\Gamma \frac{\partial \phi}{\partial x_i} - \overline{u_i' \phi'} \right) \tag{3.3}$$

where Γ = diffusivity for property ϕ; ϕ = mean scalar; ϕ' = the corresponding fluctuating scalar; and $\bar{}$ (Overbar) = averaging of fluctuating quantities. Equation (3.3) is a scalar equation which can solve scalar transport (e.g., sediments or temperature etc.) and is coupled with the Navier-Stokes equations only in the buoyancy term due to Boussinesq approximation.

Fluid interfaces and free-surface equation:

Fluid configuration is defined in terms of VOF function, $F(x, y, z, t)$. The VOF function represents the volume of fluid per unit volume and satisfies the equation given by

$$\frac{\partial F}{\partial t}+\frac{1}{V_F}\left[\frac{\partial (F A_i u_i)}{\partial x_i}\right]=0 \tag{3.4}$$

where V_F = the fractional volume open to flow; A_i = the fractional area open to flow in i th direction; and F = VOF function (Hirt and Sicilian 1985).

3.3 Turbulence Modeling

Most flows of engineering interest are turbulent and focused on the mean quantities for engineering applications. The Reynolds averaging aims to separate each flow variable into mean and turbulent components. When we apply the process of the Reynolds averaging to momentum equations, we can confirm that $\overline{u_i' u_j'}$ appears additionally in the momentum equations. The $\overline{u_i' u_j'}$ represents momentum fluxes by the turbulence. It is well known that the velocity fluctuations connected with turbulence cause additional stresses on the fluid (so-called Reynolds stresses) and those can be written as:

$$\tau_{ij}=-\overline{u_i' u_j'}=\nu_t\left(\frac{\partial u_i}{\partial x_j}+\frac{\partial u_j}{\partial x_i}\right)-\frac{2}{3}\rho k \delta_{ij} \tag{3.5}$$

where ν_t = the turbulent viscosity; δ_{ij} = the Kronecker delta; and k = turbulent kinetic energy. The $\overline{u_i' \phi'}$ represents the turbulent scalar flux by turbulent motion and can be modeled similarly:

$$-\overline{u_i' \phi'}=\Gamma_t \frac{\partial \phi}{\partial x_i} \tag{3.6}$$

where Γ_t = turbulent or eddy diffusivity. Since eddy mixing contributes to both the turbulent transport of momentum and a scalar, the value of diffusivity (Γ_t) is generally assumed to be close to that of eddy viscosity (ν_t) in homogeneous flow. The ratio of ν_t to Γ_t is called the turbulent

Prandtl (Pr_t) or turbulent Schmidt number (Sc_t), defined with

$$Pr_t \text{ or } Sc_t = \frac{\nu_t}{\Gamma_t} \tag{3.7}$$

The CFD models using RANS (Reynolds-Averaged Navier-Stokes equations) models need to use the Pr_t or Sc_t to model scalar transport. The value of Pr_t or Sc_t was generally determined by laboratory experiments.

In order to close the system of mean flow Equations (3.1) and (3.3), a turbulence model is required. The most common turbulence model in engineering flow analysis is a two-equation eddy viscosity model (e.g., $k-\varepsilon$ model). In the $k-\varepsilon$ model, the eddy viscosity is given by

$$\nu_t = c_\mu k^2 / \varepsilon \tag{3.8}$$

In the Equation (3.8), the turbulence kinetic energy k is obtained from the following transport equation:

$$\frac{\partial k}{\partial t} + u_i \frac{\partial k}{\partial x_i} = \frac{\partial}{\partial x_i}\left(\frac{\nu_t}{\sigma_k}\frac{\partial k}{\partial x_i}\right) + P + G - \varepsilon \tag{3.9}$$

The equation for the rate of dissipation of turbulent kinetic energy ε is defined as

$$\frac{\partial \varepsilon}{\partial t} + u_i \frac{\partial \varepsilon}{\partial x_i} = \frac{\partial}{\partial x_i}\left(\frac{\nu_t}{\sigma_\varepsilon}\frac{\partial \varepsilon}{\partial x_i}\right) + c_{1\varepsilon}\frac{\varepsilon}{k}(P + c_{3\varepsilon}G) - c_{2\varepsilon}\frac{\varepsilon^2}{k} \tag{3.10}$$

where P and G are given by

$$P = \nu_t\left(\frac{\partial u_i}{\partial x_j} + \frac{\partial u_j}{\partial x_i}\right)\frac{\partial u_i}{\partial x_j} \tag{3.11}$$

$$G = g_i \frac{\nu_t}{Sc_t}\frac{1}{\rho_r}\frac{\partial \rho}{\partial x_i} \tag{3.12}$$

where $c_\mu = 0.09;\ c_{1\varepsilon} = 1.42;\ c_{2\varepsilon} = 1.83;\ c_{3\varepsilon} = 0.2;\ \sigma_k = 1.39;$ and $\sigma_\varepsilon = 1.39$ (FLOW-3D 2007).

In this study, we employ Renormalization Group (RNG) $k-\varepsilon$ turbulence model for the RANS approach. This turbulence model generally provides improved predictions of turbulence flows relative to the traditional $k-\varepsilon$ model. It includes the additional term (R_ε) in the right hand side of the Equation (3.10), given by

$$-R_\varepsilon = \frac{c_\mu \eta^3 (1-\eta/\eta_o)}{1+\beta\eta^3}\frac{\varepsilon^2}{k} \tag{3.13}$$

where β = a constant. The turbulent time-scale η is proportional to the mean flow time-scale. It is defined as

$$\eta = S\frac{k}{\varepsilon} \tag{3.14}$$

where $S=\sqrt{2S_{ij}S_{ij}}$, and $S_{ij}=\frac{1}{2}(u_{ij}+u_{ji})$. In parameters of the RNG $k-\varepsilon$ turbulence model, we used the following values of turbulence coefficients presented by Yakhot and Orszag (1986) ($\eta_0 = 4.38,\ \beta = 0.015$).

The FLOW-3D code is also capable of simulating turbulence using the LES model. In the LES model, large eddies are resolved directly, but small eddies are modeled using a subgrid-scale turbulence model. For the large eddies, the governing equations are obtained by filtering them in either Fourier space (wave-number) or physical space. The subgrid-scale turbulence model adopted in the model is based on the Boussinesq hypothesis, as in the RANS approach. In this case, the Reynolds stresses are defined as following:

$$\tau_{ij} = -2\nu_t e_{ij} - \frac{2}{3}\rho k \delta_{ij} \tag{3.15}$$

$$e_{ij} = \frac{1}{2}\left(\frac{\partial u_i}{\partial x_j}+\frac{\partial u_j}{\partial x_i}\right) \tag{3.16}$$

where μ_t denotes the subgrid-scale turbulent viscosity and e_{ij} represents the strain rate tensor components. In Smagorinsky large eddy simulation, μ_t is defined with

$$\nu_t = (c\,L)^2 \sqrt{e_{ij} e_{ij}} \tag{3.17}$$

where c is a constant equal to 0.2 and L is a length scale. Smagorinsky (1963) quantified L a geometric mean of the grid cell dimensions,

$$L = (\delta x \delta y \delta z)^{1/3} \tag{3.18}$$

This method generally needs considerably finer meshes than those for RANS simulations, leading to high computational costs in terms of memory and run time (i.e., CPU time). For application of the LES to a field-scaled domain, a high-performance computing scheme (e.g., a parallel computing algorithm) is required.

3.4 Numerical Approximation

The model numerically solves the governing equations using finite difference (or finite-volume) approximations. A mesh of fixed rectangular cells subdivides the flow region and has local average values of all dependent variables, located at the centers of the cells and their faces. For numerical discretization of the governing equations, control volumes are defined surrounding each dependent variable location, and then surface fluxes, surface stresses, and body forces are computed in terms of surrounding variable values (i.e., staggered finite-difference grid).

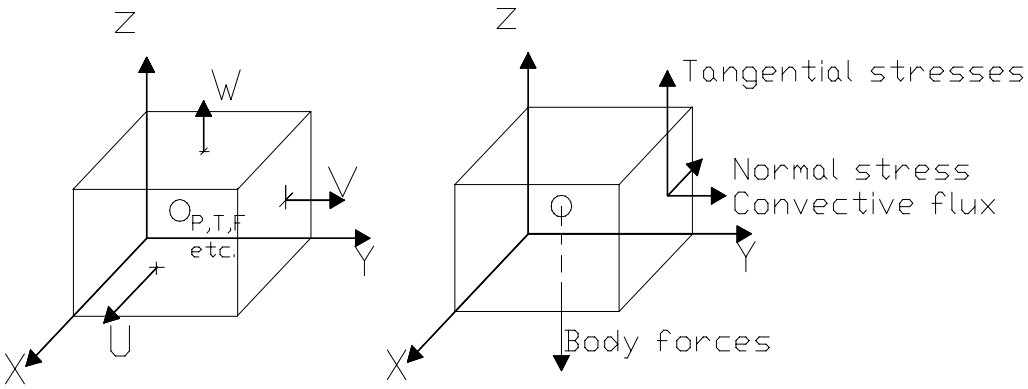

(a) Primary variable locations and conventions (b) Forces locations, control volume=mesh cell

Figure 3.1 Staggered finite-difference grid in the model.

The model explicitly evaluates most terms using the current time-level values of the local variables except pressure forces, where the pressures are coupled with velocities implicitly by using time-advanced pressures in the momentum equations and time-advanced velocities in the continuity equation. The basic procedure for advancing a solution through one time step (δt) is the following:

1. Solve coupled momentum and continuity equations using predictor and corrector steps to find new pressures and velocities. The predictor step estimates the initial velocity from the momentum equations using finite-difference approximations to the momentum equations defined by

$$U_{ijk}^{n+1} = U_{ijk}^{n} + \delta t^{n+1}\left(-\frac{P_{i+1jk}^{n+1} - P_{ijk}^{n+1}}{(\rho\delta x)_{i+\frac{1}{2}jk}^{n}} + G_x - FUX - FUY - FUZ + VISX - WSX \right)$$

$$V_{ijk}^{n+1} = V_{ijk}^{n} + \delta t^{n+1}\left(-\frac{P_{ij+1k}^{n+1} - P_{ijk}^{n+1}}{(\rho\delta y)_{ij+\frac{1}{2}k}^{n}} + G_y - FVX - FVY - FVZ + VISY - WSY \right)$$

$$W_{ijk}^{n+1} = W_{ijk}^{n} + \delta t^{n+1}\left(-\frac{P_{ijk+1}^{n+1} - P_{ijk}^{n+1}}{(\rho\delta z)_{ijk+\frac{1}{2}}^{n}} + G_z - FWX - FWY - FWZ + VISZ - WSZ \right) \quad (3.19)$$

where $(\rho\delta x)^{n}_{ii+\frac{1}{2}jk} = (\rho^{n}_{ijk}\delta x_i + \rho^{n}_{i+1jk}\delta x_{i+1})/2$, *FUX* indicates the advective flux of *U* in the x-direction, *VISX* is the x-component viscous acceleration, *WSX* means the viscous wall acceleration in the x-dirction, and *GX* is the gravitational acceleration. Time step size was computed automatically for better speed and accuracy. The advection terms can be solved using explicit or implicit differencing with the first, second, or third order accuracy. Most approximations are based on an explicit method with the first order accuracy for the simulations of a large field domain. Two options (i.e., explicit or implicit approximations) are also available to modeling viscous terms. The corrector step is to adjust pressure and velocities to satisfy the continuity equation. The pressures are iteratively adjusted in each cell and the velocity changes induced by each pressure change are added to the velocities that are computed in the predictor step. The model has two available options for the pressure iteration [i.e., SOR (Successive Over-relaxation) and ADI (Matrix Inversion for line of cells)].

2. In the case of a free-surface or fluid interface, it will be updated through solving the VOF equation to provide the new fluid configuration in the surface cell.
3. Turbulence quantities are updated in this step. Remaining variables are also updated using new velocities, pressures, and fluid fraction (e.g., density advection and diffusion, scalar advection and diffusion etc.).

In order to avoid numerical instabilities, the model suggests a time-step size to satisfy the following criteria. First, fluid should not be permitted to flow across more than one cell in one computational time step. The time-step size depends not only on the velocity, but also on a ratio of fractional volume to fractional area defined by the FAVOR method. This condition is defined with

$$\delta t < Con \cdot \min\left(\frac{V_f \delta x_i}{A_x \cdot U}, \frac{V_f \delta y_j}{A_y \cdot V}, \frac{V_f \delta z_k}{A_z \cdot W}\right) \tag{3.20}$$

where U,V,W are velocity magnitudes. $\delta x, \delta y,$ *and* δz are cell sizes in each direction. CON is a safety factor, typically 0.45. V_F and A are a fractional volume and area, open to flow in the FAVOR method (see Figure 3.2).

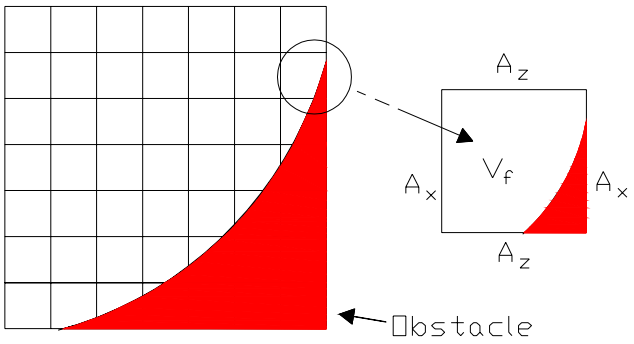

Figure 3.2 The FAVOR method representing blockages within the mesh. V_F is a ratio of open volume/volume of cell. A indicates a ratio of open area/cell edge area.

If there is considerable flow in the cell with a large open face area and a relatively small volume, the time-step could restrict the time-step size to very small values. Thus, if this happens, it may be necessary to modify the mesh constructed between the obstacle and open area. In FLOW-3D, if the automatic time-step is selected, the model adjusts the time step to be as large as possible while keeping the stability criteria.

3.5 Particle Dynamics Algorithm

General flow situations are approximated using incompressible fluids for engineering applications, but sometimes need evaluation of the influence of buoyant forces associated with small density variations on their dynamics. In the original FLOW-3D, the density variation is usually represented as a function of temperature only. The model provides a solution of the flows, influenced by buoyant forces, by coupling its incompressible flow solution algorithm with an energy transport equation and a local evaluation of the density as a function of temperature. When

the model uses the buoyant flow model, the fluid density in each computational cell is determined from the local fluid fraction (F) and temperature (T) as

$$\rho = F \cdot \rho_1(T) + (1-F)\rho_2(T) \tag{3.21}$$

where

$$\rho_1(T) = RHOF \times \left[1 - THEXF1 \times (T - T^*)\right]$$

$$\rho_2(T) = RHOFC \times \left[1 - THEXF2 \times (T - T^*)\right] \tag{3.22}$$

In Equation (3.22), RHOF and RHOFC are density of fluid #1 and fluid #2, respectively, at a reference temperature(T^*). THEXF is a thermal expansion coefficient. The fluid temperature is calculated from transport equations for the internal energy in two-fluid cases.

When we try to apply the buoyant flow model to the simulations of turbid density currents entering a stratified reservoir, the model shows some limitations to the application. Only the temperature determines the density difference in the buoyant flow model, while the density should be determined as a function of temperature and sediment concentration for the application. Another limitation is that the model only uses a two-fluid model option to simulate the density flows. However the initial vertical density distribution of a thermally stratified reservoir cannot be reproduced by only two different fluids, because the densities of each cell in a water column have their specific values, determined by their different temperatures and sediment concentrations. Furthermore, if the turbid inflows consist mainly of relatively large particle sizes, the settling rate of particles may significantly influence the variations of sediment concentrations.

Therefore, we developed the particle dynamics algorithm, which can be coupled with the FLOW-3D, so that it can reproduce the spatial-temporal changes in density at each cell via mixing, advection, and deposition of sediments. It can also reflect the change in density by the change of water temperature. The FLOW-3D provides some subroutines in FORTRAN source form that can be modified or coupled with a new algorithm. The advection of sediments is computed by

$$V_F \frac{\partial C_s}{\partial t} + \frac{\partial}{\partial x_i}(uAC_s) = \frac{\partial}{\partial x_i}\left[A\left(\Gamma \frac{\partial \phi}{\partial x_i} - \overline{u_i' \phi'} \right) \right] \tag{3.23}$$

where V_F = volume fraction of fluid in the computational cell; A = area fractions of each of the three directions open to fluid flow; u = local fluid velocity; and C_s = local concentration of sediments. Particle settling velocity (ω_s) within the numerical model is simply modeled by Stokes' Law according to the defined particle density (ρ_s) and diameter d_s, given by

$$\omega_s = \frac{g\, d_s^2}{18\,\nu}\left(\frac{\rho_s - \rho_w}{\rho_w} \right) = \frac{g\, d_s^2}{18\,\nu}\left(\frac{\rho_s}{\rho_w} - 1 \right) \tag{3.24}$$

It is incorporated into the Equation (3.23):

$$V_F \frac{\partial C_s}{\partial t} + \frac{\partial}{\partial x_i}(uAC_s) = \frac{\partial}{\partial x_i}\left[A\left(\Gamma \frac{\partial \phi}{\partial x_i} - \overline{u_i' \phi'} \right) \right] + \frac{\partial(\omega_s AC_s)}{\partial z} \tag{3.25}$$

In each computational cell, the mass change defined using the finite-volume notation corresponding to that used in the FLOW-3D code yields

$$M_{ijk}^{n+1} = VF_{ijk} C_{ijk}^n \delta x \delta y \delta z + AFT_{ijk} \omega_s C_{ijk+1}^n \delta x \delta y \delta t - AFT_{ijk-1} \omega_s C_{ijk}^n \delta x \delta y \delta t \tag{3.26}$$

where VF_{ijk} = volume fraction of fluid of cell (*i, j, k*); M_{ijk}^{n+1} = mass change at cell (*i, j, k*) at time level n+1; and AFT_{ijk} = fractional area for flow in z-direction at k + ½ cell-face (see Figure 3.3).

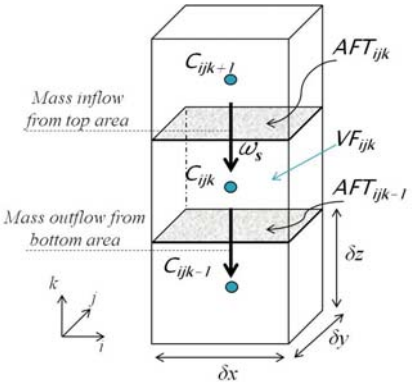

Figure 3.3 Schematic of the mass change due to sediment deposition at cell (*i, j, k*).

The densities ρ^n_{ijk} can be defined as a function of temperature and sediment concentration. Gill (1982) proposed the formulation for the density variation due to temperature change in Equation (2.1). When the water density increases due to adding sediments into water, total density can be defined as

$$\rho^n_{ijk} = \rho_w(T)^n_{ijk}\left[1+(G-1)\frac{V_{s}{}^n_{ijk}}{V_{ijk}}\right] \tag{3.27}$$

where $\rho_w(T)^n_{ijk}$ = water density at cell (*i, j, k*) at temperature T °C; $V_{s}{}^n_{ijk}$ = sediment volume at cell (*i, j, k*) and at time level; and V_{ijk} = total fluid volume at cell (*i, j, k*). The particle dynamics algorithm is capable of simulating up to 100 different particle size classes. Equation (3.27) is also employed to specify initial thermal stratification of a reservoir and inflow temperature and sediment concentration. Figure 3.4 depicts what factors change the density of each cell.

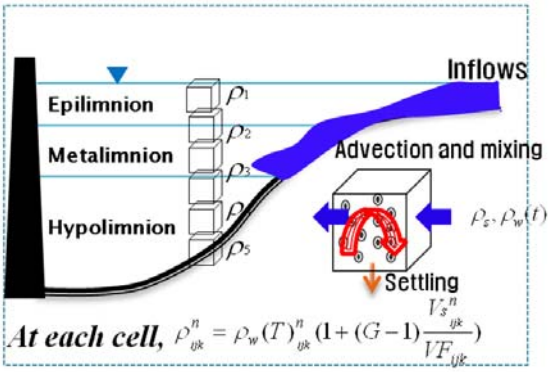

Figure 3.4 Schematic depicting the factors changing the density at each cell

Chapter 4[1]

Numerical Simulation of Lock-Exchange Gravity Currents

4.1 Introduction

Many studies have investigated various aspects of constant-volume gravity currents (also known as "gravity currents" or "buoyancy-driven currents) using lock-exchange experiments, where a constant volume of dense fluid is released into a less dense ambient fluid. The difference in density can be generally created by adjusting temperature or adding salt. In particular, some researchers have applied lock-exchange experiments to turbidity currents by adding suspended particles.

In this chapter, the RANS approach with a turbulence model is mainly employed to simulate the density currents, while some work on LES modeling is briefly presented due to its long computational runtime. In order to use experimental data for the validation and calibration of the numerical model, simulations were performed under the identical condition that corresponds to the laboratory experimental setup in some of published papers. A series of numerical simulations were performed to identify the effect of various parameters on the propagation speed of gravity currents. The numerical simulations were focused on two different types of Intrusive Gravity Currents (hereafter IGC): (1) IGC intruding into a two-layer fluid; and (2) IGC intruding into a continuously stratified fluid.

[1] This chapter has been submitted in substantial part as a paper entitled "Numerical Simulation of Particle-Driven Gravity Currents", by Sangdo An, P. Y. Julien, and S. K. Venayagamoorthy, to the *Environmental Fluid Mechanics*.

The simulation results of IGC intruding into a two-layer fluid were compared with the experimental measurements from Sutherland *et al.* (2004). This comparison was used to calibrate the model. The turbulent Schmidt number was calibrated against the experimental data (see Appendix A.2) and then the model was validated by the other laboratory experimental data from Britter and Simpson (1981) and Bolster *et al.* (2008).

The present work also contains numerical studies for the effect of particle settling on the propagation speed of gravity currents. Turbidity currents, which occur in many natural and man-made water bodies, are developed by an increased bulk density due to mass adding of suspended particles. Gladstone *et al.* (1998) carried out laboratory experiments on Particle-Driven Gravity Currents (hereafter PDGC) and offered the quantitative measurements of the propagation speed associated with the particle sizes. Their laboratory experiments were compared with the numerical simulations. The diagram below shows a configuration of lock-exchange simulations performed.

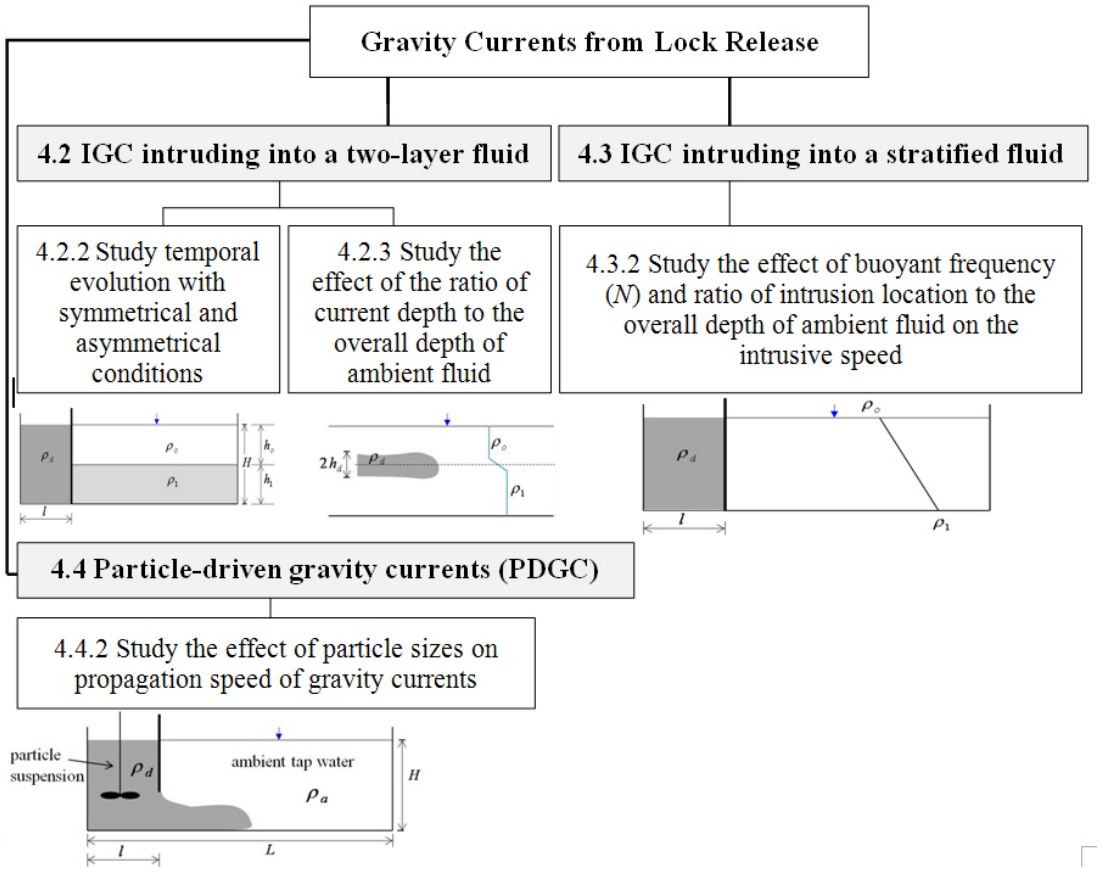

4.2 IGC Intruding into a Two-layer Fluid

4.2.1 Simulation setup

In order to simulate IGC into a two-layer fluid, we arranged dimensions and initial conditions, which correspond to the experimental setup in Sutherland *et al.* (2004) and Britter and Simpson (1981). The first simulation setup was arranged to be identical to the experimental dimensions in Sutherland's test: *L*=197.1 cm long by 17.6 cm wide by 48.5cm height, as shown in Figure 4.1. The lock-length (*l*) behind gate was fixed at 18.6 cm and the total water depth (*H*) was set equal to 20 cm. We considered three experimental cases. For defining different simulation cases, we used three dimensionless parameters (σ, ε , Δ). These parameters have been introduced in Sutherland *et al.* (2004). They defined the symmetry degree of intrusion into a two-layer fluid using ε and Δ. When the density contained behind the lock gate is equal to the depth-weighted average densities of ambient two layer fluid (ε = 0), IGC is regarded as a symmetrical flow. More perfect symmetrical IGC occurs when $\varepsilon = 0$ and $\Delta = 0$, while asymmetrical cases happen when $\varepsilon \neq 0$.

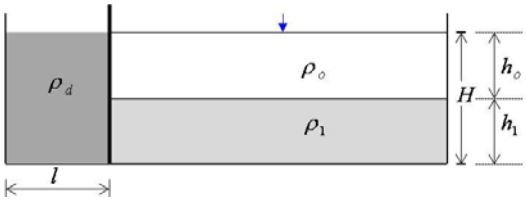

Figure 4.1 Setup and definition of parameters for experiments on intrusive gravity currents.

We conducted a total of three simulations with the experimental setup corresponding to the experiments of Sutherland *et al.* (2004). In the simulations (case 1 and case 2), the density of the lock fluid is equal to the depth-weighted average of the upper and lower layers (ε = 0). In case 1, the depth of the two layers in ambient fluids is equal ($h_o = h_1$) with σ = 0.02 . In the case 2, the depth of the two layers in ambient fluids is not equal ($h_o \neq h_1$) with σ = 0.02 . Case 3 was

conducted with $\varepsilon \neq 0$ (asymmetrical condition) and $\alpha = 0.02$. Table 4.1 shows the initial conditions for each simulation.

Table 4.1 Summary of the three symmetrical simulations.

Case	$\varepsilon = (\rho_d - \overline{\rho})/(\rho_1 - \rho_o)$	$\Delta = (h_o - h_1)/H$	H (cm)	h_0 (cm)	h_1 (cm)	$\overline{\rho}$ (kg/m^3)	ρ_1	ρ_0	ρ_d
1	0	0	20	10	10	1010	1020	1000	1010
2	0	0.75	20	17.5	2.5	1002.5	1020	1000	1002.5
3	0.625	0.75	20	17.5	2.5	1002.5	1020	1000	1015

At the solid boundaries, wall shear stresses were modeled by defining a zero tangential velocity on solid surfaces. At the free surface, no flux conditions were imposed. For tracking the free surface, we used the fluid interfaces tracking method (i.e., unsplit and split Lagrangian methods). The computational regions and mesh cells are illustrated in Figure 4.2 with the selected boundary conditions. The computational grid size in the X, Z directions was chosen to be 1 mm for 2-D simulations. For 3-D simulations, the computational grids were extended in the X, Y, and Z directions. However, the grid size became coarser ($dx, dz = 1$ mm, $dy = 30$ mm) due to the memory limitation on a 32-bit operating system. Two mesh blocks were created. The first mesh block is a domain that covers the fluid area filled behind the lock gate. The second mesh block is a larger domain that contains a two-layer fluid.

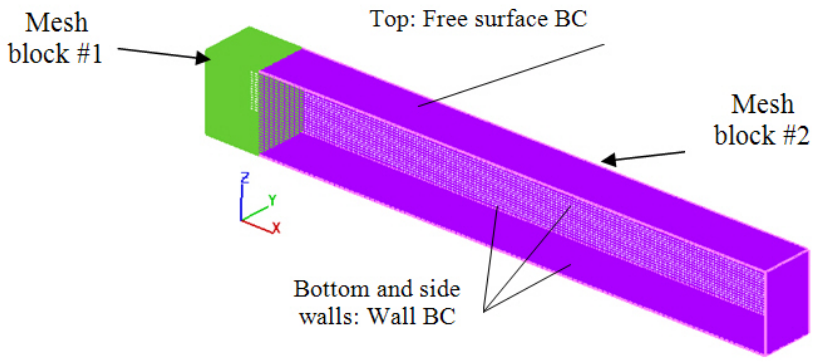

Figure 4.2 Computational domains, mesh cell boundary conditions for simulations corresponding to the experimental setup of Sutherland *et al.* (2004).

For initial conditions in the numerical simulations, the velocity was set to zero and the density difference for each simulation is developed by adjusting temperature and adding concentration. Using the volumetric concentration C_v, the bulk density of the gravity currents is determined by Equation (2.2). The water density at temperature T (°C) is calculated using Equation (2.1). The temperatures and concentration for developing density difference in each block are shown in Table 4.2.

Table 4.2 Initial conditions of each computational domain.

Case #	Mesh block #1				Mesh block #2				
	Temp. (°C)	SS (mg/l)	C_v	ρ_d (kg/m^3)	Temp. (T °C)	SS (upper/lower)	C_v (lower)	ρ_o/ρ_1 (kg/m^3/ kg/m^3)	h_o/h_1 (cm/cm)
1	4	16100	0.00607	1010	4	0/32160	0.01214	1000/1020	10/10
2	4	4050	0.00153	1002.5	4	0/32160	0.01214	1000/1020	17.5/2.5
3	4	24110	0.00910	1015	4	0/32160	0.01214	1000/1020	17.5/2.5

The second simulation setup was arranged according to the experimental setup of Britter and Simpson (1981), as shown in Figure 4.3. Britter and Simpson (1981) determined that the propagation speed of a density current was sensitive to the ratio of current depth to the overall depth of fluid. This study contains simulations to confirm the effect of the ratio of current depth to overall fluid depth on propagation speed. A thinner or thicker intrusive gravity current was obtained by changing initial fluid depth filled behind the lock gate. Table 4.3 shows the experimental conditions for the second simulation setup.

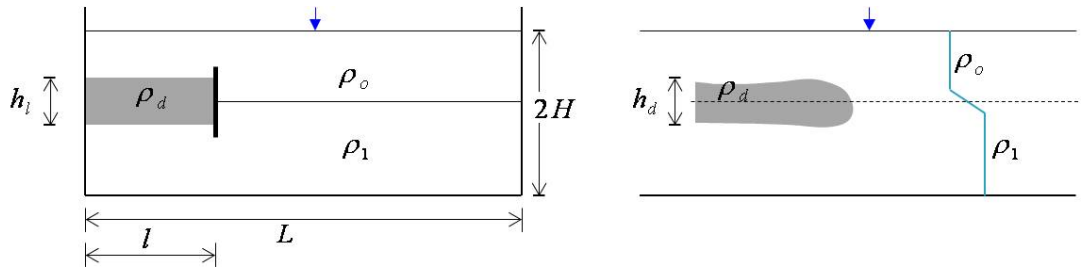

Figure 4.3 Experimental setup used to produce varying intrusion depth.

Table 4.3 Experimental conditions for the second simulation setup.

Case #	H (cm)	h_1 (cm)	L (cm)	l (cm)	ρ_1	ρ_o	$g' = \frac{1}{2} g(\rho_1 - \rho_o)/\rho_o$
4	20	0.04	500	50	1019.9	999.8	0.197
5	20	0.10	500	50	1019.9	999.8	0.197
6	20	0.14	500	50	1019.9	999.8	0.197
7	20	0.18	500	50	1019.9	999.8	0.197
8	20	0.20	500	50	1019.9	999.8	0.197
9	20	0.30	500	50	1019.9	999.8	0.197

4.2.2 Temporal evolution of intrusive currents

In the present numerical simulations, we employed both the RANS method with the renormalization group (RNG) $k-\varepsilon$ model (Yakhot and Orszag 1986) and Large-Eddy Simulation (LES) with Smagorinsky's sub-grid scale model (Smagorinsky 1963) for the flow analysis. LES simulation was limited only to one case due to long computational runtime. The transported concentration contributes to changes in the density in each of the numerical cells. The molecular diffusivity was neglected and only turbulent diffusivity was used to account for turbulent mixing effect. The value of turbulent diffusivity is computed using the ratio of eddy viscosity ν_t to turbulent Schmidt number Sc_t. For the present study, the most suitable value of Schmidt number for intrusive gravity currents was determined via calibration and validation processes using the laboratory experimental data. The sensitivity analysis of the RANS simulations to different turbulent Schmidt numbers demonstrated that the simulations with high Sc_t could provide very close agreement with the experimental results (see Appendix A.2).

For the first symmetrical cases (case 1: $\varepsilon = 0$, $\Delta = 0$), the simulation snapshots were created to visualize the temporal evolution of an intrusive gravity current. The simulation snapshots were compared with images taken from laboratory experiments of Sutherland *et al.* (2004) in

Figure 4.4. After the lock gate was removed, the fluid contained behind the lock gate collapsed symmetrically and propagated along the interface. The head already started to form and is visible at 2 s. The initial collapse began with rapid acceleration and the current head formed a uniform shape after 26 s. As it propagated to the right end of the wall, the head of the gravity current brought strong mixing, resulting in mass loss and dilution in the head. The temporal evolution was well illustrated with images taken from both experiments and numerical simulations, as shown in Figure 4.4. In order to identify the difference between 3-D and 2-D simulations, we additionally consider the 3-D simulation results in Figure 4.4.

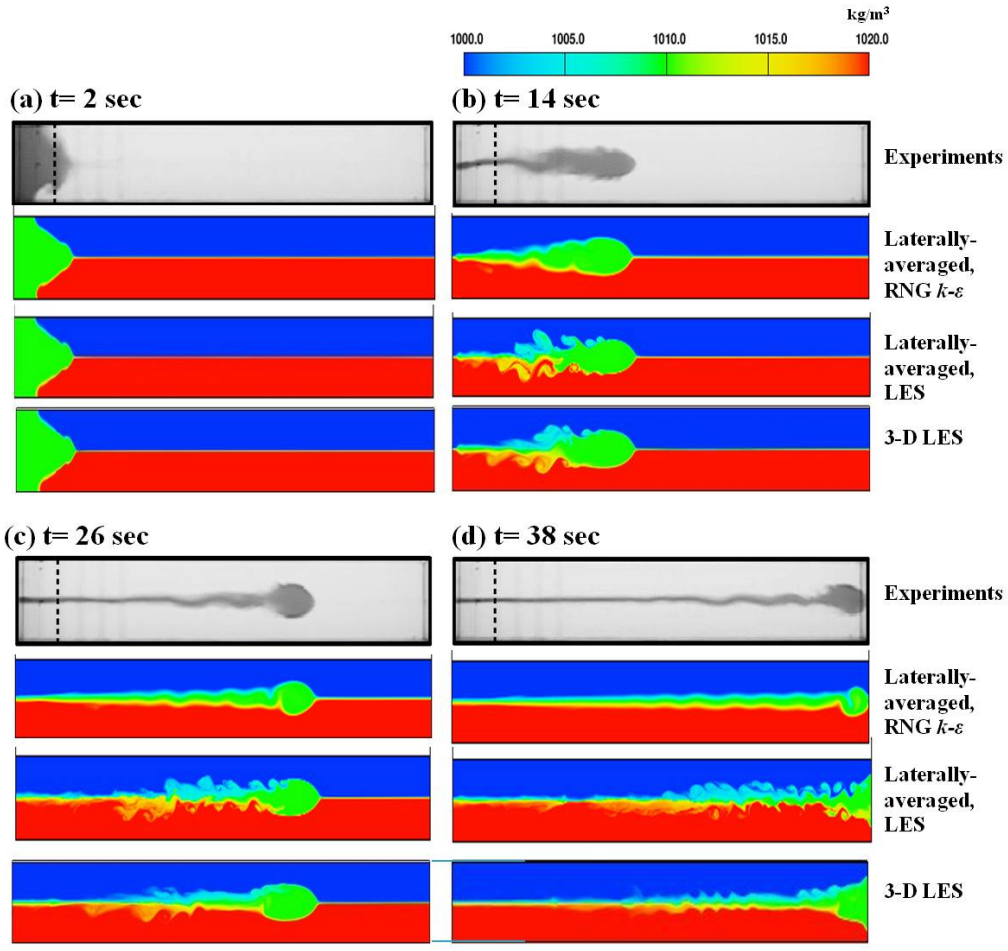

Figure 4.4 Temporal evolutions of an intrusive gravity current (IGC) for case 1 (symmetrical case) where experimental results of Sutherland *et al.* (2004) were visualized by adding dye. Density contours showing temporal evolutions in 2-D numerical simulations were calculated based on RNG $k-\varepsilon$ and LES. The 3-D results (x-z sections) were taken along the center line in the y-direction.

It is clear that the numerical model with RNG $k-\varepsilon$ and LES approaches predicts well the dynamics of an intrusive gravity current with the perfect symmetrical condition ($\varepsilon=0$, $\Delta=0$). It is also apparent that LES provides the information for the detailed turbulent mixing processes generated by the gravity current. The travel distances calculated by both RANS and LES are plotted as a function of time in Figure 4.5. This shows very good agreement with experimental measurements and the analytical solutions from Sutherland *et al.* (2004), Lowe *et al.* (2002), and Benjamin (1968).

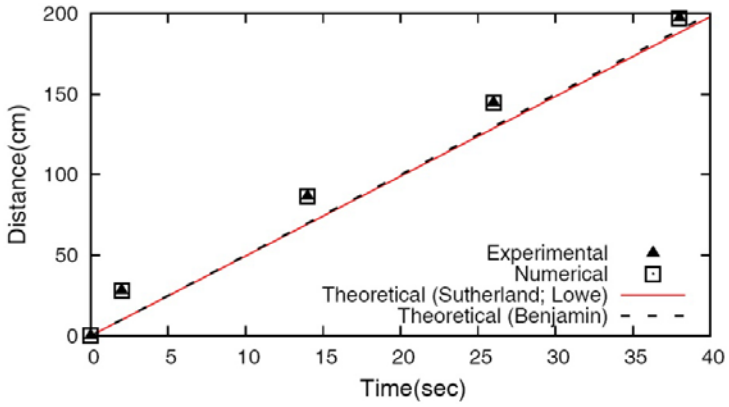

Figure 4.5 Traveling distance of IGC as a function of time in the simulation case 1. The marks indicate the numerical results from this study and experimental results from Sutherland *et al.* (2004). The solid line indicates the analytical solutions from Sutherland *et al.* (2004) and Lowe *et al.* (2002). The dashed line indicates the analytical solutions from Benjamin (1968). (h_d/H= 0.23 where the h_d was taken from the 3-D LES simulation result captured at 26 s).

In order to investigate the effect of Sc_t on the propagation dynamics of gravity currents, we conducted the numerical simulations with the value of Sc_t ranging from 0.2 to 50. Figure 4.6 provides the detailed information on the effect of the Sc_t on the turbulent mixing in stratified fluids (see Appendix A.2). No significant changes in density contour patterns were observed when the value of Sc_t was larger than 5. The simulations were compared with the experiments of Sutherland

et al. (2004) to present the values of Sc_t that are most suitable for intrusive gravity currents. The value of 5 or larger than 5 was found as a suitable turbulent Schmidt number for the simulation of intrusive gravity currents. Figure 4.6 illustrates that the propagation speed of the gravity current, determined from the slope of the lines, decreases with decreasing Sc_t. The decrease in Schmidt number means increasing turbulent diffusivity leading to the density decrease in the gravity current (i.e., the loss of buoyancy, resulting in velocity decrease as shown in Figure 4.6).

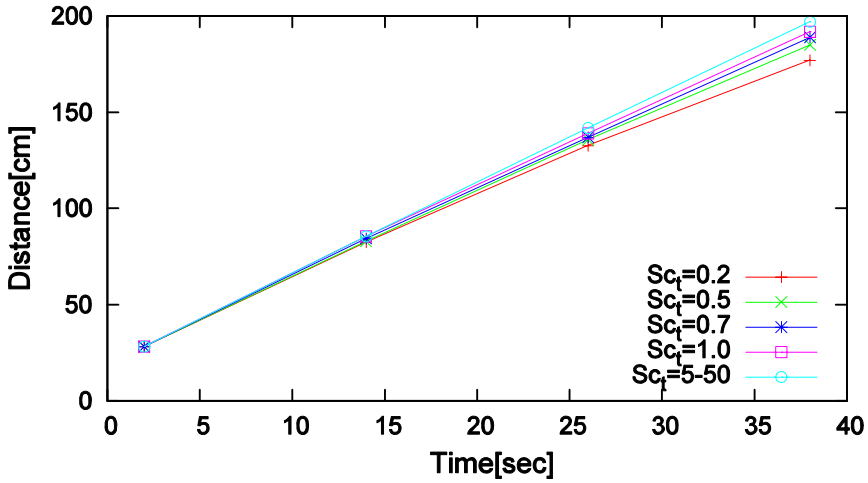

Figure 4.6 Effect of Schmidt number on the traveling distance.

In the second symmetrical case ($\varepsilon = 0$ and $\Delta \neq 0$), we observed different dynamics compared to the perfect symmetrical case. In this case, the propagation speed was observed to be slower than that of the gravity current in the first symmetrical case. In particular, the gravity current did not form a symmetrical head and body as it propagated. Interfacial instability occurred across the interface between the gravity current and the upper layer. Time series images captured from numerical simulations were compared with laboratory experiments in Figure 4.7. They indicated that the interfacial wave was probably negligible for the dynamics of the intrusion propagating into a two-layer fluid with symmetrical conditions.

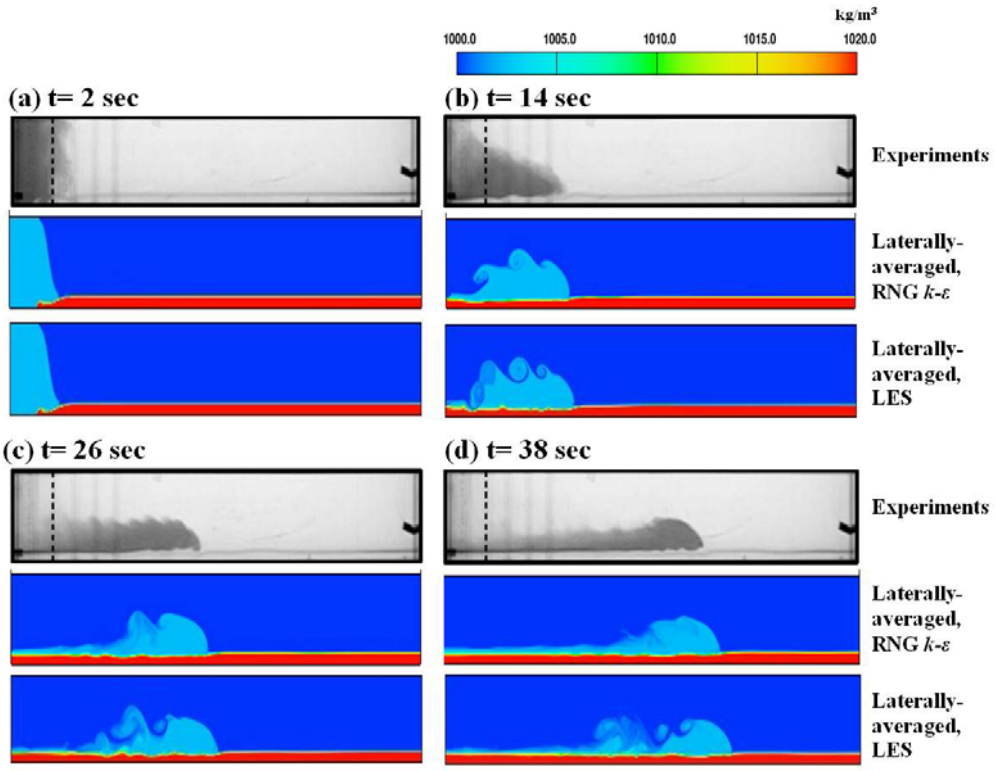

Figure 4.7 Temporal evolutions of an intrusive gravity current in second symmetrical cases ($\varepsilon = 0$ and $\Delta \neq 0$). (a) Experimental results of Sutherland *et al.* (2004), visualized by adding dye; (b) density contours showing temporal evolutions in numerical simulations based on RANS.

On the other hand, large amplitude internal waves, as is apparent from the images in Figure 4.8, were observed in simulations with asymmetrical condition. Figure 4.8 shows that the internal wave propagates faster than the propagation of the gravity current. In this case, it is not easy to predict the theoretical propagation speed because the process of developing waves including reflected waves strongly affects the dynamics of gravity currents.

The intrusive speed of IGC is one of the important parameters investigated through lock-exchange flow experiments. We plot travel distances at each measuring time using numerical results and the experimental results, shown in Figure 4.9. We assess the forecasting performance of the numerical model using absolute mean error (AME) and root mean square error (RMSE), as defined by

$$AME = \frac{1}{n}\left(\sum_{i=1}^{n}|M_i - S_i|\right) \tag{4.28}$$

$$RMSE = \sqrt{\frac{1}{n}\sum_{i=1}^{n}(M_i - S_i)^2} \tag{4.29}$$

where n = the number of data; M_i = field measurements; and S_i = simulation results. AME and RMSE for travel distances of IGC at each measurement time (t = 2, 14, 26,and 38 sec) are calculated to be 6.24 cm and 10.99 cm, based on the data shown in Figure 4.9. The numerical model shows good quantitative agreement for predicting intrusive speed and temporal and spatial evolutions of IGC.

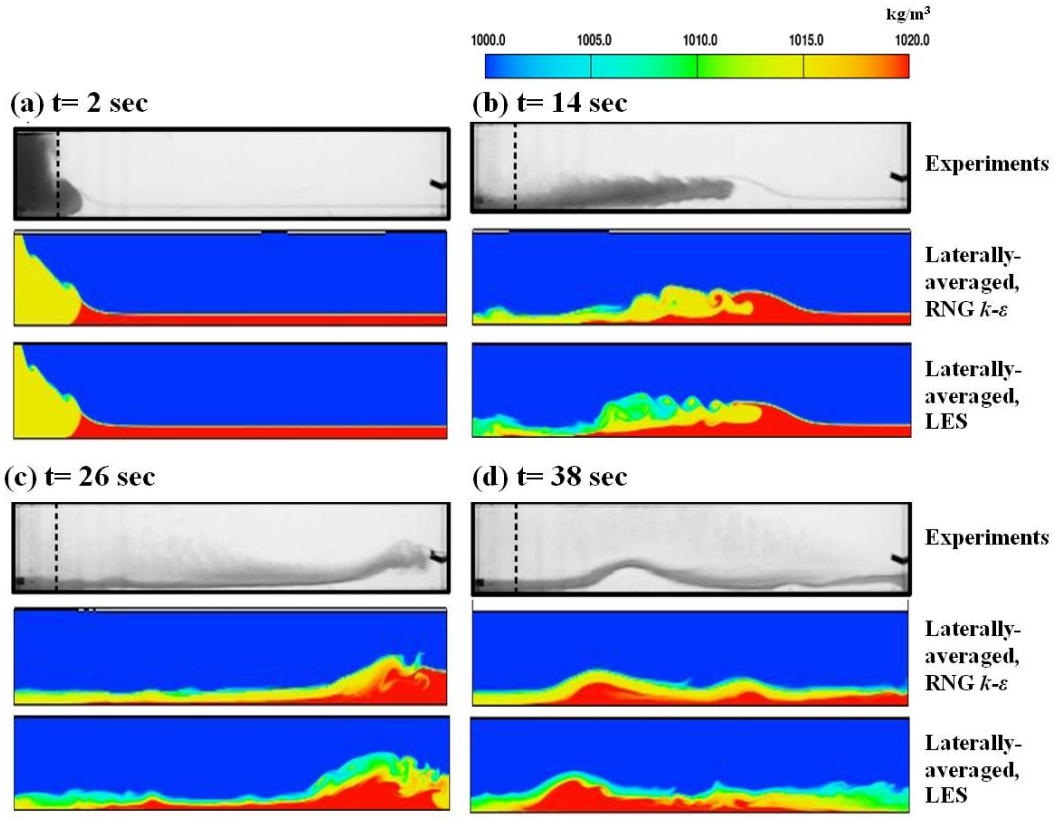

Figure 4.8 Temporal evolutions of an intrusive gravity current in asymmetrical case ($\varepsilon \neq 0$ and $\Delta \neq 0$). (a) Experimental results of Sutherland *et al.*(2004) , visualized by adding dye; (b) density contours showing temporal evolutions in numerical simulations.

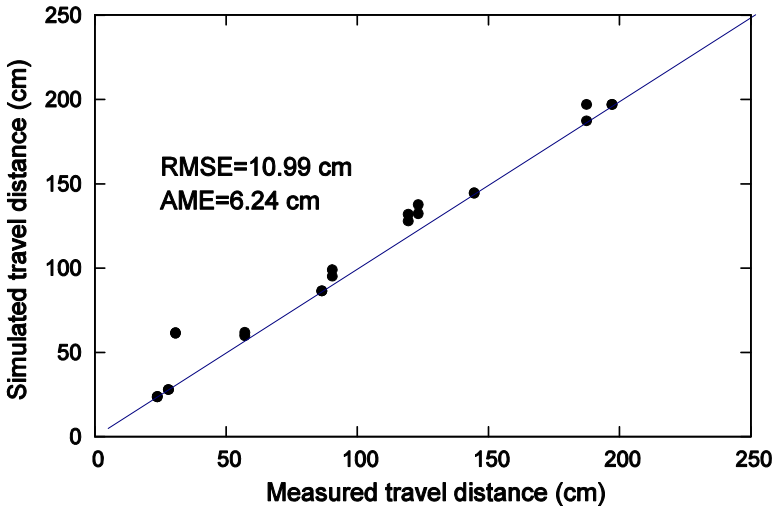

Figure 4.9 Quantitative evaluation of errors using AME and RMSE.

4.2.3 Effect of the ratio of current depth to the overall depth of fluid

One of our interests is to find the relationship between the propagation speed and the depth of a gravity current, because it is easier to set up field real-time monitoring system for the measurements of the depth rather than velocity of gravity currents. Then, we can calculate the propagation speed of gravity currents approximately using an empirical equation.

Keulegan (1957) described the motion of a gravity current with only the depth of gravity current and excess density between the current and ambient fluid. He suggested the empirical Equation (2.21) for predicting the propagation speed of a gravity current through many experiments on the gravity current propagating along a horizontal floor into fresh water. The empirical equation was derived from the experiments undertaken mainly based on the gravity currents occupying approximately 1/5 of total depth (i.e., $h_d / H = 0.2$).

Benjamin (1968) developed the theory of a gravity current entering a homogeneous fluid with a perfect fluid theory not without considering mixing between the fluids. Britter and Simpson (1981) extended the value of h_d / H in the range of 1/3 to 1/10. They found that the propagation speed of a density current was sensitive to the ratio of current depth to the overall depth of fluid. In

this simulation, we demonstrated the effect of the ratio of current depth to the overall depth of fluid. The ratio had the range from 0.045 to 0.3. The height of the interface of two fluid layers was chosen to be sharp. The range of a gravity current depth varied with adjusting initial condition. The detailed simulation setup is shown in Table 4.3. The dimensionless parameter, densimetric Froude number, is used to show the influence of the ratio of current depth and total water depth on the propagation speed of the gravity current. The densimetric Froude number of an intrusive gravity is given by

$$F_r = \frac{U_d}{\sqrt{g' h_d^{'}}} = f\left(\frac{h_d^{'}}{H'}\right) \tag{4.30}$$

where $\rho' = 0.5g(\rho_2 + \rho_1)$. If a gravity current intrudes into the interface of a two-layer fluid symmetrically, one half of current depth $h_d^{'} = h_d / 2$ and one half of total depth $H' = H / 2$ can be used to obtain the value of the Froude number. The variation of the Froude number (F_r) with the ratio of a current depth and total water depth is shown in Figure 4.10. We observed the Froude number varied considerably with the changes of $h_d^{'} / H^{'}$. The simulation results were plotted with experiments of Britter and Simpson (1981) and the analytical solutions from Benjamin (1968).

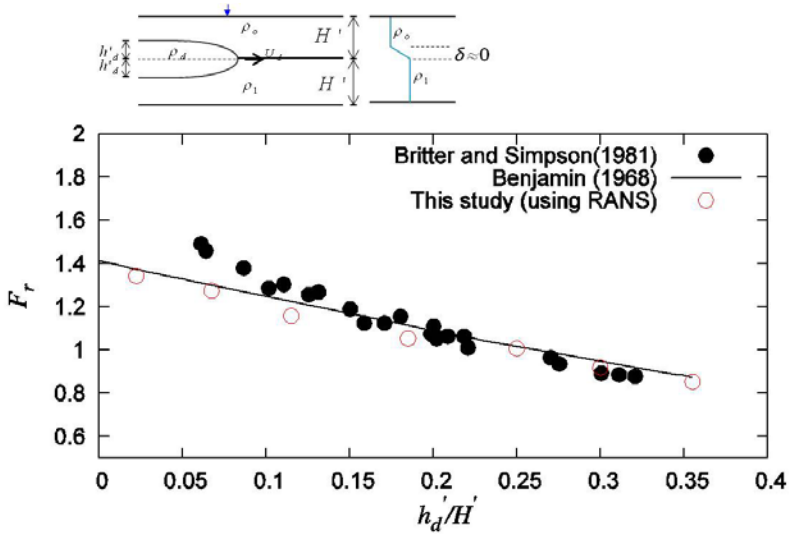

Figure 4.10 Variation of Froude number with fractional depth $h_d^{'} / H^{'}$.

We found simulation results showing good agreement with the theoretical curve from Benjamin's analytical solutions and laboratory experiments of Britter and Simpson (1981). Especially, the numerical results are more similar to the analytical values suggested by Benjamin (1968). Decreasing Froude number with increasing the value of $h_d^{'} / H^{'}$ was observed in these simulations.

4.3 IGC intruding into a Stratified Fluid

In this section, we consider intrusive gravity currents, propagating into a continuously stratified fluid, as frequently observed in nature (e.g., a reservoir, ocean, and river). The theoretical descriptions based on mass, momentum, and energy conservation were found in Cheong *et al.*(2006) and Bolster *et al.* (2008). Experimental studies also have been performed by Britter and Simpson (1981), De Rooij *et al.* (1999), and Lowe *et al.* (2002). In order to validate the numerical model, we compared the numerical simulations with theoretically predicted values and experimental measurements in Bolster *et al.* (2008).

4.3.1 Simulation setup

In order to simulate an intrusive current into a stratified fluid, we arranged dimensions and initial conditions, which corresponded to the experimental setup in Bolster *et al.* (2008). The dimensions are 182 cm long, 23 cm wide and 30 cm deep. The total fluid depth (H) is 20 cm. The lock gate is positioned at 30 cm forward from the right wall (see Figure 4.11).

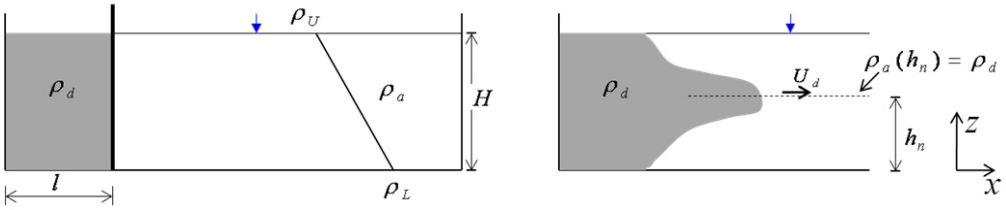

Figure 4.11 Intrusion with $\rho_d = 0.5(\rho_U + \rho_L)$ where the neutral level is at $h_n = 0.5H$.

In this simulation setup, the stratification gradient is uniform, given by $\rho_d(z) = 0.5(\rho_U + \rho_L)$ and h_n is the level where the ambient density ρ_a is equal to that of the intrusive current ρ_d. In a uniformly stratified fluid, Maxworthy *et al.* (2002) predicted that a gravity current would travel at a constant speed (U_d), which took the form

$$U_d = FNH \tag{4.31}$$

where $N = \sqrt{(-g/\rho_o)\partial\rho/\partial z}$ is the buoyancy frequency of the stratification, and ρ_o is the constant representative density. Maxworthy *et al.* (2002) and Ungarish (2006) experimentally determined the values of F equal to 0.266 and 0.25, respectively, by experiments. Bolster *et al.* (2008) carried out extensive experiments to determine how the propagation speed of gravity currents depended on the variation of density of gravity currents (or h_n). They suggested an analytical solution for determining the propagation speed using the assumption that a perfect conversion of energy occurs between the kinetic energy and potential energy as the density field adjusts.

$$U_d = \tfrac{1}{2}FNH\sqrt{12\left(\frac{h_n - \frac{1}{2}H}{H}\right)^2 + 1} \tag{4.32}$$

4.3.2 Effect of buoyant frequency (*N*) and intrusion location

We simulated gravity currents intruding into a continuously stratified fluid with the buoyancy frequency $(N = 1.0, 0.5)$. The numerical simulations were conducted for gravity currents propagating into a continuously stratified fluid over the entire range $0 \le h_n \le H$. The propagation speed of numerical results and experiments are shown and compared to the theoretical calculations in Figure 4.12. They show good agreements with theoretical curves calculated by the energy model in Bolster *et al.* (2008).

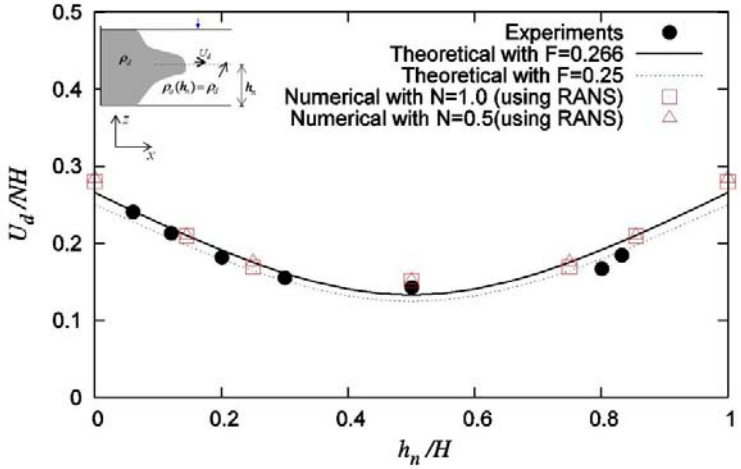

Figure 4.12 Comparison of dimensionless intrusion propagation speed (U_d / NH) **for numerical simulations (□, *N*= 1s^{-1}; Δ, *N*=0.5 s^{-1}) and experiments (●, from Bolster *et al.* 2008). The line and dashed line are the predictions by the energy model in Bolster *et al.* (2008).**

In numerical simulations, we observed that the gravity current propagated slower when the current traveled at mid-depth, while maximum speed occurred when it traveled either at the top or bottom.

4.4 Particle-driven Gravity Currents (PDGC)

PDGC are induced by loading with suspended particles. Turbidity currents in a reservoir or ocean are typical cases of particle-driven gravity currents. In the laboratory, a common procedure for generating PDGC is the sudden removal of a vertical partition separating particle-laden and clear fluid. In this section, we simulate some PDGC induced by different particle sizes. The simulation setup corresponds to a laboratory experiment of Gladstone *et al.* (1989). Particle settling velocity (ω_s) within the numerical model is simply modeled by Stokes' Law according to the defined particle density (ρ_s) and diameter (d_s).

$$\omega_s = \frac{g\, d_s^2}{18\,\nu}\left(\frac{\rho_s - \rho_w}{\rho_w}\right) = \frac{g\, d_s^2}{18\,\nu}\left(\frac{\rho_s}{\rho_w} - 1\right) \tag{4.33}$$

The temporal evolution of a particle field can then be treated in an Eulerian manner in a turbulent advection-diffusion equation.

$$\frac{\partial \phi}{\partial t} + \frac{\partial}{\partial x_i}(u_i \phi) = \frac{\partial}{\partial x_i}\left(\Gamma \frac{\partial \phi}{\partial x_i} - \overline{u_i' \phi'} \right) + \frac{\partial}{\partial z}(\omega_s \phi) \tag{4.34}$$

where Γ = diffusivity for property ϕ; ϕ = mean scalar; ϕ' = the corresponding fluctuating scalar, $\bar{}$ (Overbar)= averaging of fluctuating quantities; and ω_s = particle settling velocity. We assumed the forces induced by particle settling have a negligible influence on the motion of the fluid phase. Thus, the motion of the fluid phase is solved by the Navier-Stokes equation without two-way coupling between the particle fields and fluid phase. However, in order to describe the motion by particle-driven buoyant forces, the turbulent advection-diffusion equation is coupled with the Navier-Stokes equation through density gradient terms. Because we are interested in mixture flows with small mass loadings, the Boussinesq approximation, that the density variations affect only gravitational terms, is employed in the Navier-Stokes equation. The bulk density of gravity currents varies as a function of time due to the particle deposition and turbulent mixing, and the problem becomes more complicated.

The wall boundary is specified as non-tangential stress areas with a no-slip condition. However, the shear stress arising from tangential wall shear stresses probably contributes to the turbulent transport processes. Therefore, we should incorporate wall shear stress contributions into turbulent transport equations. In the numerical model, we assign values to the turbulent kinetic energy (k_t) and the rate of dissipation (ε_t), with the assumption of a local equilibrium between turbulent shear production and decay processes and a law-of-the-wall velocity profile.

4.4.1 Simulation setup

The setup for numerical simulations corresponds to Gladstone's experiments (1998), conducted in a glass flume tank. It has a dimension of 5.7 m long and 0.2 m wide, filled with tap water to a depth of 0.4 m (see Figure 4.13).

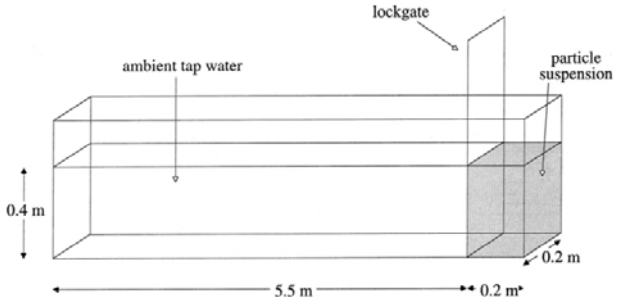

Figure 4.13 A schematic of the initial setup for PDGC (from Gladstone *et al.* 1998).

The density of silicon carbide particles (ρ_s) used to make the excess density is 3217 kg/m^3. The average particle size (d_s) used in the experiments is 25 μm and 69 μm. The concentration of particle suspension is set to be 11.2 kg/m^3. Reduced gravitational acceleration (g') was calculated to be 0.076 m/s^2. Considering Stokes' law, the settling velocities for each particle size are approximately 0.76 mm/s and 5.75 mm/s. We estimated settling time in a half depth (20 cm) of the total water depth for their sizes. The 25 μm and 69 μm particles totally settle to the bottom after 265 sec and 35 sec, respectively. Four simulations were performed with different proportions of coarse and fine particles (see Table 4.4).

Table 4.4 Simulation cases using mixtures comprising different particle sizes according to the proportions of each particle.

Runs	% Coarse(69 μm)	% Fine(25 μm)
A	0	100
B	50	50
C	80	20
D	100	0

4.4.2 Effect of the particle sizes on propagation speed

The temporal evolutions of PDGC were captured for the Runs A, D at t = 0, 5, 15, 25, and 30 sec with concentration contour, after the release of the particle added fluid (see Figure 4.14). During the initial collapse, the propagating gravity currents showed similar evolutions and almost constant velocity for all simulation runs. However, as the gravity currents traveled further, the gravity currents in each simulation run showed different speeds depending on each particle size fraction in a mixture. Figure 4.15 demonstrates the effect of the particle diameter as well as the amount of each particle size fraction on the propagation speed of the gravity current. We confirmed the particle diameter and particle size fraction play a dominant role in the dynamics of gravity currents generated by suspended particles.

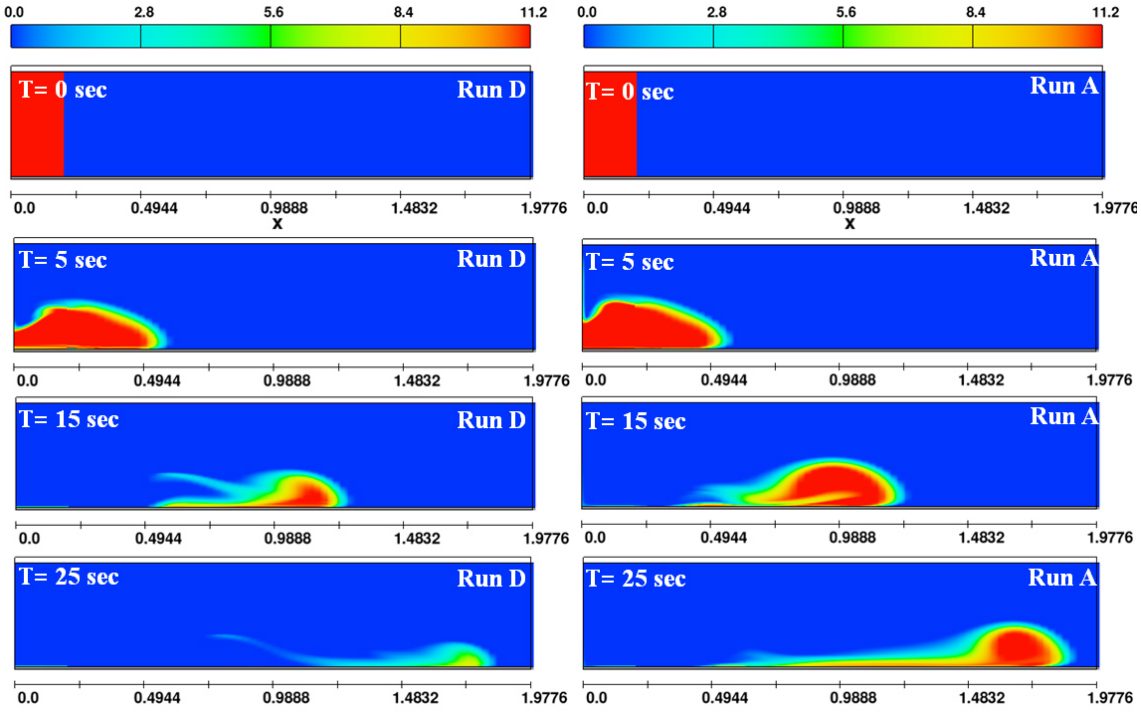

Figure 4.14 Simulated temporal evolutions of gravity currents, plotted with concentration shaded contours for simulation Run D (69 μm, 100%) and Run A (25 μm, 100%), based on RANS $k-\varepsilon$. (continued).

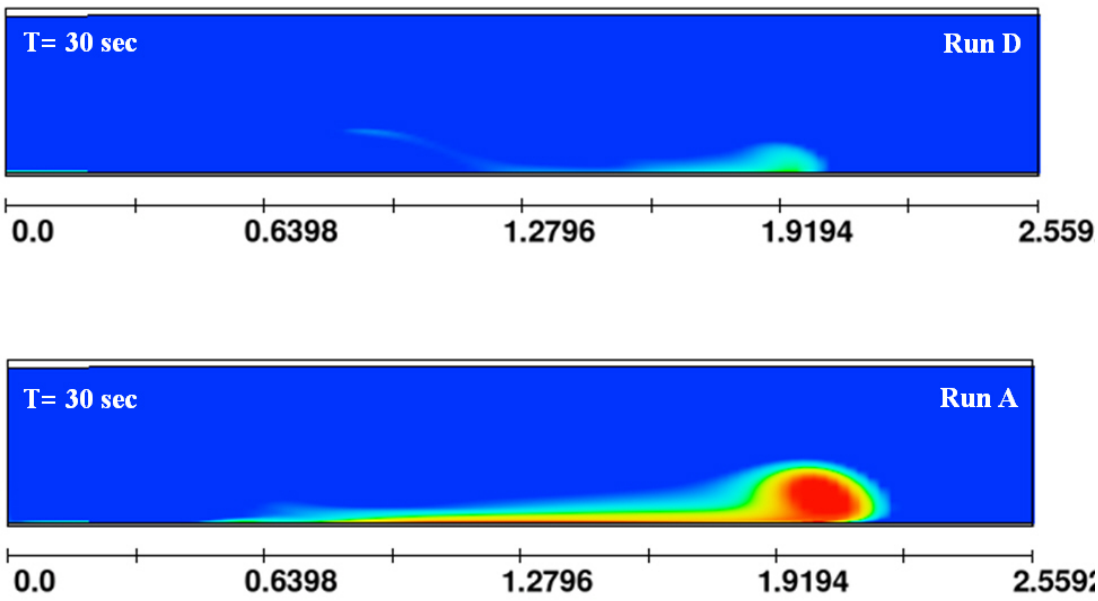

Figure 4.14 Simulated temporal evolutions of gravity currents, plotted with concentration shaded contours for simulation Run D (69 μm, 100%) and Run A (25 μm, 100%), based on RANS $k-\varepsilon$.

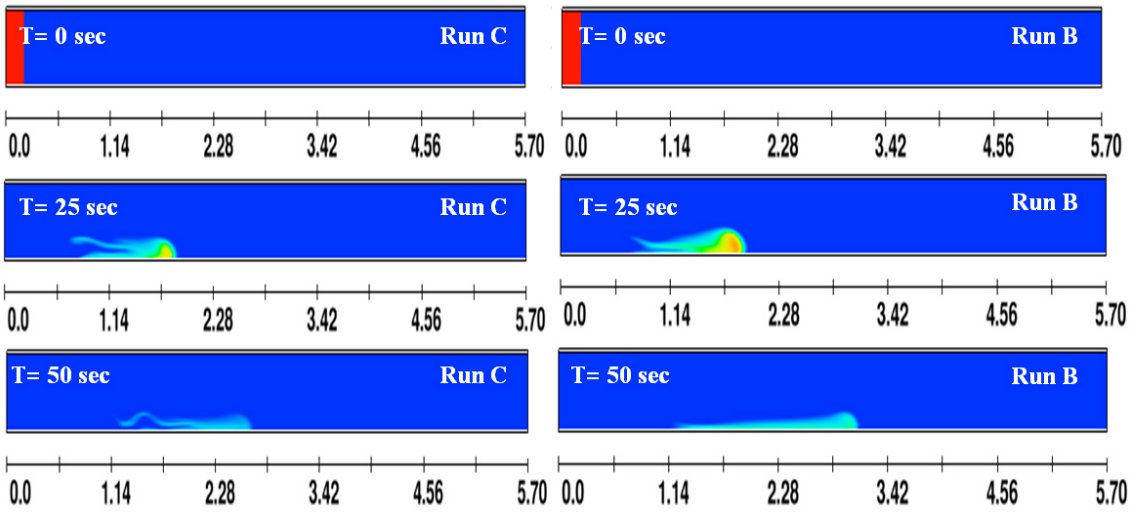

Figure 4.15 Simulated temporal evolutions of gravity currents plotted with concentration shaded contours for simulation Run C (69 μm 80%, 25 μm 20%), and Run B (69 μm 50%, 25 μm 50%), based on RANS $k-\varepsilon$.

The propagation speed is a main interest studied through these simulations. In Figure 4.16, we compared the simulated and observed current front position versus time. The numerical model successfully captured the decreasing propagation speed due to the different deposition rates between different particle sizes. The curve shows the constant slope during the slumping phase of gravity currents. In this flow regime, the velocity of currents remains constant regardless of the proportion of coarse and fine particles. After approximately 10 lock lengths from gate, the density current enters an inertia-buoyancy flow regime (Huppert and Simpson 1980). In the inertia-buoyancy flow regime, the propagation speed is decreasing in proportion to the increasing particle size. We observed that the divergence between experiments and numerical results was increasing with time. A possible reason for the observed divergence between experiments and numerical results might be the difficulty in modeling the mechanism for re-suspension from the bottom. In the numerical model, particles reaching to the bottom surface cannot be re-suspended. Therefore, the celerity calculations in the model are expected to be slightly lower than the laboratory measurement.

The transported concentration by the gravity current is plotted as a function of particle size at a fixed time t=100 sec, which was determined by considering the settling velocities of two particle sizes in the inertia-buoyancy flow regime (see Figure 4.17). The flow patterns of PDGC can be subdivided into three regimes describing the effect of particle size. The effect of particle settling velocity on the propagation speed of the PDGC is negligible at value of d_s less than about $10\,\mu\mathrm{m}$. The different deposition rates depending on d_s, however, significantly contribute to the dynamics where $10\,\mu\mathrm{m} < d_s < 40\,\mu\mathrm{m}$. When $d_s > 40\,\mu\mathrm{m}$, the PDGC rapidly lose their momentum to go forward due to their fast settling velocities.

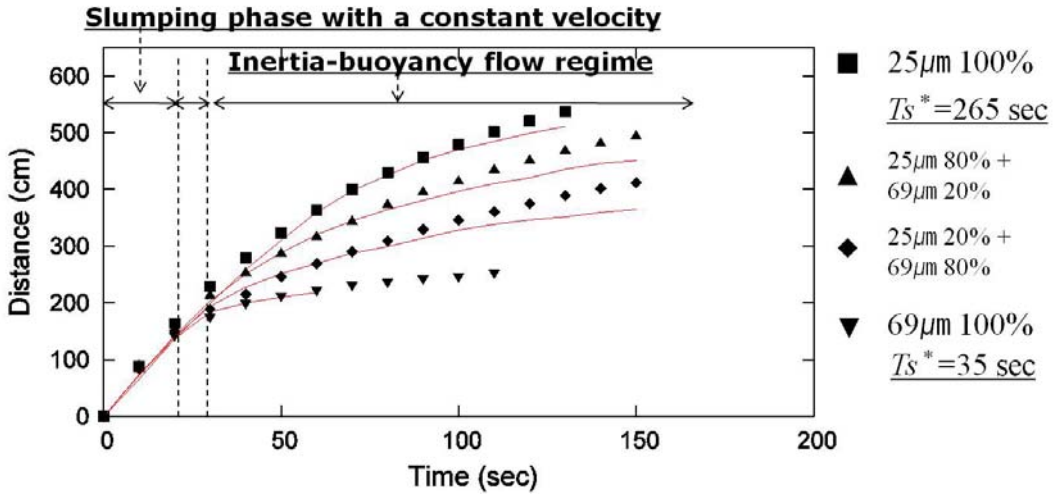

Figure 4.16 Traveling distance as a function of time. The filled marks indicates the percentage of coarse (69 μm) and fine (25 μm) size fractions by mass comprising each experimental flow. The *Ts indicates particle settling times for the half depth (20 cm) according to Stokes′ Law. The lines indicate the numerical results using RANS.**

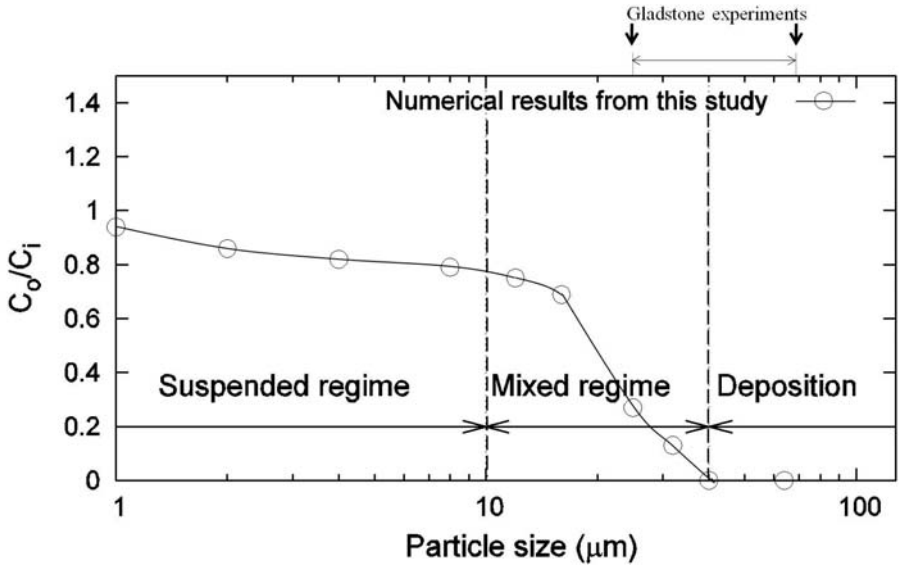

Figure 4.17 The transported concentration by PDGC as a function of particle size at t=100 sec. C_i is initial concentration of the fluid inside the lock. C_o is the concentration horizontally transported at t=100 sec by PDGC.

4.5 Conclusions

In this chapter we explore the propagation dynamics of gravity currents using a three-dimensional, non-hydrostatic numerical model. The numerical simulations focus on two different types of density flows (IGC and PDGC). In the study of IGC, the evolution profile and intrusive speed are compared with laboratory experiments and analytical solutions. The numerical model shows good quantitative agreement for predicting temporal and spatial evolutions of IGC. In particular, the simulated propagation speed is exactly equal to the experimental measurements in simulation case 1. In the study of PDGC, the FLOW-3D model has been modified to include particle dynamics: The new algorithm has been tested and it successfully captured the decreasing propagation speed due to the different deposition rates depending on particle size. The ratio C_i / C_o of transported to initial concentration of the gravity current varies as a function of the particle size d_s. Particle transport by gravity currents can be subdivided into three regimes: (1) The effect of particle deposition rate on the propagation dynamics of gravity currents is negligible when d_s is less than about $10\,\mu$m. In this regime, the fluids can be treated as homogeneous and the simulations of IGC and PDGC are expected to produce similar results; (2) Deposition rates significantly change the flow dynamics when $10\,\mu\text{m} < d_s < 40\,\mu\text{m}$; and (3) The PDGC will rapidly lose forward momentum due to their fast deposition rates when $d_s > 40\,\mu\text{m}$. We have presented three-dimensional simulations of intrusive gravity currents propagating into a two-layer fluid and a continuously stratified fluid, respectively. RANS with a RNG $k-\varepsilon$ model was employed to simulate turbulent flows. The numerical simulation results were compared with experimental data. The comparison shows that the numerical model based on either RANS or LES can predict realistic physical processes of gravity currents.

Chapter 5

Site Description and Field Measurements

5.1 Introduction

In this chapter, we present a description of Imha Reservoir and an analysis of field measurements. Field measurements are used as input for simulation setup and field validation. The data for setting up numerical simulations are sampled and transmitted in real-time at one- or two-hour intervals from gauging stations. Real-time gauging stations provide the field data on turbidity, temperature, and water level at every 1.0 m depth interval. The analysis of some important field data contributed to better understanding of the turbid density flows in the reservoir.

5.2 Site Description

Imha Reservoir is located (36^{o} 32' N; 128^{o} 53' E) in the northeastern part of the Nakdong River basin and was completed in 1992. It is the major water source for the northern Gyeongbuk province, with various water supply purposes, as shown in Figure 5.1.

Figure 5.1 Basin map of Korea (from Bae *et al.* 2008)

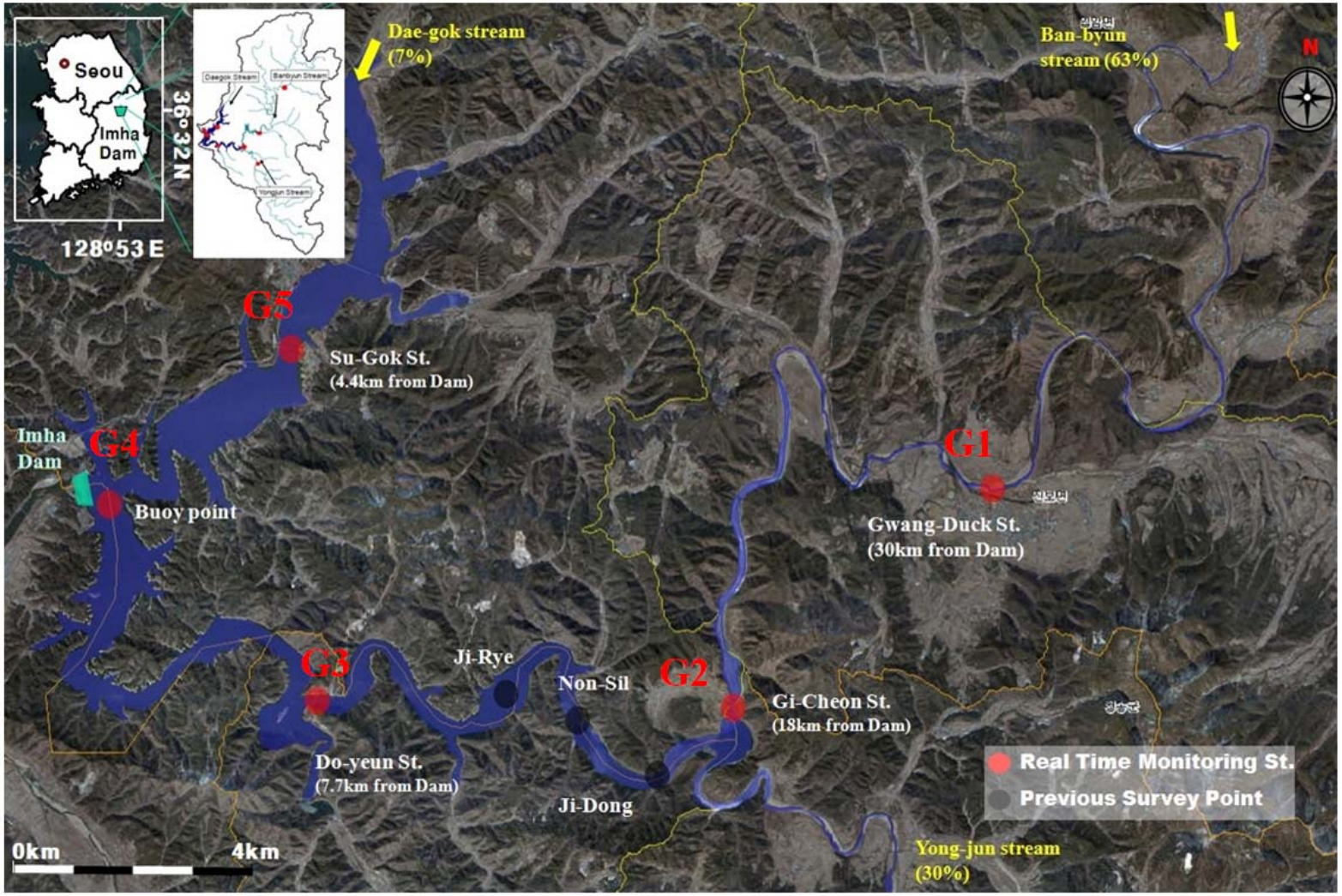

Figure 5.2 The satellite image for Imha Reservoir location with monitoring gauging stations.

Its capacity for annual water supply almost reaches 497×10^6 m^3 and flood control with 80 $\times 10^6$ m^3 among the total storage of 595×10^6 m^3. It also contributes to the annual power generation of 96.7 GWh. The watershed area of Imha Reservoir is about 1361 km^2, drained by three major tributaries: Ban-byun Stream, Yong-jun Stream, and Dae-gok Stream. The Ban-byun Stream is the principal tributary flowing into Imha Reservoir, which has 63 % of the total watershed area. The Yong-jun Stream is the second large tributary, which drains about 30 % of the total watershed. The reservoir shows morphologically complex characteristics. It has a comparatively long and narrow river with a 0.2 % bottom slope and the width ranging from 300 m to 1000 m. Maximum water depth is about 58 m near the dam site. Mean annual rainfall was measured at 1248 mm, 1089 mm, and 1029 mm, respectively, at three stations located near Imha Reservoir, based on hydrological observation over 20 years.

Kim (2006) estimated that the annual average soil loss rate was approximately 3450 ton/km^2 using USLE. Typically, the largest soil loss occurs during severe rainfall events such as a typhoon. Kim (2006) predicted the soil loss rate during Typhoon Maemi in 2003 to be 1330 ton/km^2. One of the main reasons for the high soil loss rate in Imha watershed is that the watershed has weak resistance to soil erosion as a result of geology and land cover conditions (Lee and Cho 2004). The large soil loss during severe flood events probably triggers the intrusion of highly turbid water into the reservoir. Furthermore, the turbid water may contain a large nutrient load, resulting in water quality degradation such as dissolved oxygen (DO) depletion and algal blooms by eutrophication. As mentioned in Chapter 1, Imha Reservoir has suffered from water quality problems induced by the intrusion of highly turbid water since 2002. The highest turbidity was recorded during Typhoon Rusa in 2002, Maemi in 2003, and Ewiniar in 2006 with 882 NTU, 1221 NTU, and 1055 NTU, respectively (see Figure 5.5).

5.3 Field Measurements

Real-time gauging stations were installed at five stations by the Korea Water Resources Corporation (K-water) to monitor turbid density currents propagating from each of the tributaries into the reservoir (see Figure 5.2). The monitoring device works with a data logging system to store the measured data of temperature and turbidity (NTU, Nephelometric Turbidity Units), pH, conductivity, and DO at every 1.0 m depth interval, installed by winch-type method. The data are transmitted in real-time at one or two hour intervals from the gauging stations to the Dam Integration Information System (DIIS) of K-water using the Mugunghwa satellite (see Figure 5.4). The turbidity sensor (Troll 9000, shown in Figure 5.3) provides resolution of 0.1 NTU with accuracy ± 5 % of reading or 2 NTU, whichever is greater.

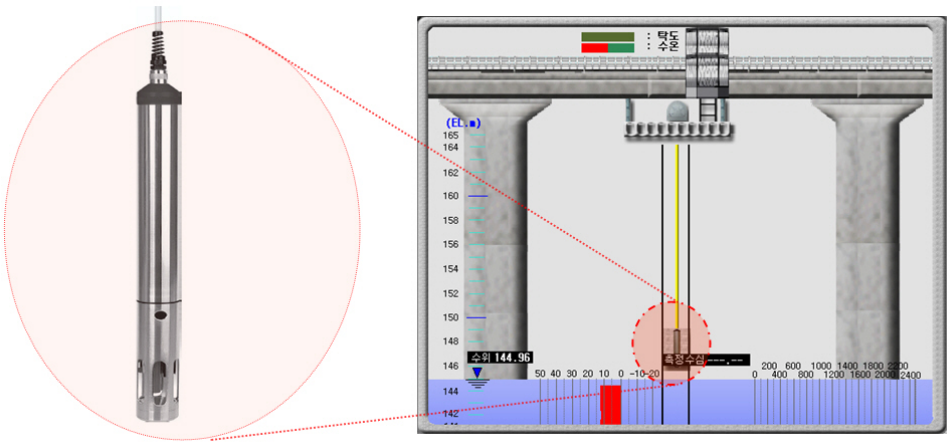

Figure 5.3 Turbidity measurement device (In-situ Inc. troll 9000) installed at the G2 station.

The optical sensors feature self-cleaning wipers to cleanse the sensors every hour. It is also compatible with the real-time data logging systems. In the sensors, NTU is measured using a light source with wavelength 870 nm and an angle of 90 ° light scattering between detected and emitted radiation. The sensor can measure the range from 0 up to 2000 NTU. The type of temperature

measurement is a platinum resistance thermometer. The range for temperature measurement is from -5 °C to 50 °C, with ± 0.1 °C accuracy and 0.01 °C resolution.

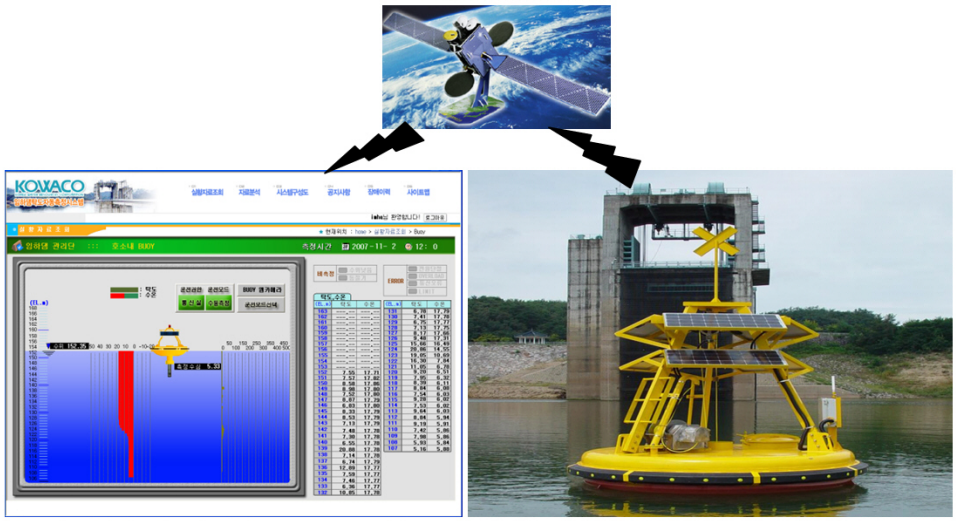

Figure 5.4 Real-time monitoring system for Imha Reservoir installed and has been operating by K-water since 2006.

The highest turbidity in Imha Reservoir was recorded during Typhoon Rusa in 2002, Maemi in 2003, and Ewiniar in 2006 with 882NTU, 1221NTU, and 1055 NTU, respectively (see Figure 5.5).

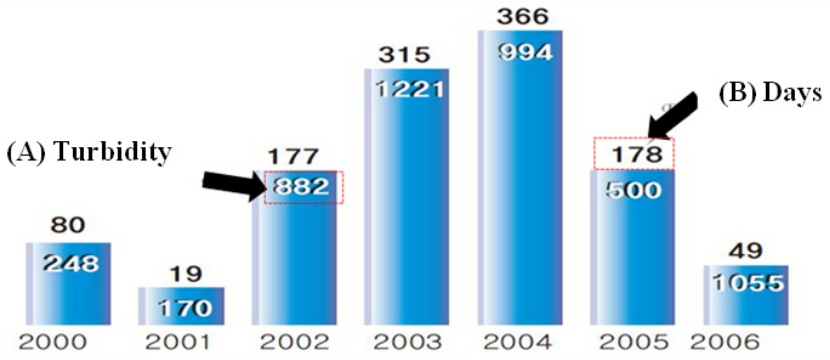

Figure 5.5 Maximum turbidity records reported during each year at Imha Reservoir. (A) indicates maximum turbidity (NTU), (B) indicates the total number of days with records above 30 NTU.

The gauging stations G2, G3, and G4 represent the characteristics typical of three zones of the reservoir: riverine, transitional, and lacustrine zone (see Figure 5.6). The riverine zone, upstream of G2, is well mixed and not stratified. The lacustrine zone between G3 and G4 shows a stable stratification with a thick hypolimnion. The transitional zone between G2 and G3 is the region between the riverine zone and lacustrine zone, showing weak stratification with a thin hypolimnion or no stratification. The downloaded data from the DIIS are used to set initial and boundary conditions for the numerical simulations, and to validate the numerical model.

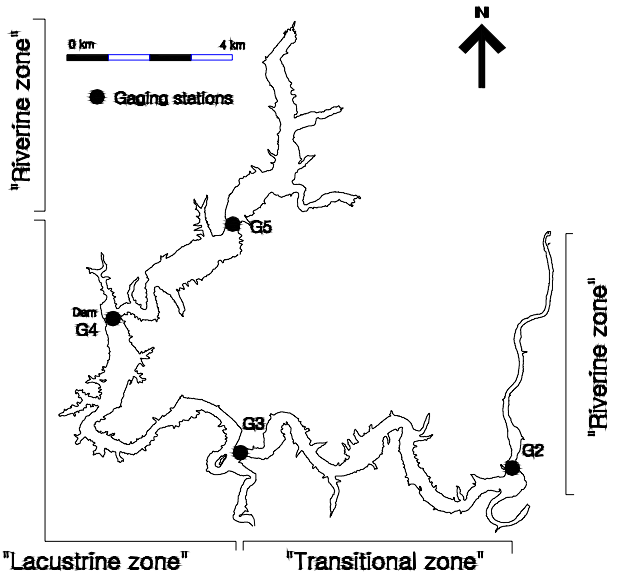

Figure 5.6 Topographic map of Imha Reservoir with the location of the measuring stations, representing zones divided into three regions: "Riverine", "Transitional", and "Lacustrine" .

5.3.1 Seasonal Stratification

Imha Reservoir has a stable thermal stratification during summer. Figure 5.7 shows a series of monthly thermal profiles measured near the Imha Dam during three years. The field measurements indicated that the continuous temperature gradient typically starts to form from April or May due to increasing solar energy and heat transfer into the layers below the water surface. In June or July, however, the temperature gradient was not as continuous as it was in April

or May. As the increased heating and wind-driven mixing occurs on the water surface, the epilimnion developed approximately 5~10 m below the water surface. Below the developed epilimnion, the temperature gradient continued to increase during summer and reached strong stratification at the end of July. The depth of the temperature gradient (i.e., metalimnion) was observed to reach about 10-15 m. Thus, we can observe the water column divided into three layer zones (i.e., epilimnion, metalimnion, and hypolimnion) during summer.

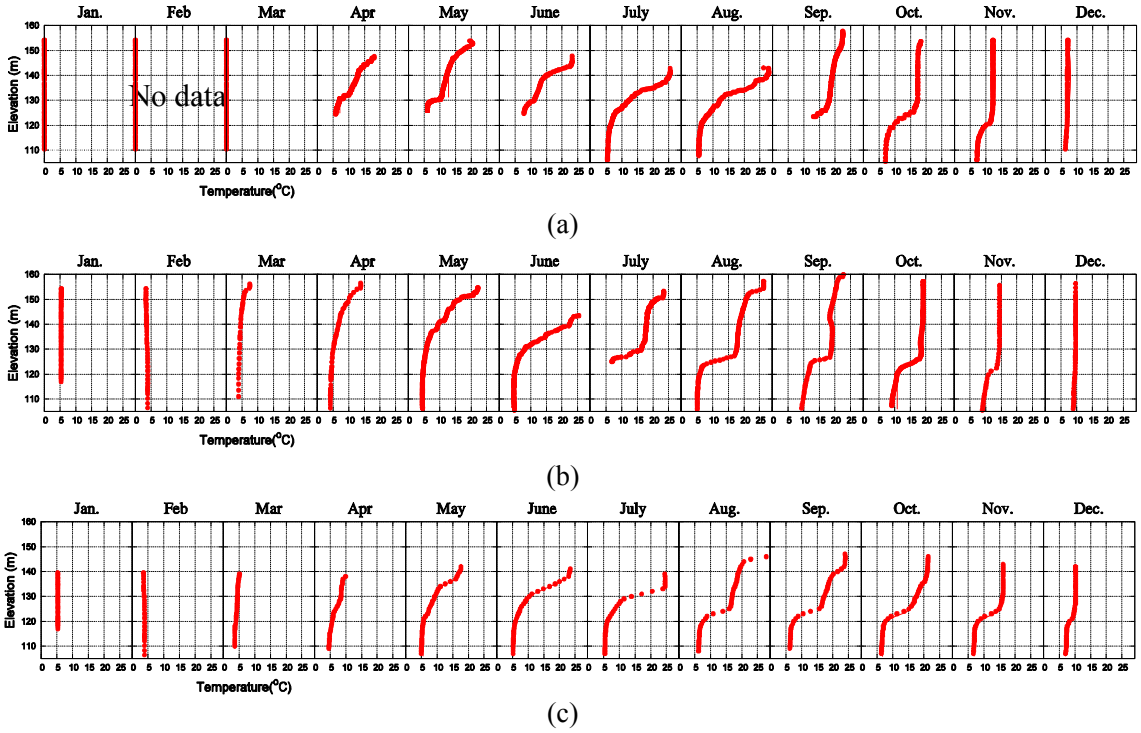

Figure 5.7 Seasonal variation in water temperature, Imha Reservoir, South Korea; (a) Typhoon Rusa on August 20, 2002, (b) Maemi on September 11, 2003 and heavy rainfall events during July, (c) Typhoon Ewiniar on July 10, 2006.

During summer, the reservoir generally experiences a large increase of surface water level during severe flood events such as typhoons or monsoon rains. During severe flood events, the metalimnion increased with the decreasing temperature gradient. This variation of temperature profile in the metalimnion explains well that most inflows intrude into the metalimnion of the reservoir during the severe flood events. These intrusive gravity currents displaced the original

metalimnion and accelerated mixing across the vertical layers, resulting in a decrease in temperature gradient vertically. The change of the temperature gradient of the metalimnion means the breakdown of the stratification structure. This is accountable for some turbulent mixing induced by the large intrusions, leading to the water column mixing in the metalimnion. The occurrence of a new sharp metalimnion was observed along the interface between the intrusion layer and hypolimnion when the intrusive turbid density currents approached the dam.

We can predict the elevation of the intrusions entering into the metalimnion using simple calculations. The inflow temperature decreases down to 17~18 ^{o}C after rainfall events and accompanies fine sediments generally in the amount of 500- 1000 mg/*l* (only washload) in Imha Reservoir. Thus, we can estimate the density of the inflow entering into the reservoir using Equations (2.1) and (2.2). Table 5.1 shows the temperature of clear water having an equivalent density to the mixture water depending on sediment concentration, to be 17 ^{o}C.

Table 5.1 Temperature of clear water having an equivalent density to the mixture water depending on sediment concentration in 17 ^{o} C.

Sediment Concentration, (mg/*l*)	0	250	500	1000	1500	2000
Mixture water density in 17 ^{o}C temp., (kg/m^{3})	998.8	998.9	999.1	999.4	999.7	1000.0
Clear water temp. equivalent to the mixture water density, (^{o}C)	17.0	16.1	**15.1**	**12.9**	10.0	4.0

Therefore, we can predict the turbid density currents, consisting of SS = 500 ~ 1000 mg/*l* and 17 ^{o}C water in temperature, will move horizontally through the ambient reservoir at the elevations where the water temperatures range from 13 to 15 ^{o}C. In the right figure of Figure 5.8, the shaded zone indicates the predicted intrusive elevation of turbidity currents in accordance with the calculation of Table 5.1. However, mixing by many factors (e.g., resistance of stratified fluids interface and boundary, meandering effect, etc) can dilute the density currents, resulting in loss of

excess density. Thus, they may propagate at a little higher elevation due to the loss of excess density. Field measurements support these assumptions in Section 5.3.3.

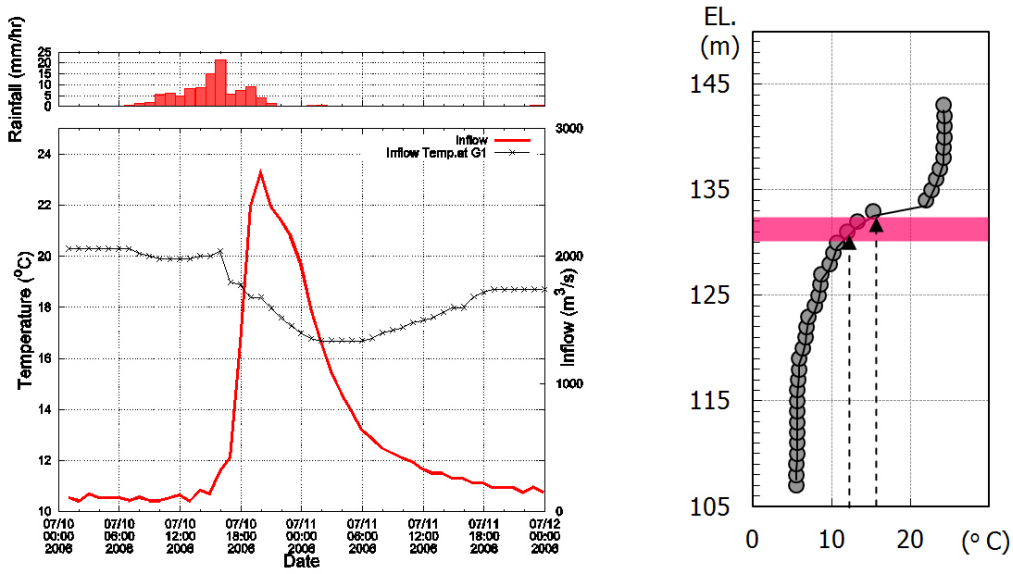

Figure 5.8 Plot of the variation of inflow discharge and temperature with respect to time in Imha Reservoir during Typhoon Ewiniar. (Left) temperature and river discharge during the flood event. (Right) thermal structure at the dam site. In left figure, the shaded zone indicates the predicted intrusive elevation of turbidity currents in accordance with the calculation of Table 5.1.

5.3.2 Meteorological and Hydrological Datasets

A typhoon with strong winds develops the surface stress, increasing mixing in the whole reservoir by the production of surface waves. The wave motion causes transfer momentum to water columns, leading to mixing below the water surface. The mixing is generally active in the epilimnion. However, it may occur even in the thermocline and hypolimnion by the development of internal waves, leading to vertical mixing. Mixing due to weak winds stems from active production of turbulence via waves breaking on the water surface. Continuously strong wind may cause tilting of the metalimnion (i.e., the occurrence of baroclinic pressure gradient), leading to internal waves.

We investigated the response of Imha Reservoir to the wind forces during Typhoon Ewiniar in 2006 using field measurements. Figure 5.9 shows measurements of the wind speed and direction during seven days including Typhoon Ewiniar event. The changes in wind direction and speed, as observed before, during, and after the typhoon, were plotted on the Imha Reservoir map (see Figure 5.10).

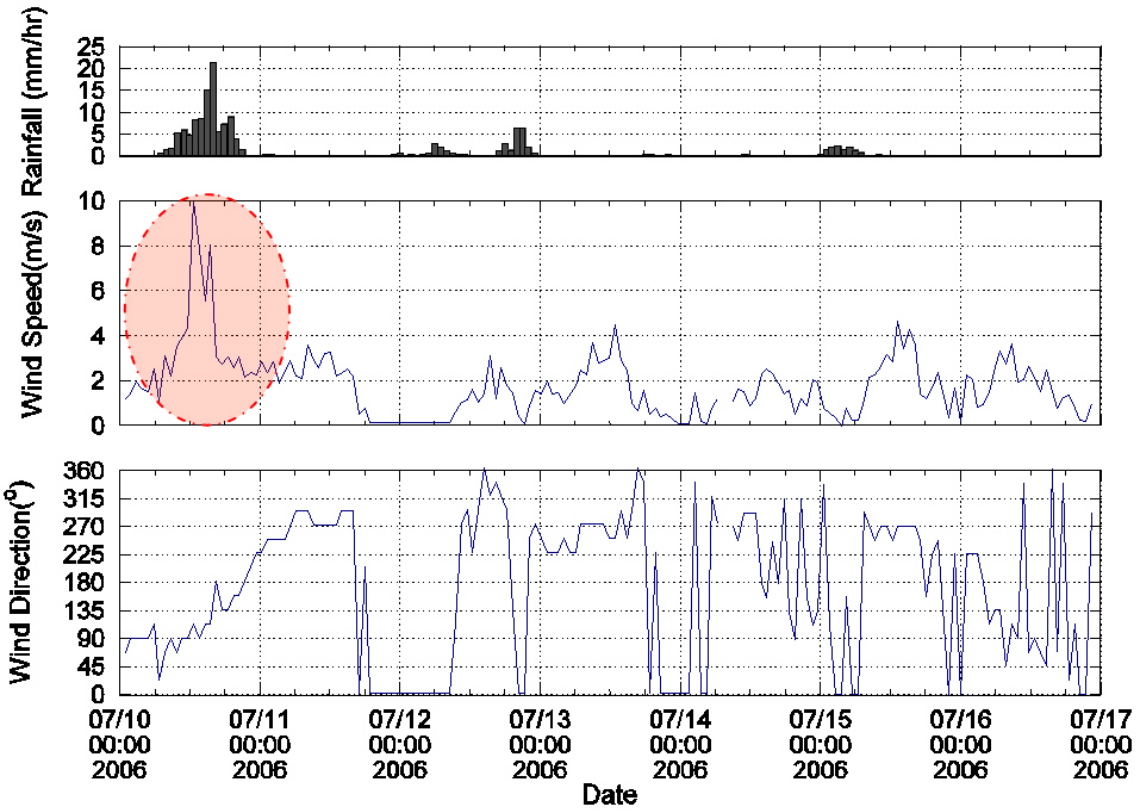

Figure 5.9 Meteorological data during Typhoon Ewiniar. The shaded circle are for the duration of the typhoon passing Imha Reservoir.

The Imha Reservoir has a relatively short length of the lacustrine part (3 km long and maximum 0.7 km width). During the typhoon, the maximum wind was mainly blowing westward over a relatively short fetch distance (about 0.6 km). In order to investigate the effect of winds on the structure of temperature profile by wind mixing in Imha Reservoir, we plotted the temperature profiles using the field measurement data before and after Typhoon Ewiniar in Figure 5.11. If the

wind-driven forces during the typhoon were not negligibly small, there would be a significant change in the temperature profile.

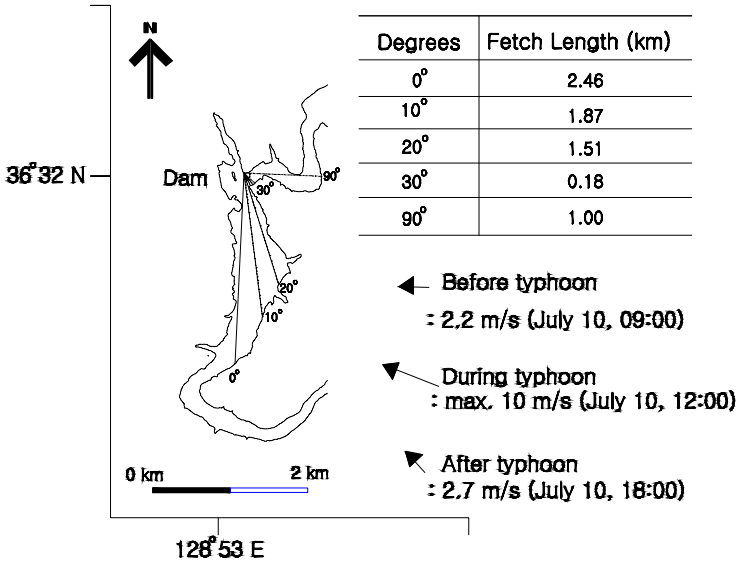

Figure 5.10 Map of Imha Reservoir with wind speeds and directions before, during, and after the typhoon. The fetch distances were computed.

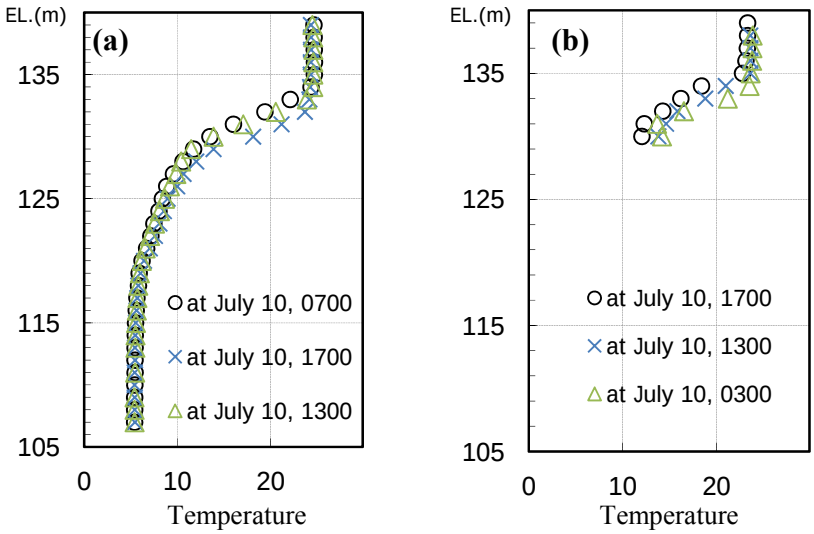

Figure 5.11 Temporal variations of temperature profiles. (a) measurements at G4, (b) measurements at G5.

As shown in Figure 5.11, however, the changes in temperature profiles during the time when the typhoon was passing over the reservoir were negligibly small. The possible reason for the small discrepancy between the temperature profiles in Figure 5.11 was that the wind was blowing in the direction of the short fetch during the typhoon. It was not sufficient to develop surface waves, accelerating vertical mixing. Figure 5.11 clearly illustrates that the effect of wind-driven forces can be negligible during the simulation periods. All other data (e.g., reservoir inflow, outflow, surface water level, wind, rainfall, and air temperature etc.) are available on the web at www.wamis.go.kr.

5.3.3 Turbidity

Turbidity is an optical property of fluid containing particles, expressed in terms of the amount of light that is scattered by particles in the fluid. The measurement unit for turbidity is called Nephelometric Turbidity Unit (NTU). For simulation setup (i.e., for setting up initial and boundary conditions) and field validation, the field measurements are taken from the real-time measuring system. Figure 5.12 illustrates the turbidity and rainfall changes during Typhoon Ewiniar in 2006 at the 5 field monitoring stations. Turbidity increased with increasing rainfall up to 2400 NTU at G1 on July 10 20:00, while the river inflow temperatures dropped from 20 ^{o}C to 17 ^{o}C (see Figure 5.8). The peak NTU at G1 finally arrived at the Imha Dam (G4) after 1 day (travel a distance of 30 km in 1 day, V = 0.35 m/s).

As the turbid inflows proceeded into Imha Reservoir, the magnitude of peak NTU decreased due to mixing, dispersion, and sediment particles settling. The incoming turbid water moved with relatively fast speed over the distance between G1 and G2 (12 km in 2 hours, V = 1.67 m/s), while the turbid water moved slowly over the distance between the inlet of Imha Reservoir G2 and the Imha Dam wall G4 (travel a distance 18 km in 22 hours, V = 0.23 m/s). In the section between G1 and G2 (“Riverine zone”), the river is characterized with good mixing, narrow width, and shallow depth, resulting in fast propagation.

On the other hand, in the section between G2 and G4 ("Transitional zone" and "Lacustrine zone"), the turbid water becomes density currents, propagating horizontally (i.e., intrusive gravity currents). After the currents arrive at the dam wall G4, the propagation speed of the density currents moving from G4 to G5 becomes much slower (V = 0.04 m/s) and their forward movement is generally determined by inertial and buoyant forces. In this regime the currents need a continuous inflow and/or outflow to sustain the movement, or their movements are delayed and finally vanish. In the section between G2 and G3 ("Transitional zone"), plunging flows may occur. They happen generally at the points where the momentum of incoming flows and the pressure gradient across the interface separating the incoming flows and ambient water of a reservoir meet a balance with resisting shear forces. After plunging to the bottom of the river, they propagate as an underflow and they propagate horizontally at the separation point where the currents lift off the bottom.

Figure 5.13 and Figure 5.14 demonstrate longitudinal concentration distributions along the thalweg of the reservoir during Typhoons Rusa (8/30/2002) and Maemi (9/11/2003). Intrusions, indicative of horizontal propagation of turbid density currents into a stratified reservoir, are indentified in the field observations. It is also well shown that autumn turnover can occur when very fine sediments still remain until the late autumn. The turbid density currents triggered by severe rainfall events contains many different grain size of suspended sediments. This strongly influences the sedimentation processes. Very small sediments such as clay or very fine silt take a long time to settle. In the late autumn, the temperature of a reservoir becomes uniform vertically and then the reservoir gets mixed easily by the development of external forces (e.g., wind forces, inflow momentum). Figure 5.13 (b) and Figure 5.14 (b) show the increasing turbidity in the discharge water from the reservoir due to the autumn turnover.

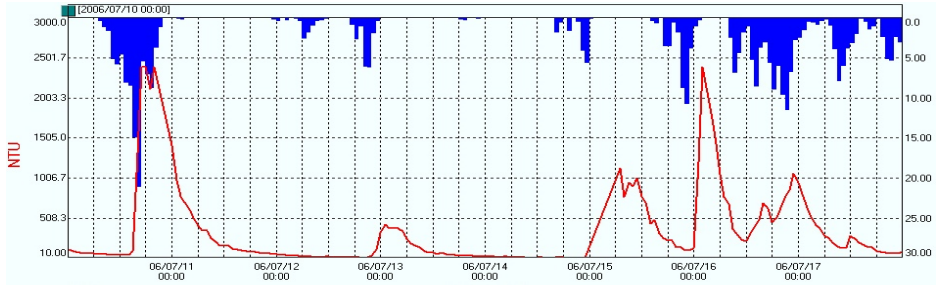

(a) G1

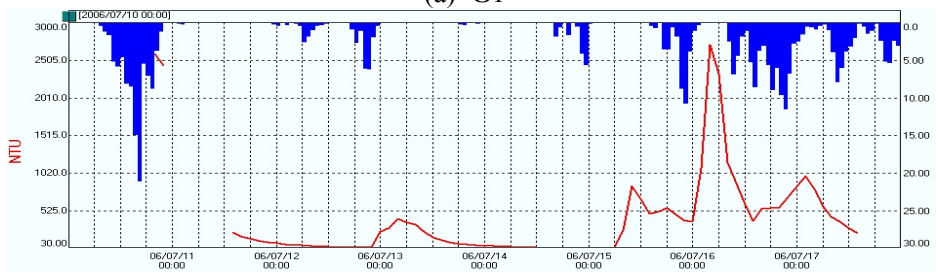

(b) G2

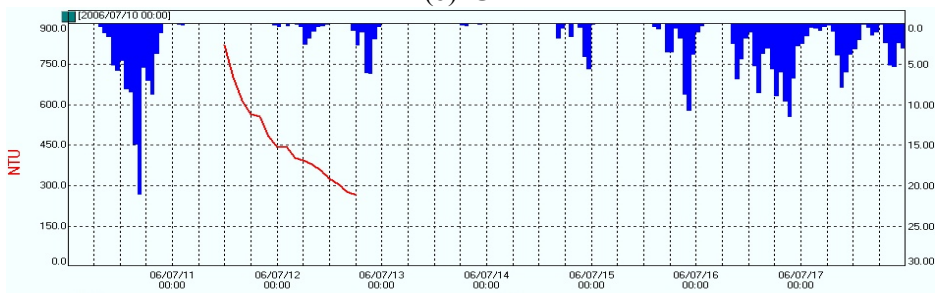

(c) G3

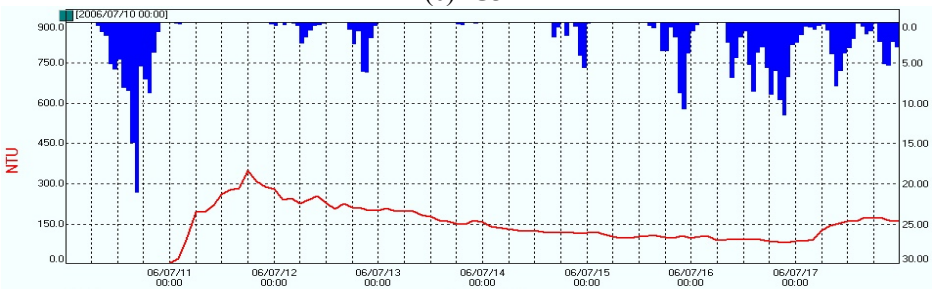

(d) G4

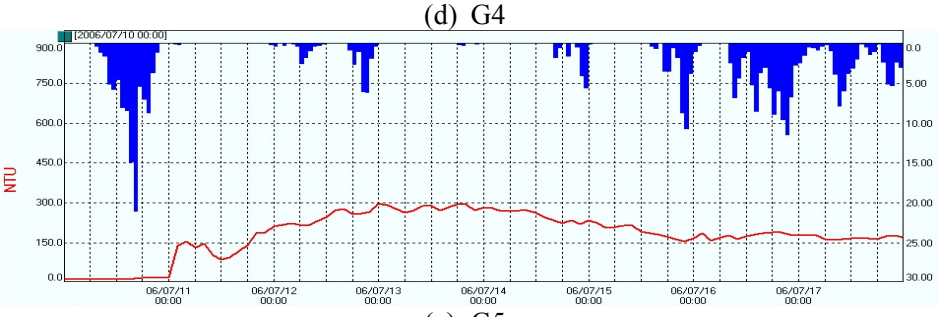

(e) G5

Figure 5.12 Temporal variations of inflow turbidity measured at gauging stations during Typhoon Ewiniar 2006. The y-axis represents depth-averaged values of turbidity.

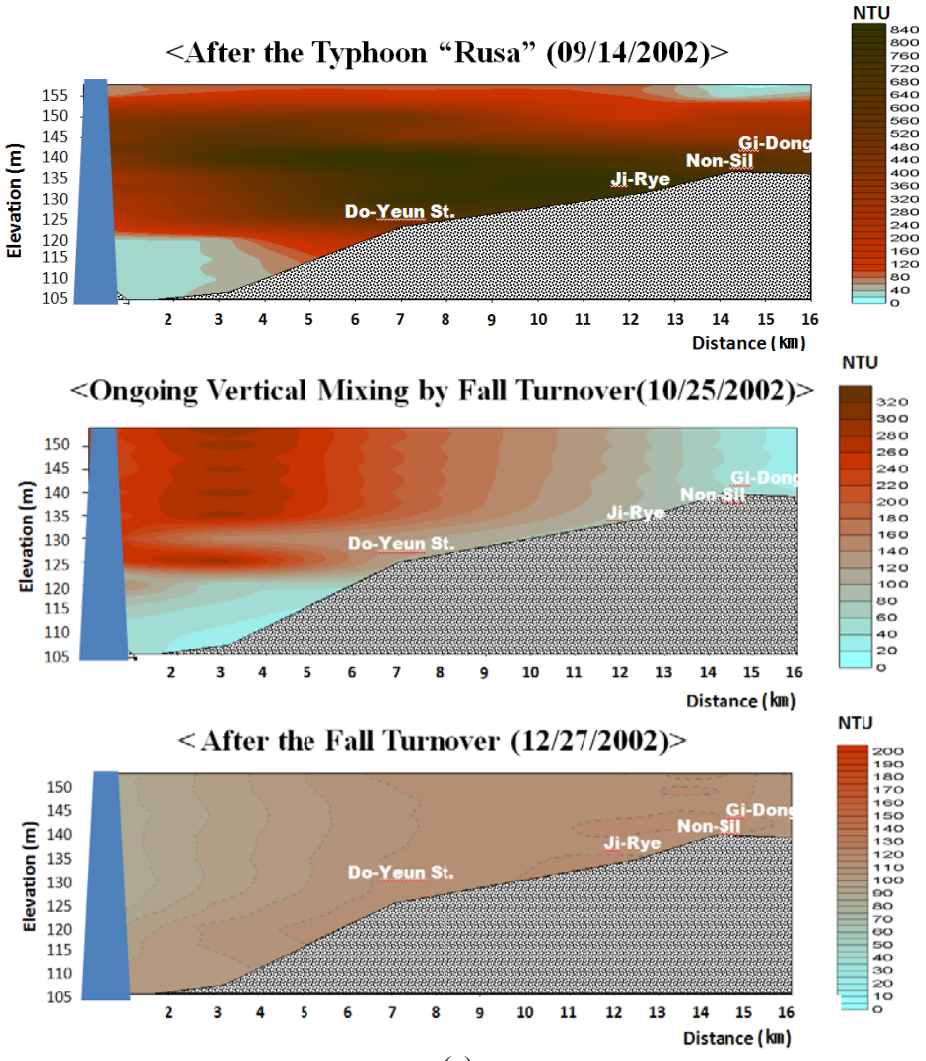

(a)

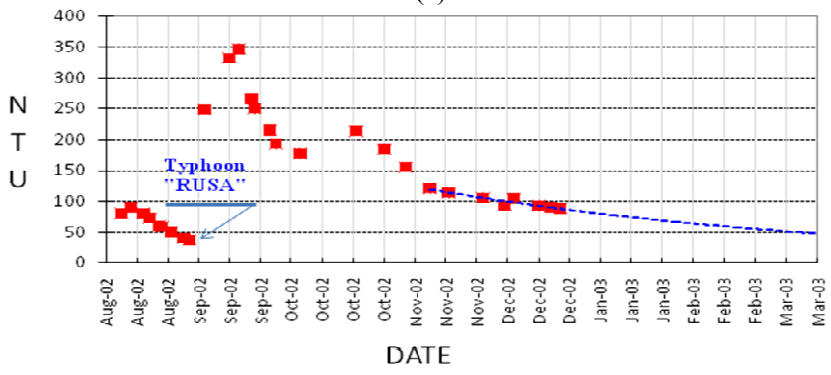

(b)

Figure 5.13 Intrusion of turbid density currents and discharge of the turbid water; (a) turbidity distribution after Typhoon Rusa (b) the turbidity measured from discharge water.

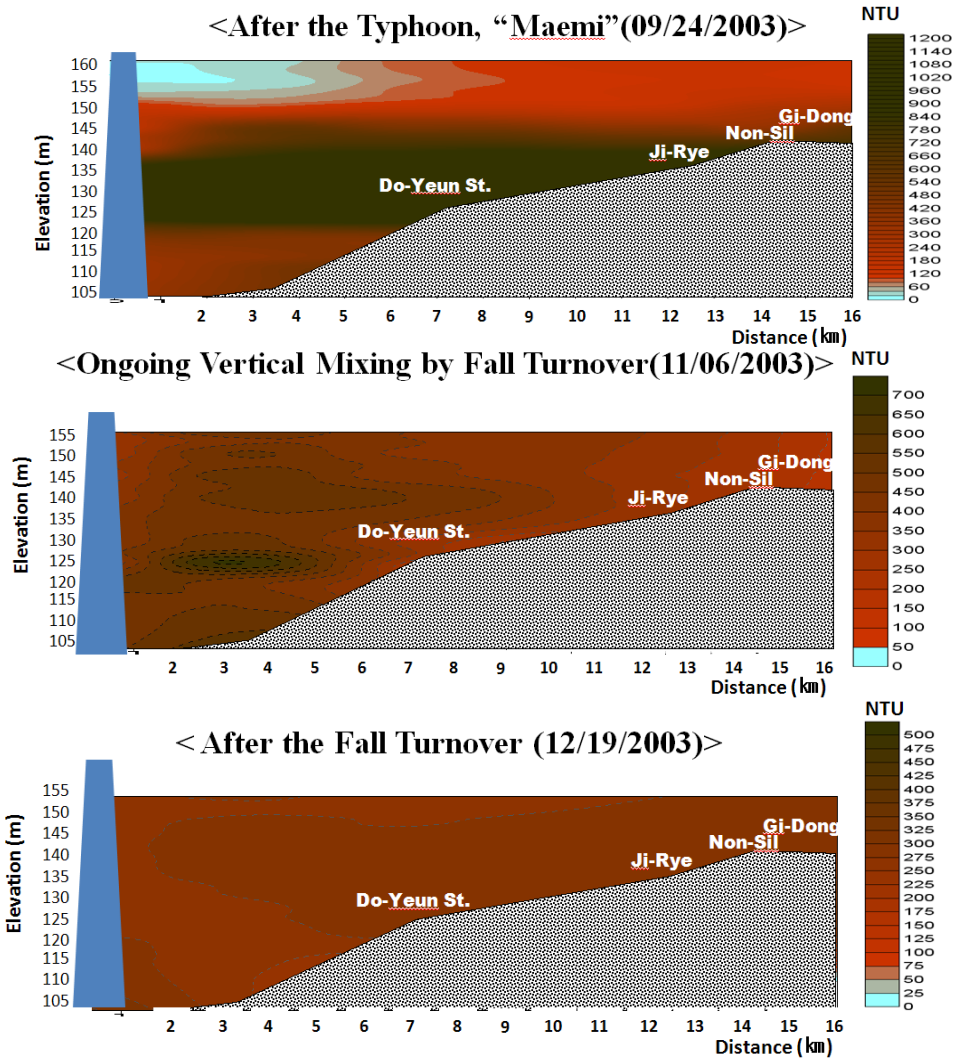

(a)

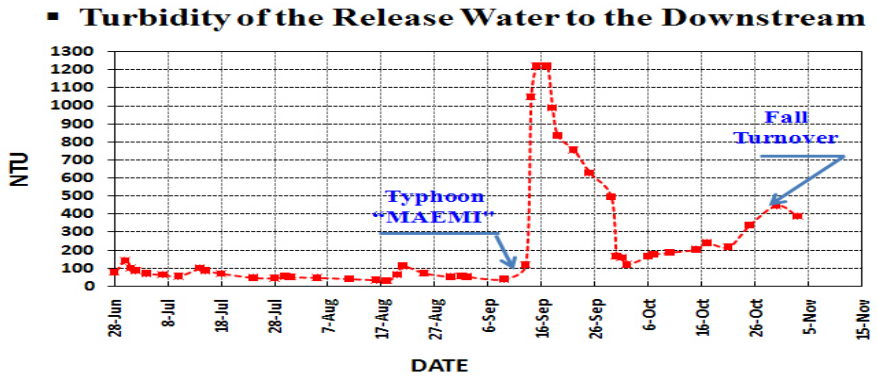

(b)

Figure 5.14 Intrusion of turbid density currents and discharge of the turbid water; (a) turbidity distribution after Typhoon Maemi (b) the turbidity measured from discharge water.

5.3.4 Relationship between Turbidity and Suspended Sediments

In order to model reservoir for the simulation of turbidity currents, we need the relationship between sediment concentration (mg/*l*) and turbidity (NTU), which is most easily measured in the field. K-water used 120 samples obtained on 21, 22, and 23 June and 23 July 2004 to determine the correlation. Figure 5.15 and Figure 5.16 show the relationship between sediment concentration (mg/*l*) and turbidity (NTU) measured in the reservoir and the tributary river, respectively.

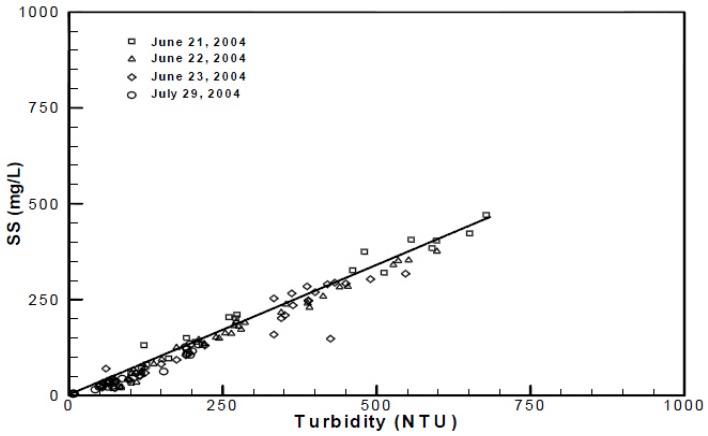

Figure 5.15 Relationship between sediment concentration and turbidity (NTU) measured in Imha Reservoir (SS=0.7 NTU).

The SS-NTU relationship must be used with caution, however, since the relationship probably might be similar among reservoir stations, but significantly different at different tributary stations. Turbidity measured in a tributary station is considerably affected by many factors (e.g., particle distribution, deposition rate, erosion rate, resuspension, total water depth, river structures, etc.). Therefore, it is very difficult to define a universal relationship between the two factors for representing each tributary. The relationship between SS and NTU obtained from field data will be used to specify boundary conditions for numerical simulations, but these values could be adequately adjusted for a calibration process.

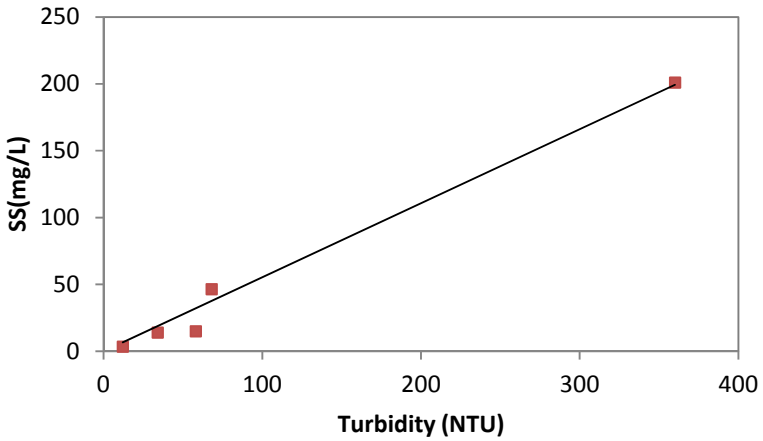

Figure 5.16 Relationship between sediment concentration and turbidity (NTU) measured at the tributary station (G1) (SS=0.5 NTU).

A series of experiments was conducted to analyze the particle distributions in the turbidity currents. The turbid water was sampled during some rainfall events in July 2007. The analysis results demonstrated that d_{50} ranged from 6 to 20 μm and the size of sediments increased with increasing turbidity (see Table 5.2). We theoretically estimate the settling velocity of particles in clear water and the settling time to travel 1.0 m depth in Table 5.3. This calculation describes that very fine particles found in all samples (d_{10} = 0.5 to 4.0 μm) do not settle easily under gravity.

Table 5.2 The relationship between turbidity and particle size distribution (K-water 2007).

Sampling Data (5 tests) Max. NTU	Particle size distribution (μm)		
	d_{10}	d_{50}	d_{90}
360	3.6	19.4	68.8
68	3.1	13.6	50.9
58	0.59	4.9	55.3
34	2.4	8.0	23.3
12	0.5	6.6	60.0

Table 5.3 Clear water fall velocity ω_s as a function of temperature and particle diameter (from Julien 1998). T_{1m} indicates the settling time to travel 1.0 m of water depth.

Particle Diameter d_s (μm)		Settling velocity ω_s (mm/s)			T_{1m}		
		0 °C	10 °C	20 °C	0 °C	10 °C	20 °C
Clay	1	4.8×10^{-4}	6.5×10^{-4}	8.6×10^{-4}	24 days	17.8 days	13.4 days
	2	1.9×10^{-3}	2.6×10^{-3}	3.4×10^{-3}	6.09 days	4.45 days	3.40 days
Silt	4	0.0076	0.01	0.014	1.52 days	1.15 days	19.84 hours
	8	0.031	0.042	0.055	8.96 hours	6.61 hours	5.05 hours
	16	0.12	0.167	0.22	2.31 hours	1.66 hours	1.26 hours
	32	0.49	0.67	0.88	34.01 min	24.87 min	18.93 min
Sand	64	1.9	2.66	3.47	8.77 min	6.26 min	4.80 min

K-water (2007) carried out settling column tests on the samples from major tributaries to Imha Reservoir. The settling column tests are compared with the samples from other streams. Figure 5.17 shows that Ban-byun Stream contains very fine sediments inducing turbid density intrusions in Imha Reservoir.

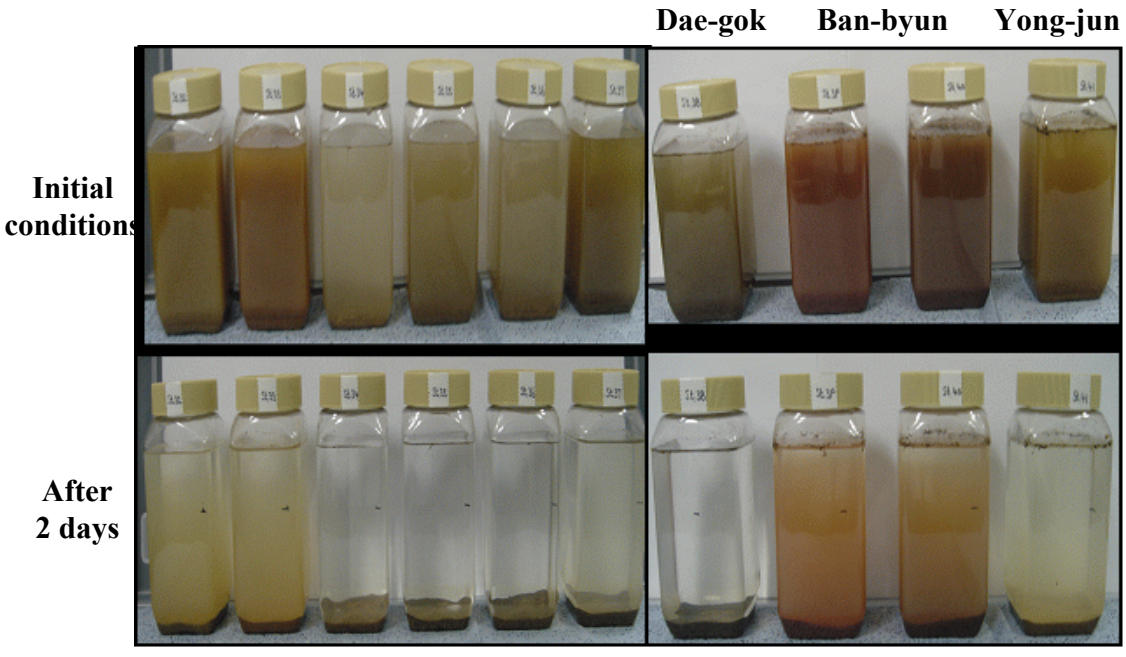

Figure 5.17 Settling column tests on (a) the samples from other streams (b) the samples from major tributaries to Imha Reservoir (from K-water 2007).

5.4 Conclusions

In this chapter, we presented a description of the study site and the field measurements. Real-time gauging stations installed at five locations provide the field data on turbidity, temperature, and water level at each 1.0 m depth interval. The data are transmitted in real-time at one or two hour intervals from the gauging stations to the Dam Integration Information System (DIIS) and used to set initial and boundary conditions for the numerical simulations, and to validate the numerical model.

During Typhoon Ewiniar in 2006, turbid density currents were recorded in Imha Reservoir. The field data show that the celerity of the currents varies in space and time according to the characteristic of three typical zones of the reservoir: riverine (G1 to G2), transitional (G2 to G3), and lacustrine zone (G3 to G5). The turbid density currents traveled a distance 18 km from the reservoir's inlet (G2) to the dam wall (G4) in 18 hours with average velocity observed as 0.23 m/s.

In Figure 5.12, we observed a large spatial gradient in the maximum depth-averaged turbidity between G1 and G3, but no significant change in the value between G1 and G2 (i.e., the riverine region). This implies the sediment particles were equally influenced by both the deposition and resuspension as they pass through the riverine region (G1~G2). However, after they enter into the reservoir, resuspension plays a negligible role in creating high turbidity due to the decrease of both inflow velocity and shear velocity resulting in reducing resuspension. Thus, the turbidity probably decreased due to particle settling and mixing while the turbid density currents passed through the transitional region (G2~G3). By contrast, the turbidity did not decrease any more after the turbid density currents passed G4. We observed spatially a uniform peak value of turbidity along the lacustrine region (G4~G5). This indicates that the sediment particles retained in the density currents were very fine particles (i.e., clay or very fine silt) that are difficult to settle. This hypothesis was supported by laboratory tests. The turbid water was sampled during some rainfall events in July 2007. The analysis results demonstrated that d_{50} ranged from 6 to 20 μm. In

particular, very fine particles were found in all samples (d_{10} = 0.5 to 4.0 μm), which do not settle easily under gravity. It is also well shown that autumn turnover can occur when very fine sediments still remain until the late autumn.

We investigated the response of the stratification structure to the wind forces during Typhoon Ewiniar using field measurements. We found that changes in the stratification structure were negligibly small, because the wind was blowing in the direction of the short fetch and not an enough condition to develop surface waves, accelerating vertical mixing. Thus, the effect of typhoon wind-driven forces can be negligible during the simulation periods.

Chapter 6[2]

Application of the Three-dimensional Model to Imha Reservoir

6.1 Introduction

In this chapter, we explore the evolution of turbid density currents changing from plunging flow and underflow to interflow in thermally stratified Imha Reservoir during Typhoon Ewiniar in 2006. Typhoon-induced turbid density currents typically show dramatic spatial and temporal variations when they enter into a reservoir through morphologically complex rivers. In order to simulate the complicated flows accurately, we employ the three-dimensional model, FLOW-3D with a non-hydrostatic approach. The model used here includes the particle dynamics algorithm that we developed to incorporate the effect of particle settling. Since, however, applying the 3-D non-hydrostatic CFD model to a large field-scale domain demands significant computational costs, the time-scale over which a reservoir can be simulated is limited by current computer technology in terms of both memory capacity and run time. In the case of typhoon-induced turbid density currents, they tend to propagate into a reservoir fast due to the large magnitude of inflows. Therefore, the model can provide successful simulations over the time-scale, which is enough to investigate the propagation dynamics of turbid density currents during severe flood events.

---

[2] This chapter will be submitted in substantial part as a paper entitled "Three- Dimensional Modeling of Turbid Density Currents in Imha Reservoir, South Korea", to the *Journal of Hydraulic Engineering*.

Field measurements during Typhoon Ewiniar are used to set initial and boundary conditions, and to compare to numerical results. Digital Terrain Model (DEM) and bathymetry survey data are used for three-dimensional geometry modeling. Applying the 3-D numerical model to the flow simulations influenced by complex geometry (e.g., turbid density currents passing narrow and deep meandering rivers) demands exact interface representation in the numerical model. In this study, exact representation of the complex geometry was accomplished using CAD (Computer Aided Design), GIS (Geographic Information System), and the FAVOR (Fractional Area-Volume Obstacle Representation method, used in exclusively in the FLOW-3D model) technique.

6.2 Model Preparation

6.2.1 Three-Dimensional Bathymetry Modeling

The bathymetric survey of Imha Reservoir taken by K-water (2007) provides topographic and bathymetric data for the production of a DEM (see Figure 6.1).

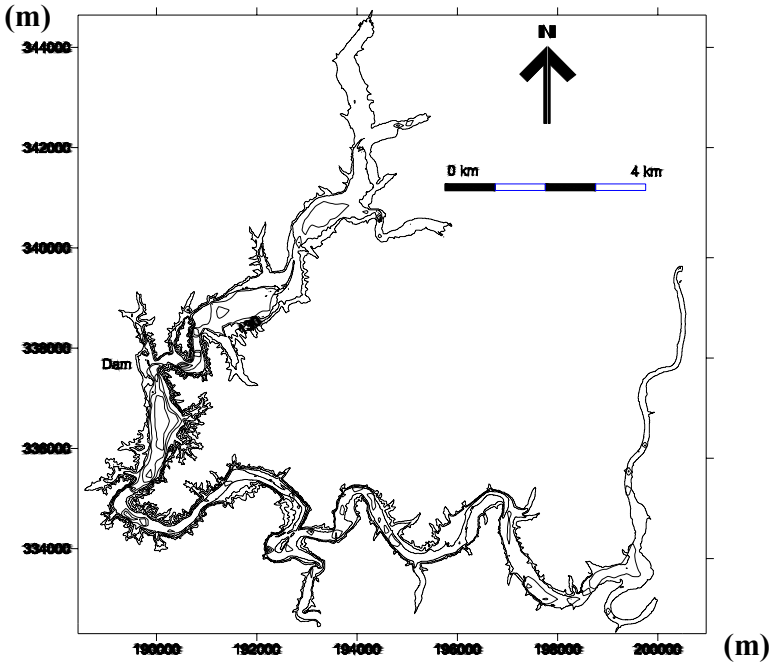

Figure 6.1 Imha Reservoir bathymetry developed using field survey data (2007) with l/5,000 digital map in a rectangular coordinate system.

The DEM was created using a GIS tool, which can incorporate the bathymetric survey data into topographic data (see Figure 6.2). The sophisticated methods for defining complex geometric regions (e.g., bathymetry, the surface terrain, and hydraulic structures) into the grid systems of the numerical model are needed to simulate the density currents passing the complex geometries. AutoCAD and Arcview GIS software were used to create the 3-D bathymetric model as a high-resolution stereolithography (STL) format, which can be exported to the FLOW-3D model (see Figure 6.3).

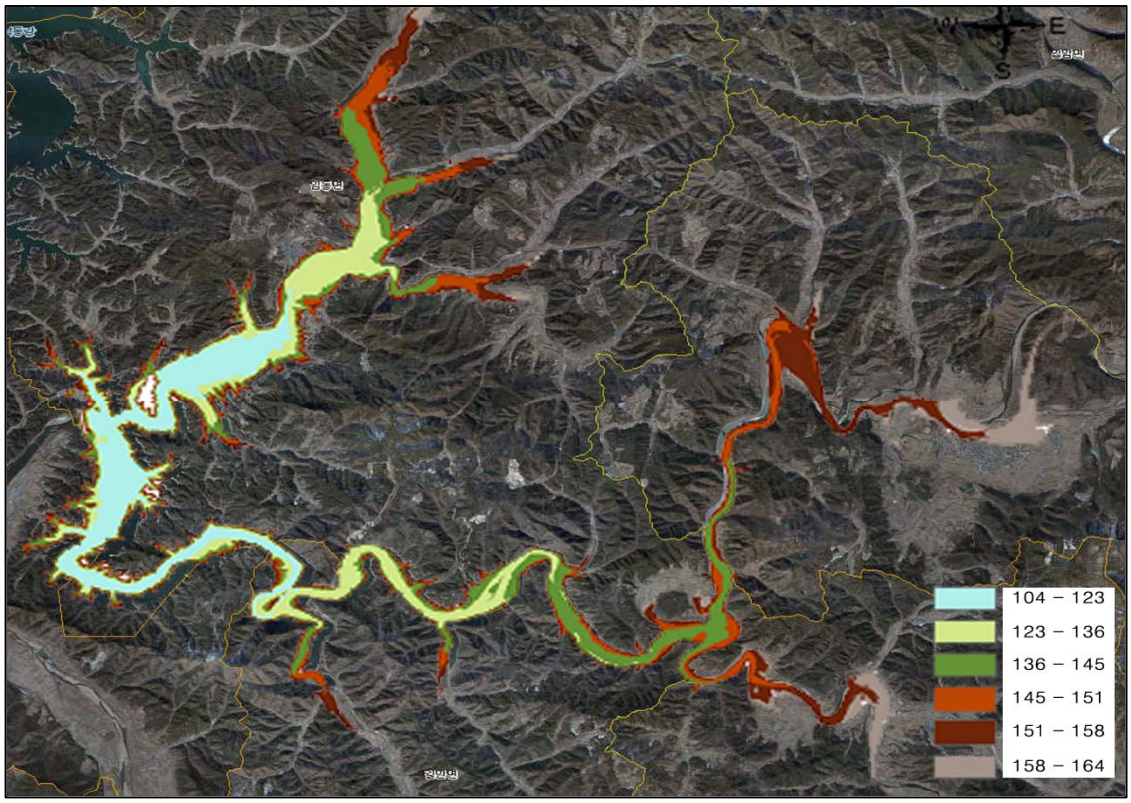

Figure 6.2 The bathymetric DEM model of Imha Reservoir. The colors illustrate increasing depth ranging from the deepest shown in cyan through different color shades to the shallowest shown in dark grey.

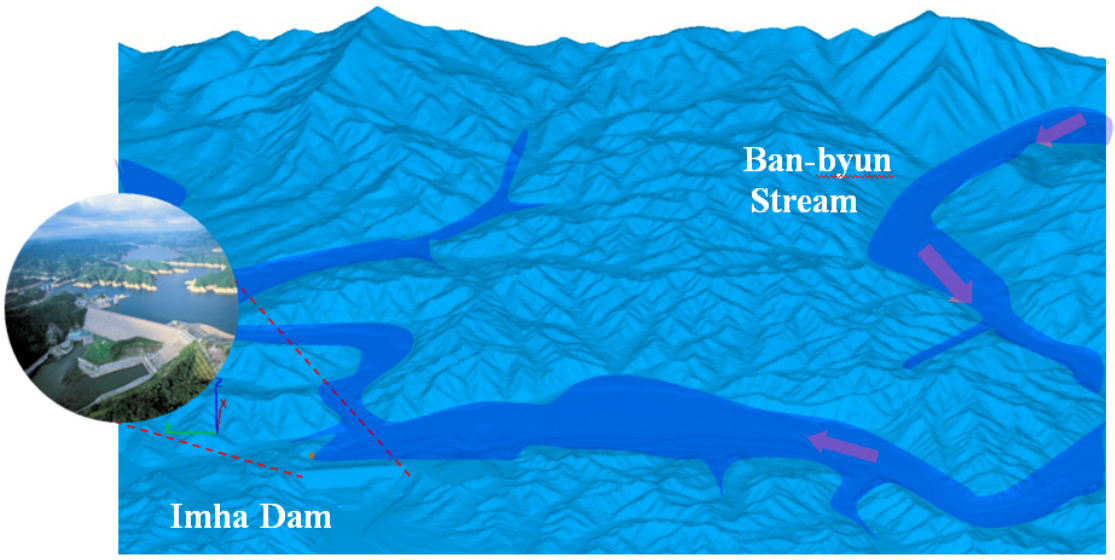

Figure 6.3 Three-dimensional bathymetric modeling as a high-resolution stereolithography (STL) format.

6.2.2 Computational Grid Generation

In order to solve the governing equations using the finite-volume approach, the simulation domain is required to be discretized on model grids. Since the dynamics of the density currents are affected by both complex geometric conditions of the study area and multi-physical properties (e.g., density stratification, particle settling, etc.), we employed relatively high-resolution discretization grids. The vertical layers below the water surface were represented by one meter depth ($\Delta z = 1.0$ m) throughout the reservoir water column, while horizontal grid sizes were chosen to be 25m ($\Delta x, \Delta y = 25$ m) due to the limitations of current computer resources in terms of both total run time and memory capacity. The computational meshes were generated with 2.5 million cells (see Figure 6.4).

The FLOW-3D model uses the FAVOR method to get better geometric representations of complex geometries in the grid system, based on rectangular cell mesh. In the FAVOR method, complex geometries are defined within each cell by calculating the ratio of fractional volumes

occupied by obstacles and fractional volumes filled with fluid or air. This is a very good method for representing complicated geometric shapes with the rectangular grid system.

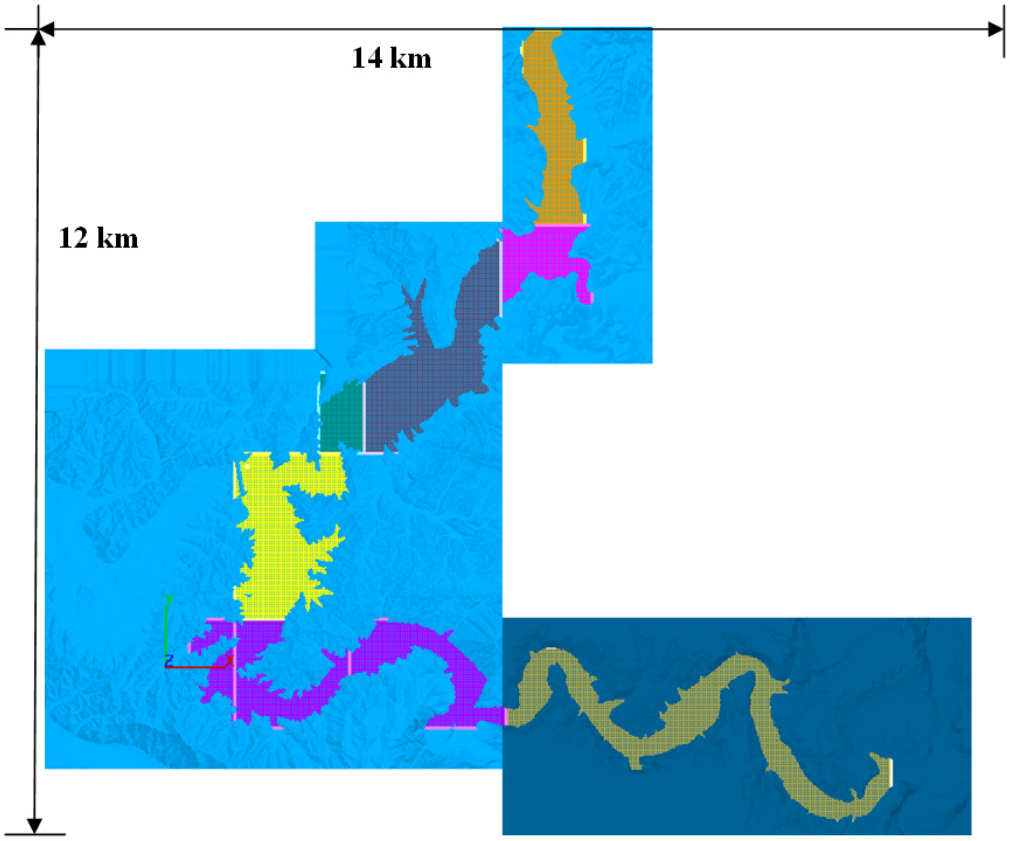

Figure 6.4 Grid generation for the simulations of Imha Reservoir.

6.2.3 Boundary and Initial Conditions

Boundary conditions for the simulations include spatially and temporally varying river inflows and outflows, river inflow temperatures and concentration of suspended sediments, wind directions and speeds. Temperature and turbidity profiles measured at Buoy-point (near the dam wall, G4) were used to set initial conditions. The depth-averaged turbidity data with time, collected at Do-yeun gauging station (G3), Buoy-point (near the dam wall, G4), and Su-gok gauging station (G5), were used for field validation.

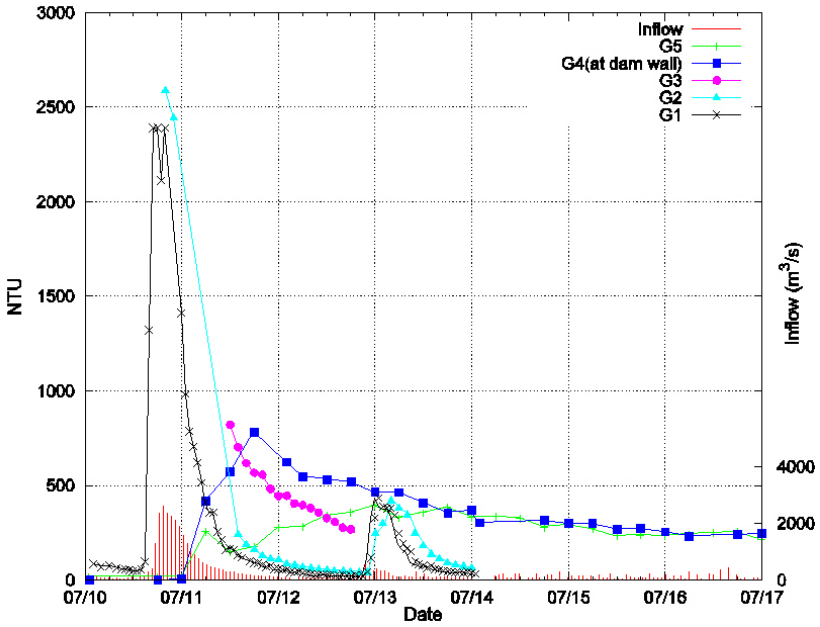

Figure 6.5 Field measurements for setting boundary conditions. The time series plots of the turbidity were made using peak values in the turbidity profiles measured at each site during Typhoon Ewiniar.

Some subroutines of the original code (FLOW-3D) were modified to allow for defining the density of each cell as a function of temperature and sediment concentration. Thus, each layer in water columns throughout the reservoir can have a different density by initial condition and boundary conditions. The total inflows to the reservoir were calculated by using the hourly reservoir water level measured at the dam site and the volume of the reservoir, which is determined as a function of the water level, while the other data were directly collected from each monitoring station.

An inflow boundary location was specified at the confluence of two main tributaries (e.g., Ban-byun Stream and Yong-jun Stream). The inflow from Dae-gok Stream, the sub-basin which is of the smallest drainage area, was neglected. The monitoring gauging station is located near the confluence; the real-time measurements (temperature, NTU) were used as boundary input to the numerical model.

Wind-driven shear stress at the water surface of a reservoir is regarded as one of the important external energy sources with respect to current circulation and mixing processes. The shear stress (τ) is given by

$$\tau = C_D \rho_A U_w^2 \tag{6.1}$$

where U_w = the wind speed at 10 m above the water surface; ρ_A = air density; and C_D = the surface drag coefficient. Even though a great deal of research effort was conducted to determine the value of C_D for different reservoir conditions, large spatial and temporal variability in the value of C_D was observed through field measurements. It is strongly influenced by the stability of a water body, wind speed, and reservoir depth. Therefore, from a practical view point, an average value of $C_D = 0.0013$ is suggested for most engineering approaches (Fischer *et al.* 1979).

In addition to the variability, it is not easy to measure the wind speed at 10 m above the water surface since the necessary data are generally provided from the land-based meteorological stations, located far away from the reservoirs. The wind shear stress is applied in the control volumes containing the free surface (i.e., the top cell of water columns). The wind shear stress adds new terms in the right-hand side of the x and y directional velocity equations, respectively. The wind-driven velocity components at the wind-mixed layer are calculated by the following relationships

$$\frac{du_x}{dt} = ... + \frac{C_D \rho_A U_{wx}^2}{\rho_w h} \tag{6.2}$$

$$\frac{du_y}{dt} = ... + \frac{C_D \rho_A U_{wy}^2}{\rho_w h} \tag{6.3}$$

where U_{wx}, U_{wy} = the wind velocities in the x and y directions; ρ_A = water density; and h = the depth of the wind-mixed layer. The relative velocity between water and winds is not considered for the above equations since the wind speed is generally much larger than that of the water.

No-slip conditions, modeled by assuming a zero tangential velocity on the boundary, were specified along interfacial areas between solid geometries and flows (e.g., reservoir bottoms and

side walls). The modeling for the turbulence near the solid boundary is conducted by using a so-called "wall function", assuming that a shear stress at the wall can be computed using a logarithmic velocity profile. The logarithmic velocity profile is the following:

For a smooth wall the equation is,

$$u = u_* \left[\frac{1}{\kappa} \ln\left(\frac{\rho u_* z_o}{\mu} \right) + 5.0 \right] \tag{6.4}$$

where k = the von Karman constant; u = the velocity parallel to the wall orientation at the distance from the wall(z_o); and u_* is the shear velocity. In a turbulence transport model (e.g., standard $k-\varepsilon$ or RNG $k-\varepsilon$), the turbulent variables, k and ε, are defined by the value of u_* as the following:

$$k = \frac{u_*^2}{\sqrt{c_\mu}}, \qquad \varepsilon = \frac{u_*^3}{\kappa z_o} \tag{6.5}$$

where c_μ = a turbulence parameter (c_μ =0.085 in the RNG model).

For rough walls,

$$u = u_* \left[\frac{1}{\kappa} \ln\left(\frac{z_o}{k_s} \right) + 8.5 \right] \tag{6.6}$$

where k_s is the roughness height of particles.

6.2.4 Model Parameters for Calibration

We employed the 3-dimensional hydrodynamic model coupled with a particle dynamics algorithm to simulate the turbid density currents in the stratified reservoir. A multi-dimensional approach is required for the simulations of complex flows, resulting from the complicated reservoir morphometry and the interactions between the inflowing currents and various mixing processes. Although the multi-dimensional hydrodynamics model needs less parameterizations than other

reduced dimensional models (i.e., 1-D or 2-D), there are still some important parameters to be considered for this turbid density currents modeling.

In order to simulate the turbid density currents, the conversion between the suspended sediments (mg/*l*) and turbidity (NTU) is required. The SS-NTU relationship determined by using field data at G2 and G4 (see Figure 5.15 and Figure 5.16 in Chapter 5) and was adequately adjusted through calibration. Application of the numerical model with SS/NTU = 1.0 at G4 and SS/NTU = 0.4 provided a good agreement with field measurements. Settling velocity of sediment particles is modeled as a function of the diameter and the density of the particle according to Stokes' Law.

In parameters of the RNG k- ε turbulence model, we used the values of turbulence coefficients presented by Yakhot and Orszag (1986) (i.e., $c_\mu = 0.09$; $c_{1\varepsilon} = 1.42$; $c_{2\varepsilon} = 1.83$; $c_{3\varepsilon} = 0.2$; $\sigma_k = 1.39$; $\sigma_\varepsilon = 1.39$; $\eta_o = 4.38$; and $\beta = 0.015$). The turbulent Schmidt number was set to be 5, which was presented for gravity currents modeling in Chapter 4. In FLOW-3D code, time steps are automatically controlled by the stability criteria, Equation (3.20), to insure time-accurate approximations between minimum time step $\Delta t = 1 \times 10^{-6}$ sec and maximum time step $\Delta t = 1.5$ sec.

6.3 Simulation Results

6.3.1 Modeling Wind-Driven Currents

In this simulation, we investigated the effect of wind-driven mixing on thermal structures of the reservoir during the typhoon. Figure 6.6 shows the velocity field of near the surface for the maximum wind condition induced by the typhoon. The flows were initiated by the wind shear stress in the equal direction to wind direction (ESE, 112.5^o). They showed the fastest velocities when they passed through the narrow area in front of the reservoir. In order to investigate the change of the stratification under the severe wind conditions, we plotted the temperature distributions in the Y-Z plane at three different positions as shown in Figure 6.6(c). The tilted

interfacial layers between the epilimnion and the thermocline were observed at each position, but they did not contribute significant change in the structure of stratification. These results indicate that the effect of the wind can be negligible when compared to the strong effects of the river inflows during the flood event.

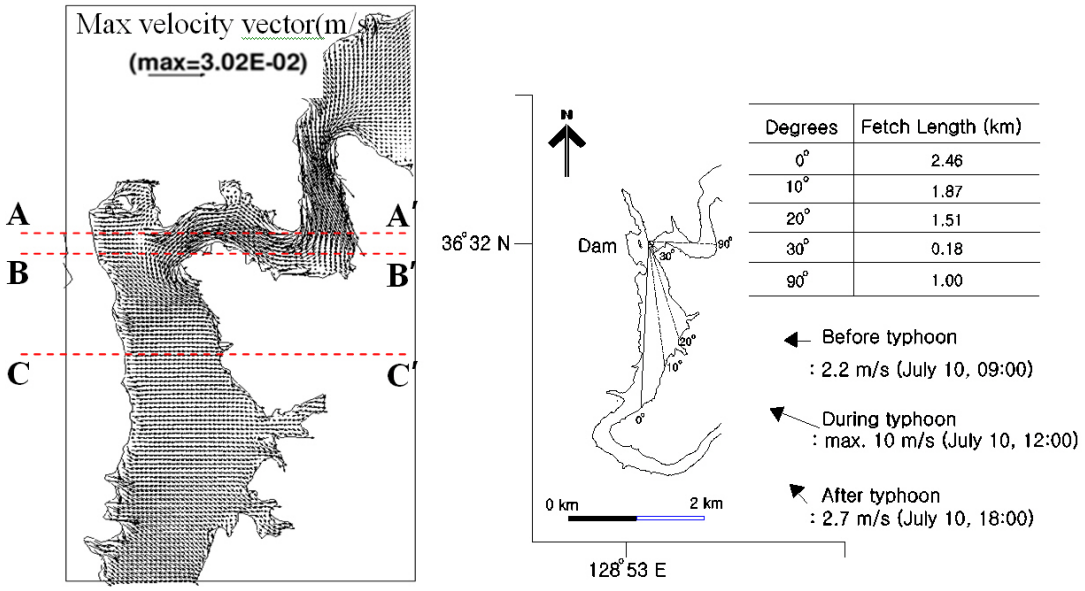

(a)Wind-driven horizontal circulation during the typhoon (b) Wind fetch, direction, and magnitude

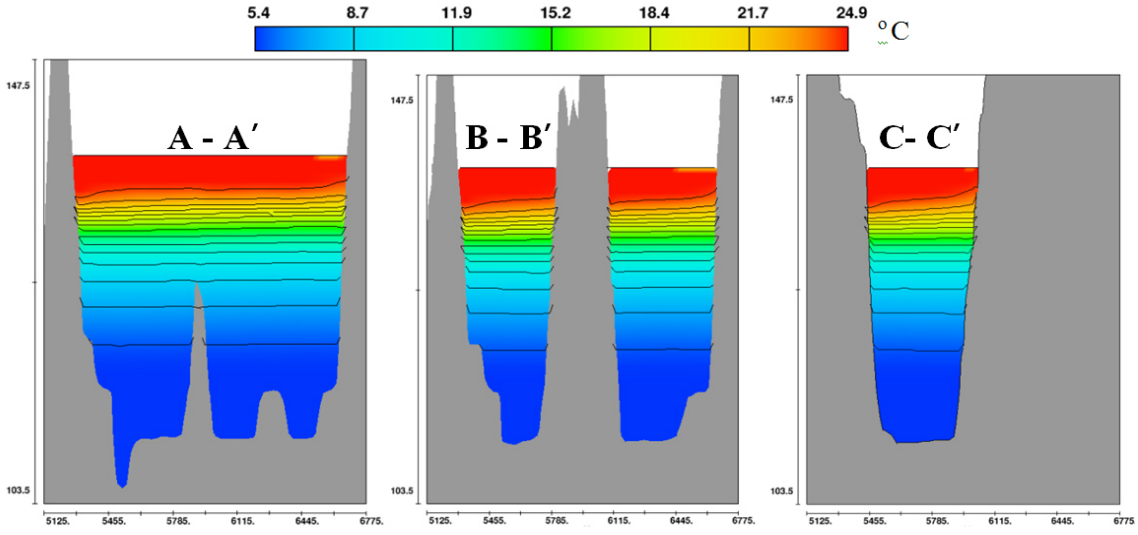

(c) Wind-driven changes of the thermal stratification during the typhoon. Scale H:V=1:20

Figure 6.6 The effect of wind on thermal stratification during the typhoon.

6.3.2 Modeling Flood-Driven Currents

During Typhoon Ewiniar in 2006, the total amount of the inflows entering the reservoir roughly reached 100×10^6 m^3, which was equal to 25 % of the effective capacity of the reservoir (424×10^6 m^3). Because of the large magnitude of inflows with relatively short duration (35 hours) during the typhoon, we can obviously expect that they control the reservoir's dynamics with thermal stratification. Thus, mixing of the inflows is a dominant factor to account for the dynamics of the turbid density currents in this study.

The numerical simulations were performed on two personal computers with the hardware platforms: 3.2 GHz Quad-Core (i7), 4GB memory. Overall movements of the turbid density currents entering into the reservoir during the flood event were reproduced accurately through three -dimensional simulations. The three-dimensional simulations of density currents, however, are computationally very expensive. Thus, we employed the shared-memory parallel version of FLOW-3D code, available on a multi-core computer, allowing for efficient parallelism. We performed numerical simulations during 3 days (7/10/2006 to 7/13/2006) and it took a week to complete one simulation case.

The inflows showed fast propagation speeds in the transitional region (G2~G3) due to the bed slope and narrow cross section, while the inflows reduced their propagation speed because they intruded horizontally into the lacustrine region (G3~G5), which was a width is greater than that of the other regions (i.e., riverine or transitional region). In Figure 6.13, time-series plots are used to illustrate the temporal variations of suspended sediments at three locations (G3, G4, and G5). Figure 6.13 indicates the travel time of peak turbidity from G3 to G4 and from G4 to G5 was about 15 hours and 30 hours, respectively, during the flood event. Figure 6.7 and Figure 6.8 show simulation results with horizontal viewpoint at EL 141.0 m (10 m above thermocline). Figure 6.9 presents the simulated temporal and spatial distributions of turbidity with horizontal viewpoint at EL 131.0 m (thermocline). Figure 6.10 shows simulation results with horizontal viewpoint at EL

121.0 m (10 m below thermocline) and illustrates temporal and spatial evolutions with the longitudinal dispersion and lateral mixing in the meander loops very well.

Appendix A.3 derives an analytical solution to estimate the intrusive speed of turbid density currents propagating into a reservoir. The equations consist of the continuity equation and an empirical formula. The solution of these equations presents the intrusive depth and celerity of gravity currents entering into a reservoir, given by

$$h_d = \left[\frac{L^2}{g'} \left(\frac{\Delta h}{\Delta t} \right)^2 \frac{1}{C^2} \right]^{1/3} \tag{6.7}$$

$$U_d = C\sqrt{g' h_d} \tag{6.8}$$

where h_d is the depth of density currents and L is the length of a reservoir. $\Delta h / \Delta t$ indicates the rate of change of reservoir surface elevation during a flood event. C is a coefficient ($C \approx 0.7 - 1.0$). Table 6.1 shows that the analytical solution provides a good prediction of the celerity of intrusive turbid density currents in Imha Reservoir.

Table 6.1 Average celerity of turbid density currents traveling from G2 to G4 (18 km), computed using the analytical solution (see Appendix A.3 for the derivation).

	Distance	C	Average celerity	Intrusion depth at G4
Field measurement	18 km (G2 to G4)	-	0.23 m/s	10~15 m
Analytical solution	30 km (Reservoir length)	from Figure A.5 $C = 0.8$	0.31 m/s	11.6 m
		Benjamin (1968) $C = 0.7$	0.28 m/s	12.7 m
		Kao (1977) $C = 1.0$	0.19 m/s	18.6 m

We estimate the location of the plunge point using the analytical solution (Equation 2.16 in Chapter 2), which was derived for the steady-state flow in a constant width channel. At the inlet point of the reservoir (G2), the maximum inflow densimetric Froude number F_o (defined as Equation 2.11) was 4.6 during the flood event, indicating an inertial force is dominant rather than

the buoyant forces (when $F_o > 0$). According to the analytical, solution turbid density currents plunge between G3 and G4 at an approximate water depth 25 m (6 km from G4) during the flood event (using a constant peak inflow 2650 m^3/s). In numerical simulations, however, the plunge depth varies depending on time and space due to the significant changes in width and inflows of the reservoirs during the flood event.

Keulegan (1949) proposed an interfacial stability number ϑ to determine the flow conditions at which mixing occurs. He defined ϑ from viscous and gravity forces as Equation (2.28). The occurrence of mixing across the interface depends on the critical Keulegan number ϑ_c. The average experimental value of ϑ_c for turbulent flow was estimated to be ϑ_c=0.18 for turbulent flow. The flow will be stable (i.e., mixing is small), if $\vartheta > \vartheta_c$. On the contrary, when $\vartheta < \vartheta_c$, the interfacial mixing happens. In Table 6.2, the field measurements indicate the depth and intrusive celerity of density currents between measurement points. We approximately estimate the rate of sediment transport by the turbid density current during Typhoon Ewiniar. If the average width and C_v of the density currents are assumed to be W_d = 500 m and C_v = 0.0002 or C = 500 mg / l, the discharge of the density currents is $Q_d = U_d\, h_d\, W_d$ =1150 m^3/s and that of sediment $Q_{sd} = Q_d\, C_v$ =0.23 m^3/s , which is approximately identical to a sediment transport rate of 50,000 tons/day. This sediment transport rate of 50,000 tons/day estimated during Ewiniar is nearly equal to 45,300 tons/day during Typhoon Maemi in 2003, presented by Lee and Cho (2004).

Table 6.2 Application of Keulegan number ϑ_c to the turbid density currents observed in Imha Reservoir during Typhoon Ewiniar.

Distance	Average intrusive celerity (m/s)	Current depth (m)	ϑ		
G2 to G4	0.23	10 m	0.01	Mixing occur	$\vartheta < \vartheta_c$
G4 to G5	0.04	15 m	0.07	Mixing occur	$\vartheta < \vartheta_c$

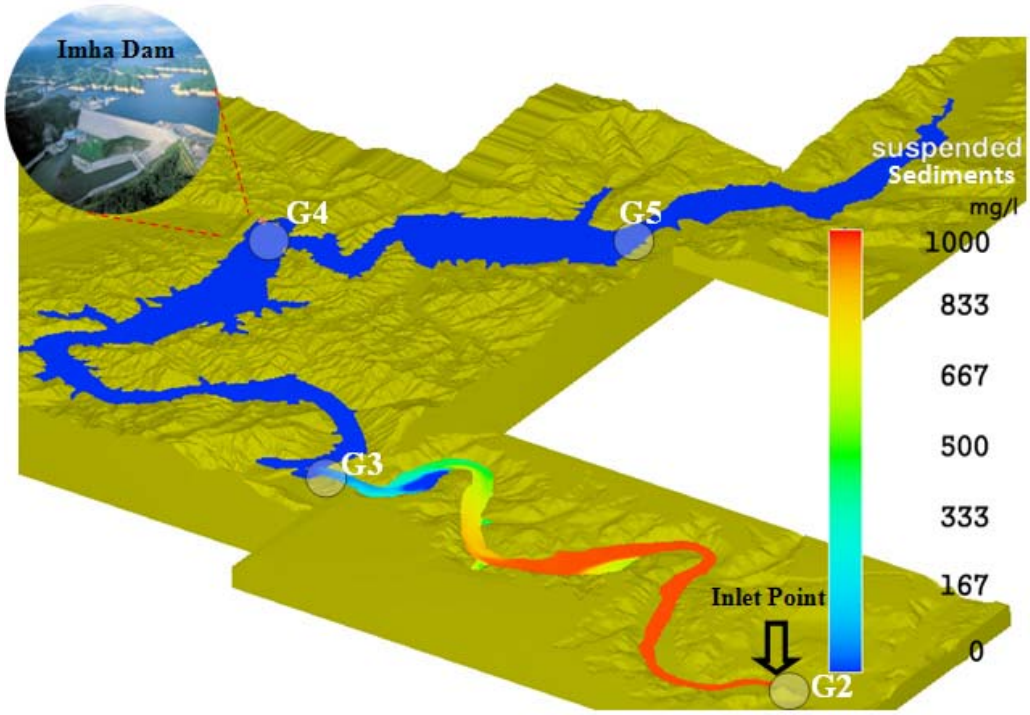

(a) July 10, 18:00

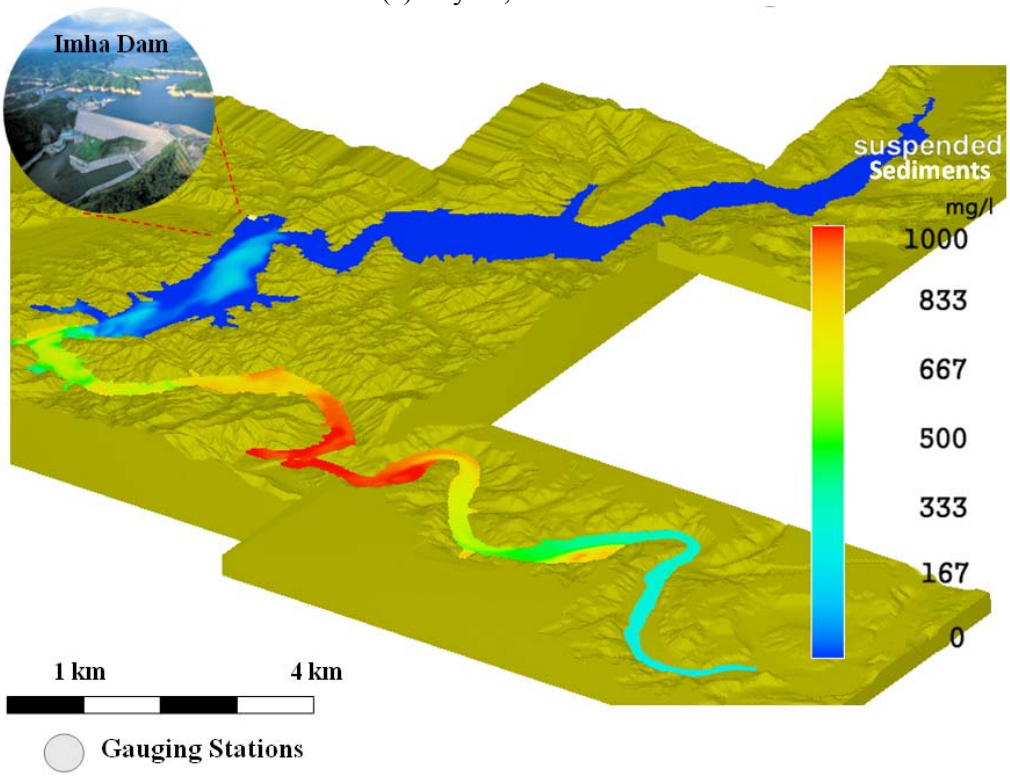

(b) July 11, 04:00

Figure 6.7 Simulated temporal and spatial distributions of suspended sediment concentration with 3-D viewpoint at EL 141.0 m (10 m above thermocline), continued.

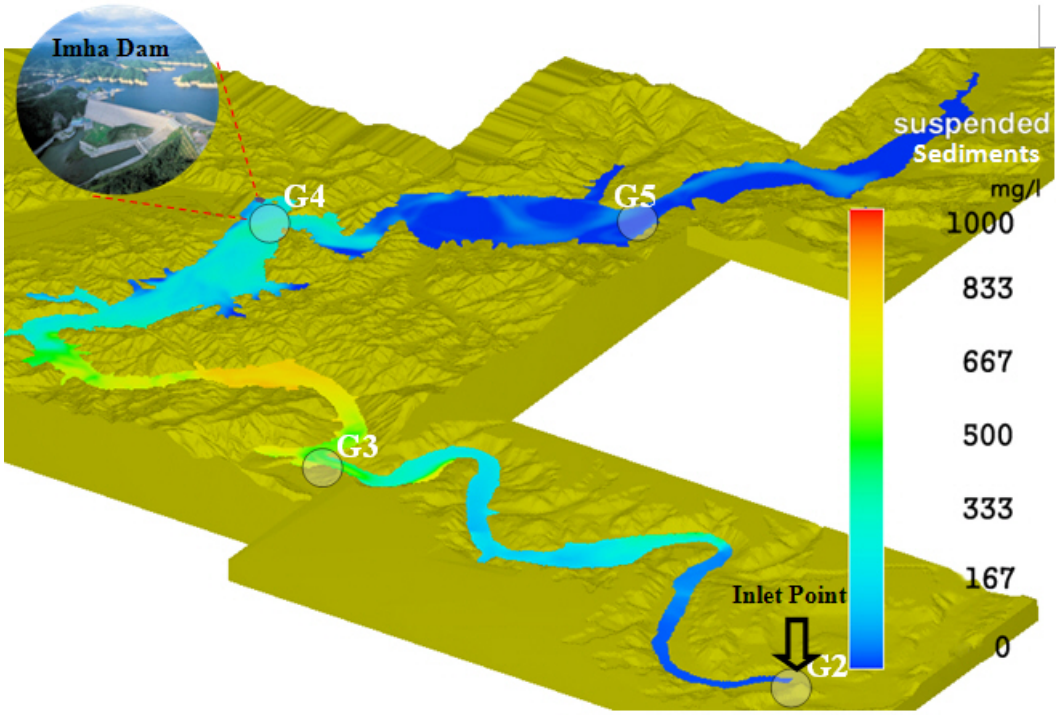

(c) July 12, 00:00

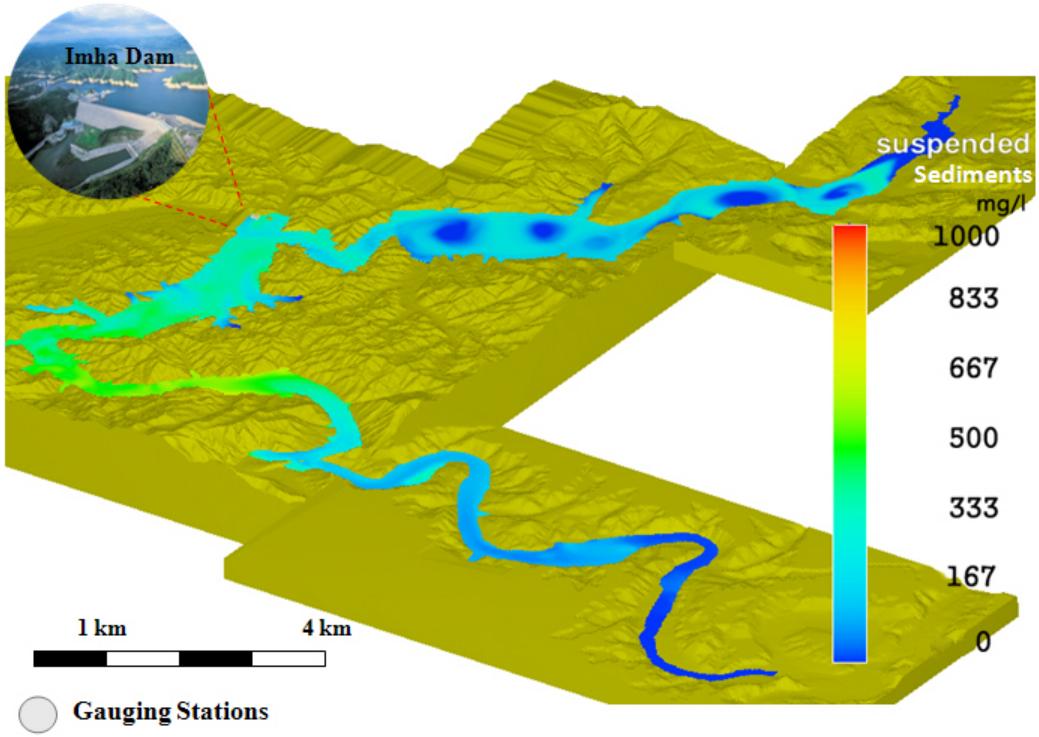

(d) July 12, 16:00

Figure 6.7 Simulated temporal and spatial distributions of suspended sediment concentration with 3-D viewpoint at EL 141.0 m (10 m above thermocline).

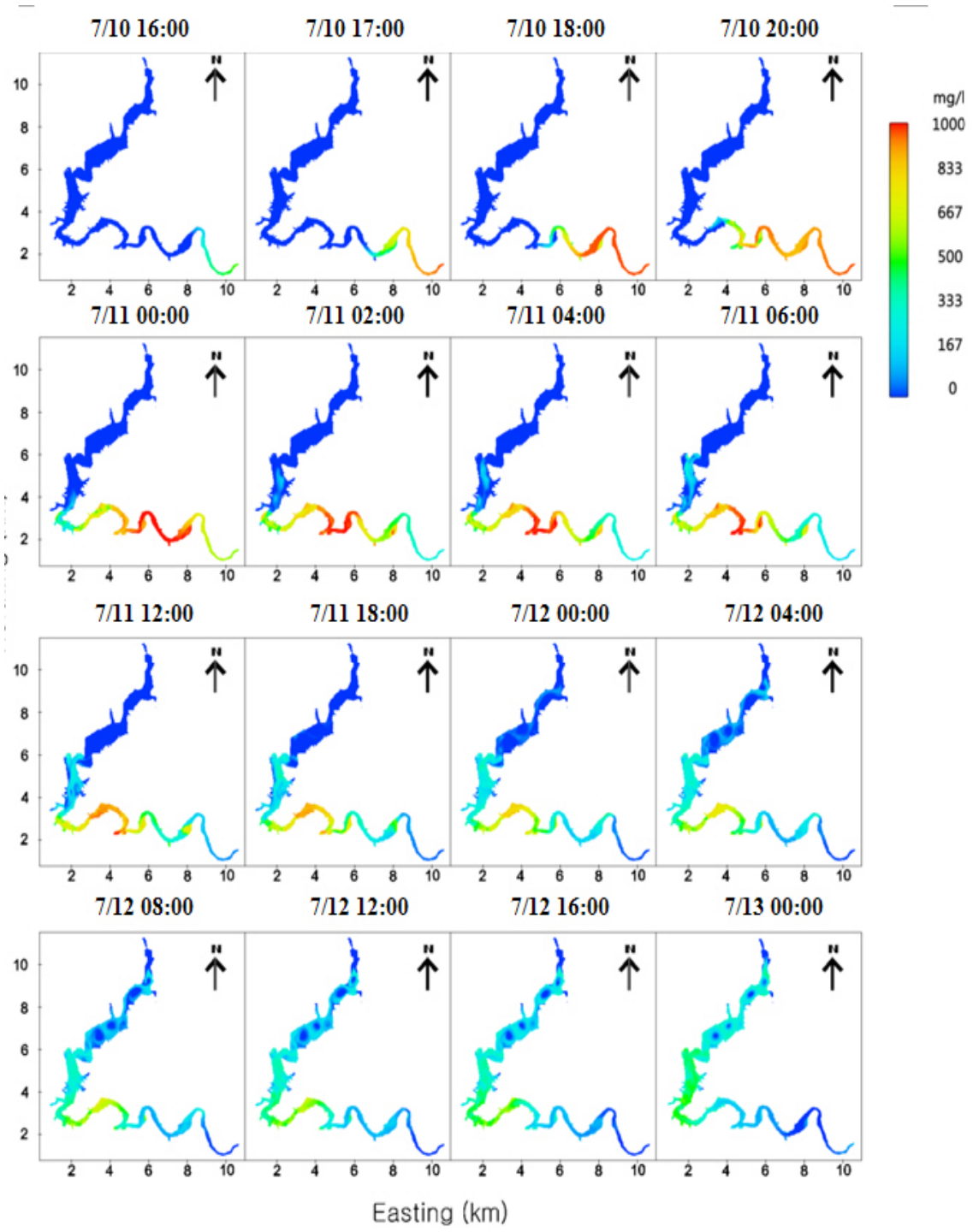

Figure 6.8 Simulated temporal and spatial distributions of suspended sediment concentration with horizontal viewpoint at EL 141.0 m (10 m above thermocline).

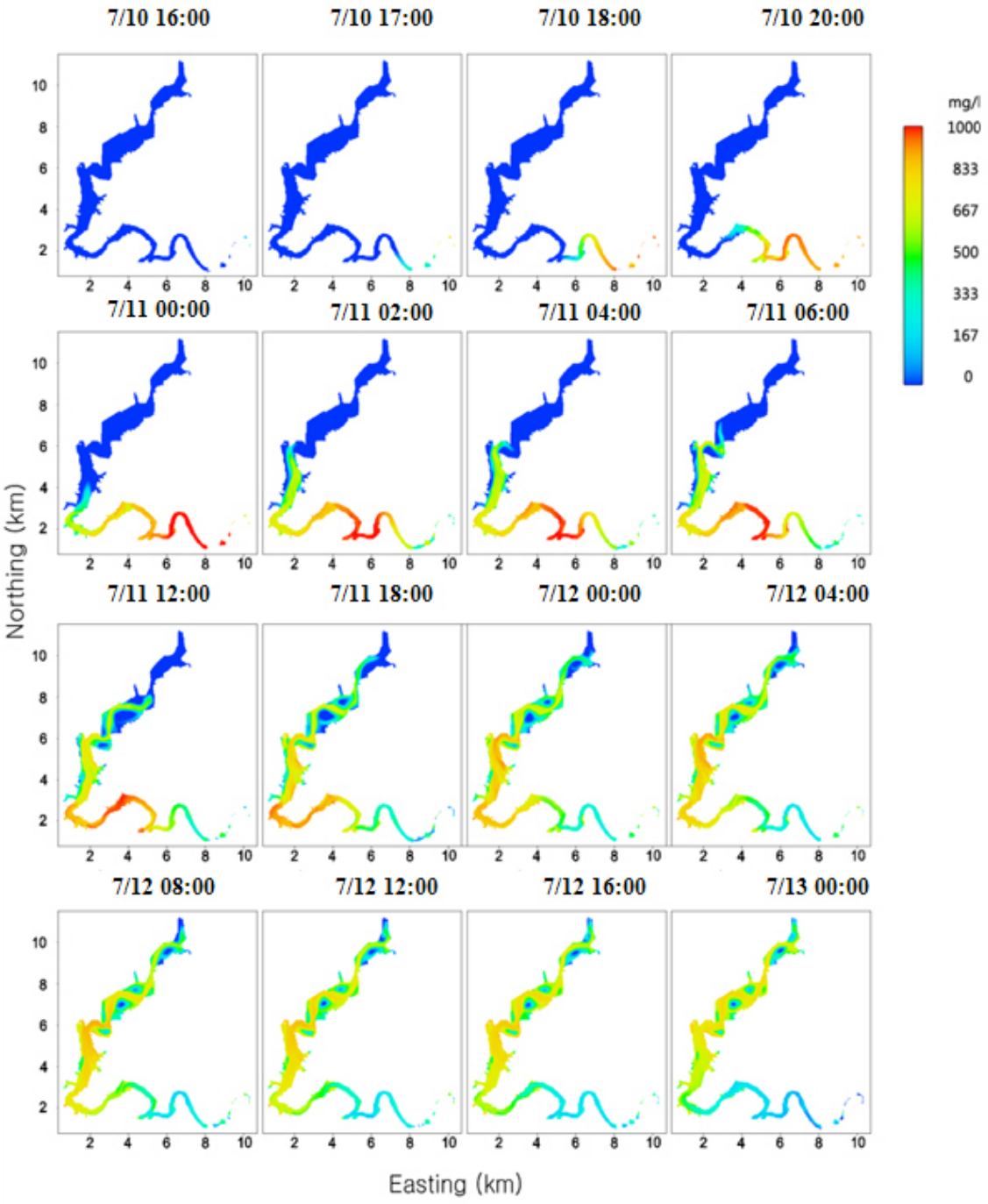

Figure 6.9 Simulated temporal and spatial distributions of suspended sediment concentration with horizontal viewpoint at EL 131.0 m (thermocline).

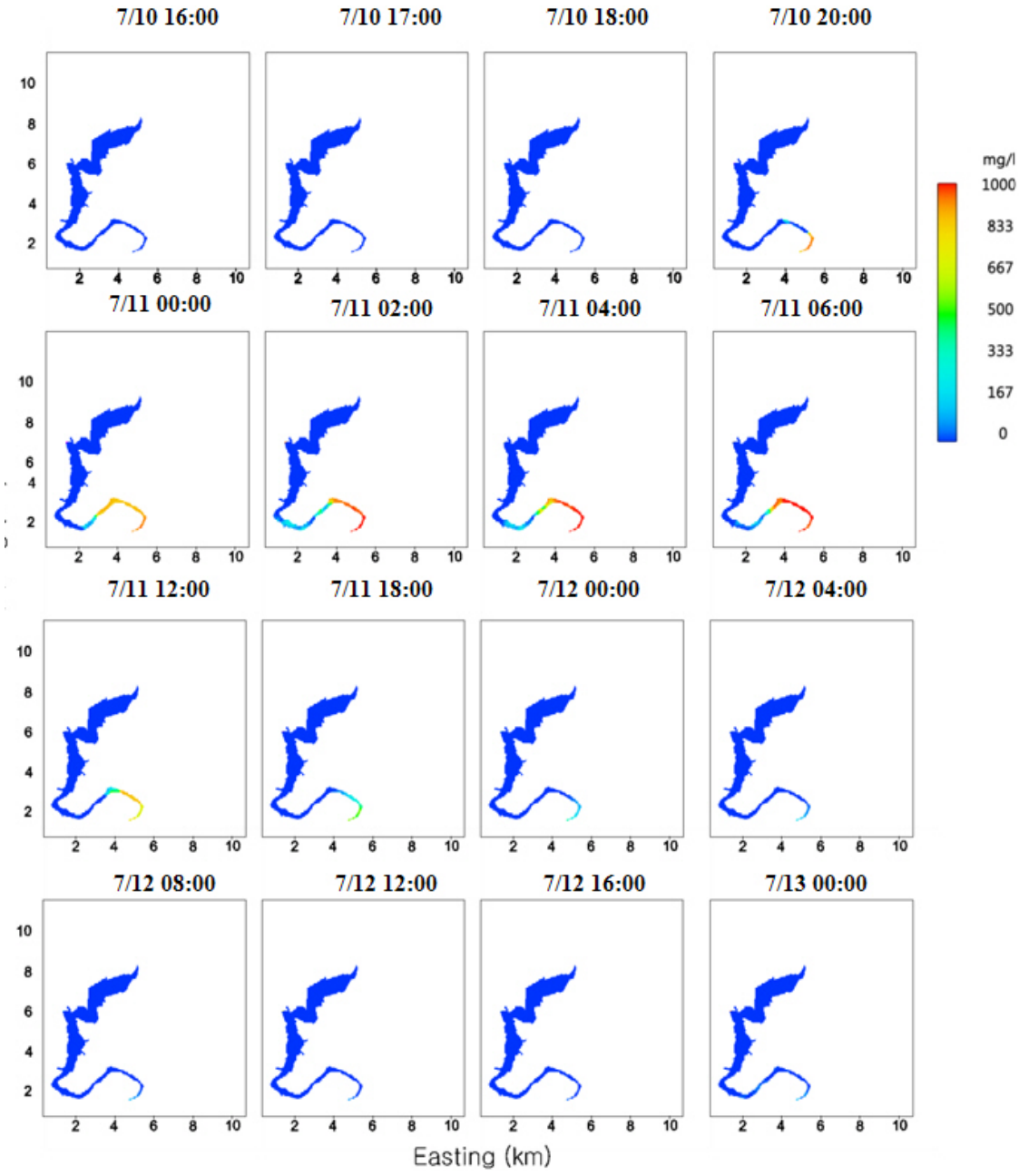

Figure 6.10 Simulated temporal and spatial distributions of suspended sediment concentration with horizontal viewpoint at EL 121.0 m (10m below thermocline).

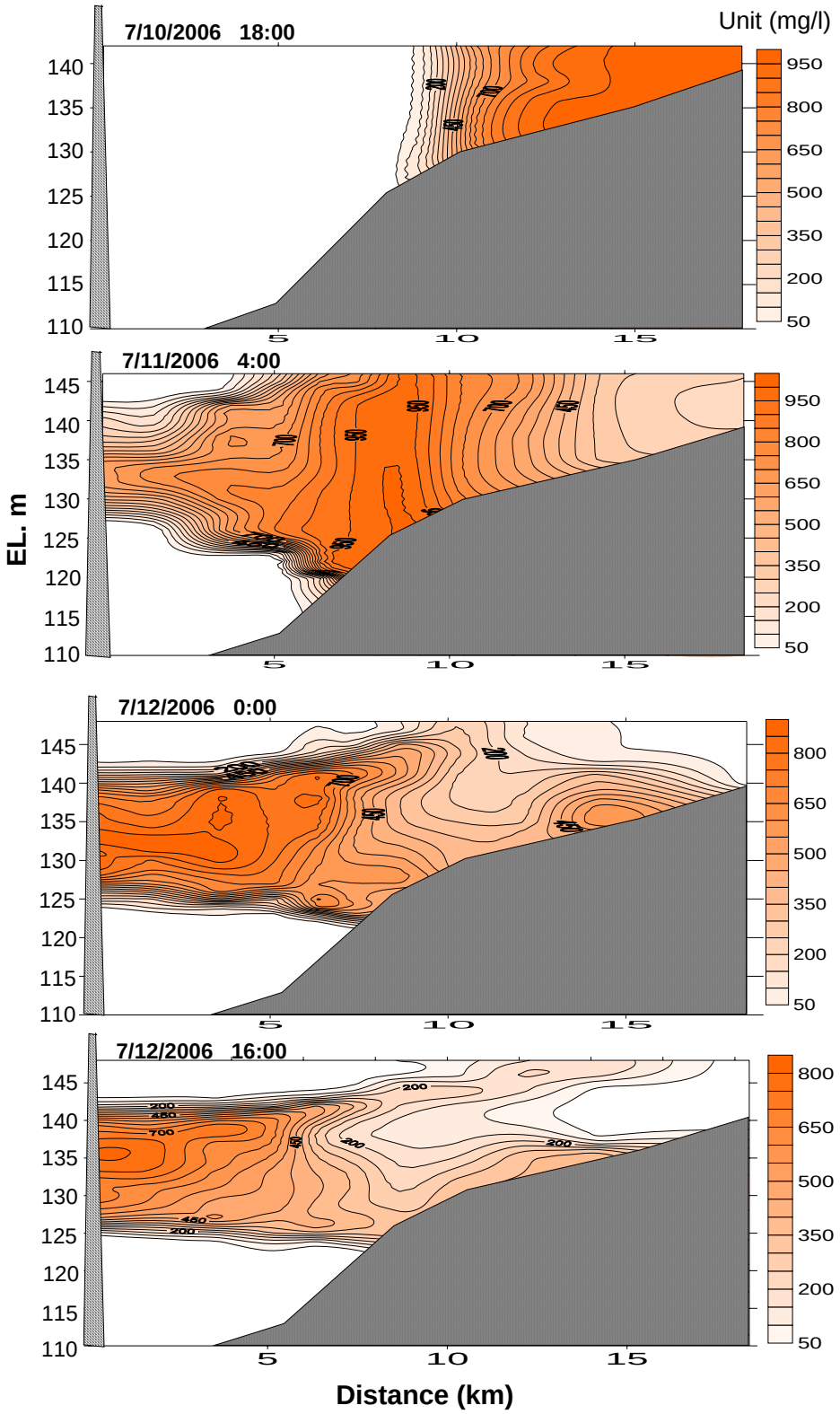

Figure 6.11 Simulated longitudinal transects of suspended sediment concentration (mg/*l*). Contours, ranging from 50 to 1000 mg/*l* in increments of 50 mg/*l*, were made with profile data at 11 points along the longitudinal direction of the reservoir thalweg.

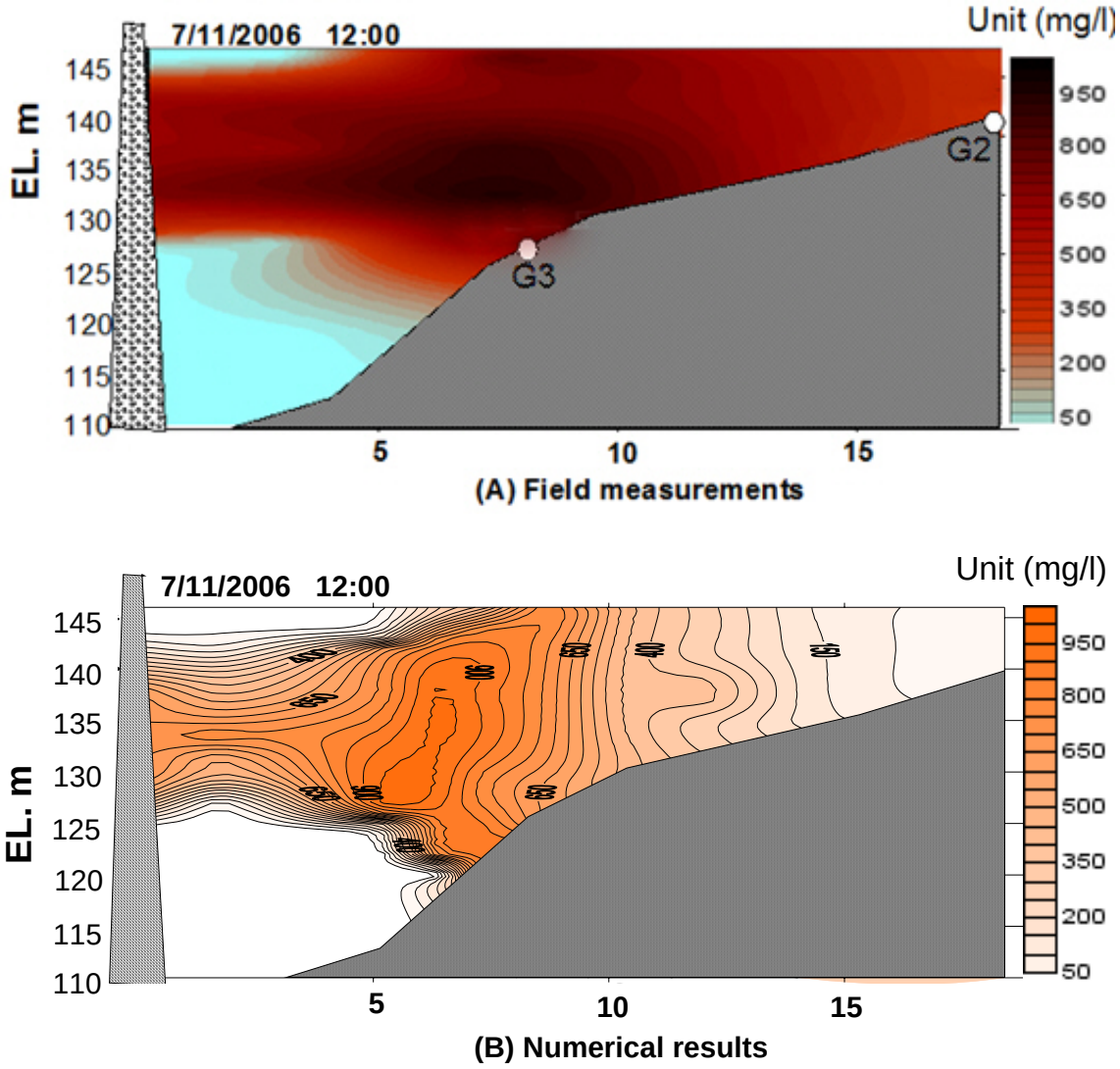

Figure 6.12 Comparison of measured (a) and computed (b) sediment concentrations along the longitudinal transect of Imha Reservoir on July 11, 12:00.

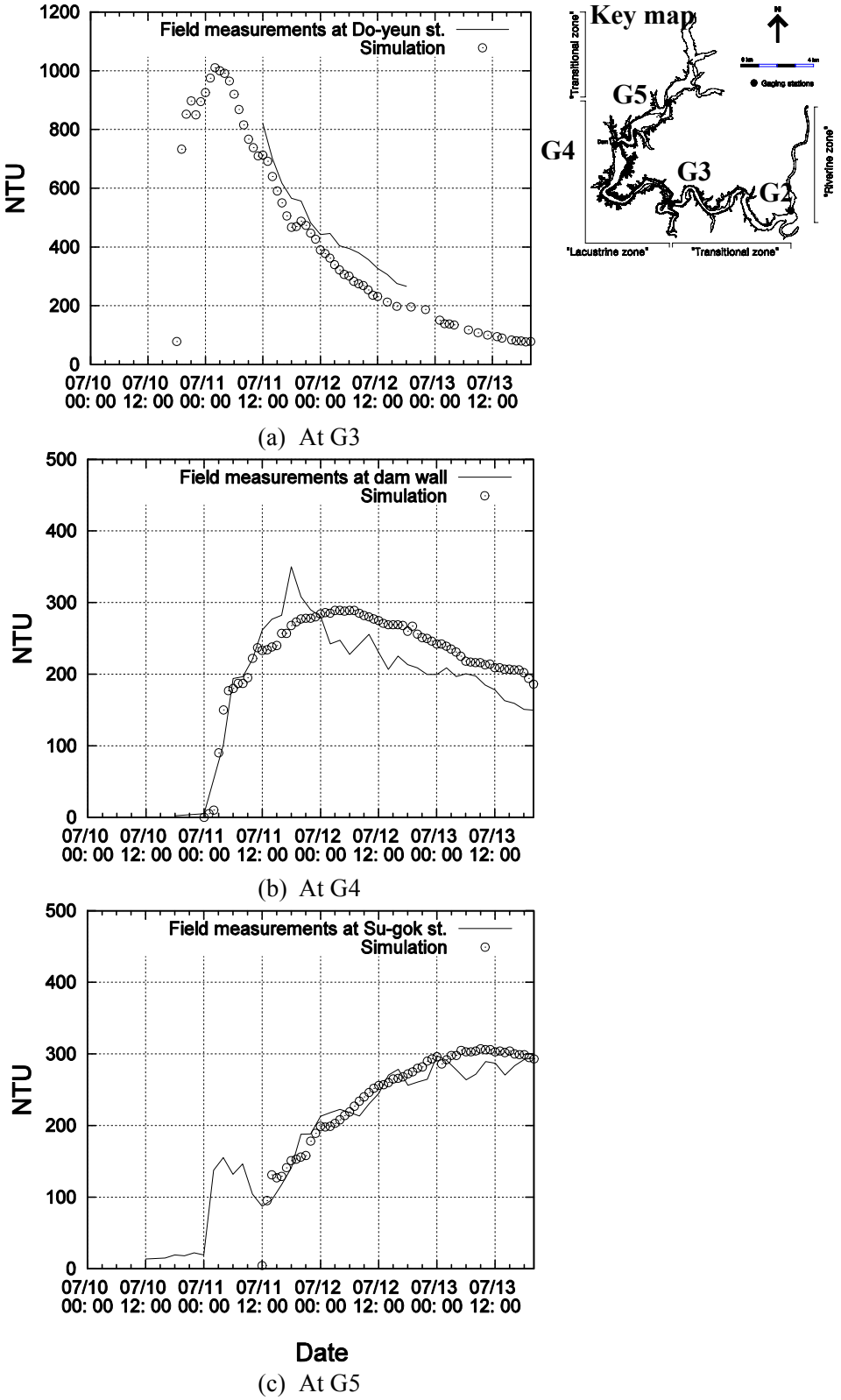

Figure 6.13 Time-series plots used to display the simulated time variations of NTU, depth-averaged, at three observation points with the comparison to the field measurements.

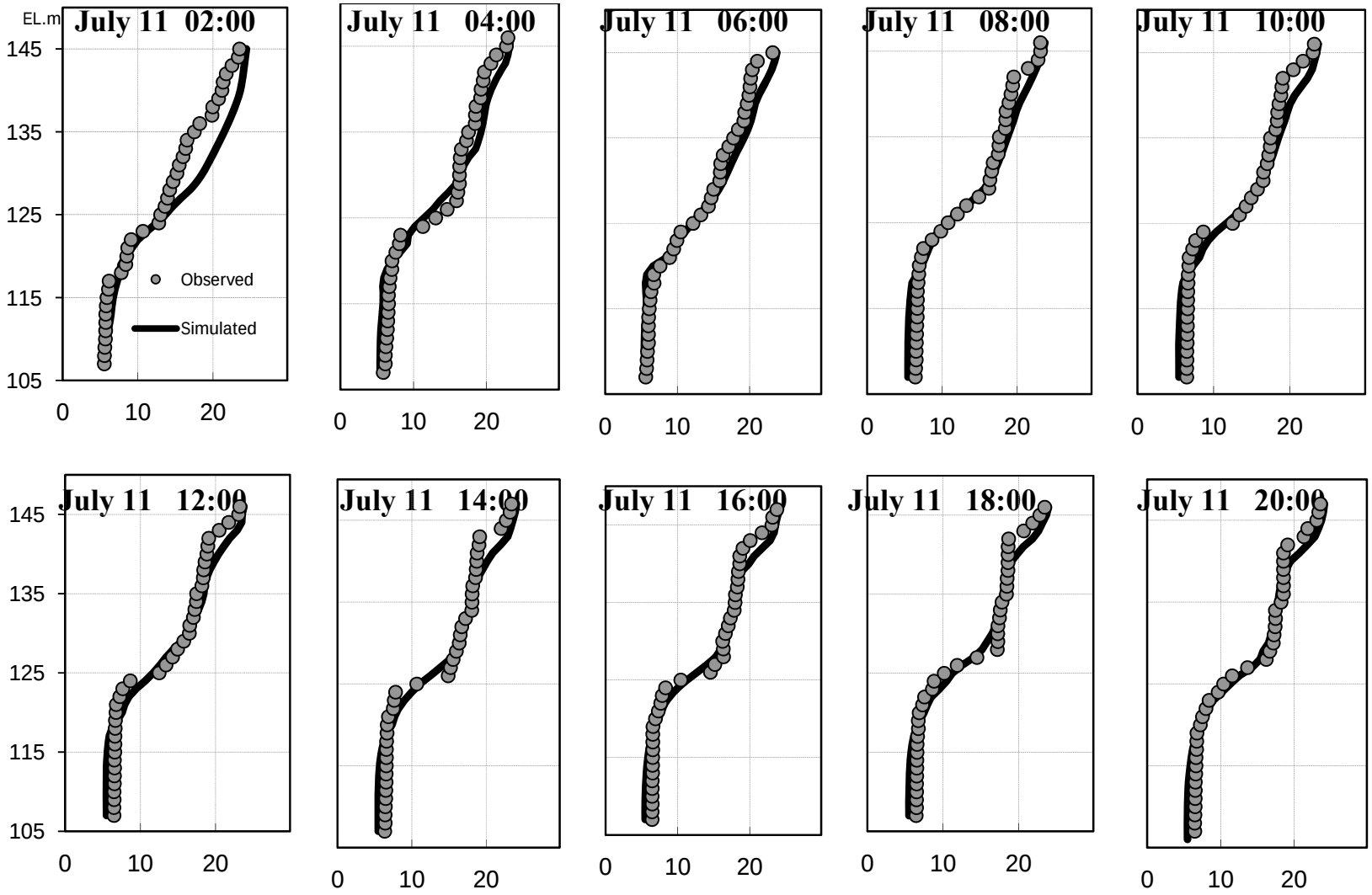

Figure 6.14 Comparisons of water temperature profiles between the numerical model (lines) and field measurements (circles) at G4.

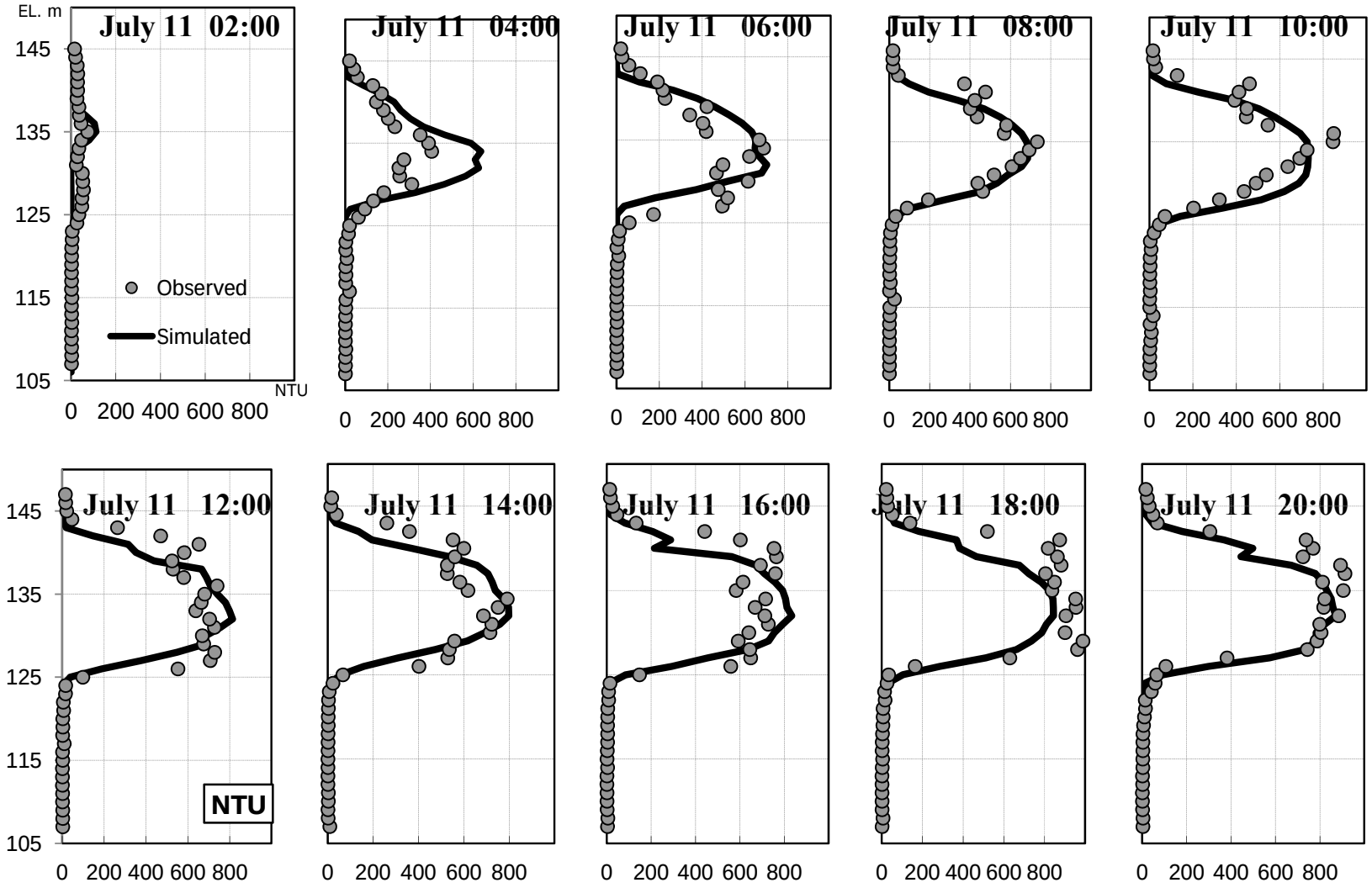

Figure 6.15 Comparisons of turbidity (NTU) profiles between the numerical model (lines) and field measurements (circles) at G4.

The vertical distributions of suspended sediment concentration along a longitudinal transect were presented in Figure 6.11. These transects demonstrate the temporal and spatial evolution of the turbid density currents changing from plunging flows to interflows. Figure 6.12 shows the comparison of measured and computed sediment concentrations along the longitudinal transect of Imha Reservoir on July 11, 12:00. The numerical prediction is in good agreement with field measurements.

The simulated intrusion level, depth, and temperature profiles were illustrated in Figure 6.14 and Figure 6.15. They intruded along the level of the thermocline with increasing depth, where the centre line of the intrusions was approximately EL 135.0 m and the depth of the intrusions ranged from 15 m to 20 m. It is difficult to define the intrusion depth exactly due to interfacial mixing.

The numerical model was also validated by comparisons to field measurements: (1) time-series turbidity data at G3, G4, and G5; and (2) temperature profiles and sediment concentration profiles. The comparison to the time-series turbidity data at G3, G4, and G5 clearly indicates that the model accurately reproduced the propagation speed of the turbid density intrusions. We assessed the forecasting performance of the numerical model using absolute mean error (AME) and root mean square error (RMSE), as defined as Equation (4.32) and (4.33). Average AME and RMSE for temporal turbidity variations were 37 and 47 NTU, respectively, provided by comparing with the time series data of NTU measured at G3, G4, and G5 (time-series turbidity data). AME and RMSE for water temperature profiles were calculated to be 1.0 ^{o}C and 1.3 ^{o}C over a range of 5-24 ^{o}C, respectively, based on the data shown in Figure 6.14. The numerical model provided very good prediction of temperature evolution induced by the intrusion of density currents. In order to assess the performance of predicting turbidity profiles, AME and RMSE were calculated using the NTU profile data shown in Figure 6.15. They were 72 and 136 NTU, respectively. Although the relatively large AME and RMSE for the prediction of turbidity profiles at G4 were presented, the numerical model accurately captured the intrusion level and depth of the density currents.

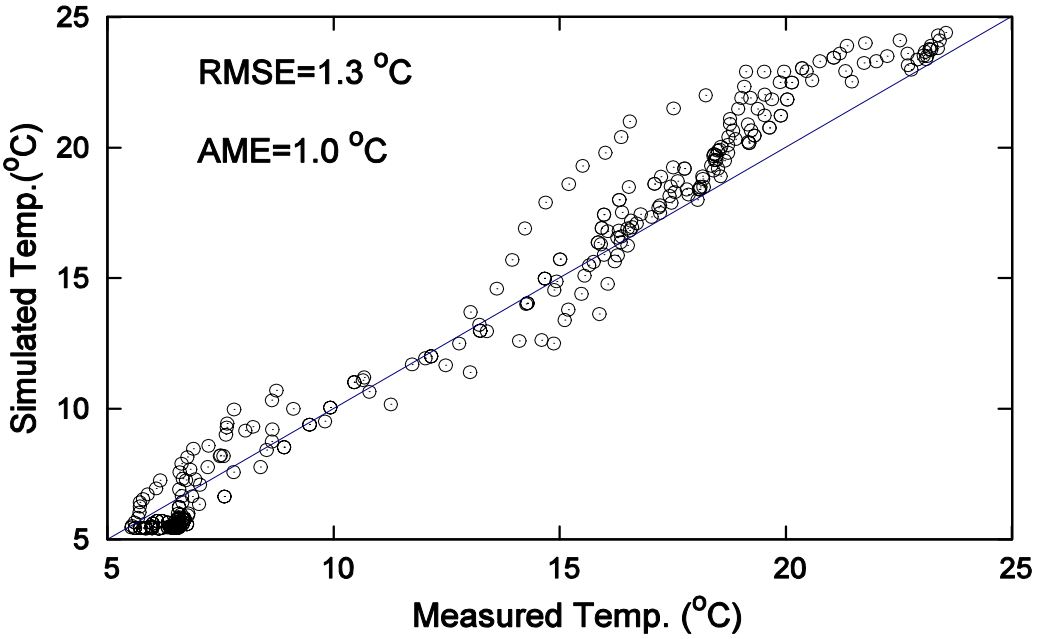

(a) Using the data presented in Figure 6.14

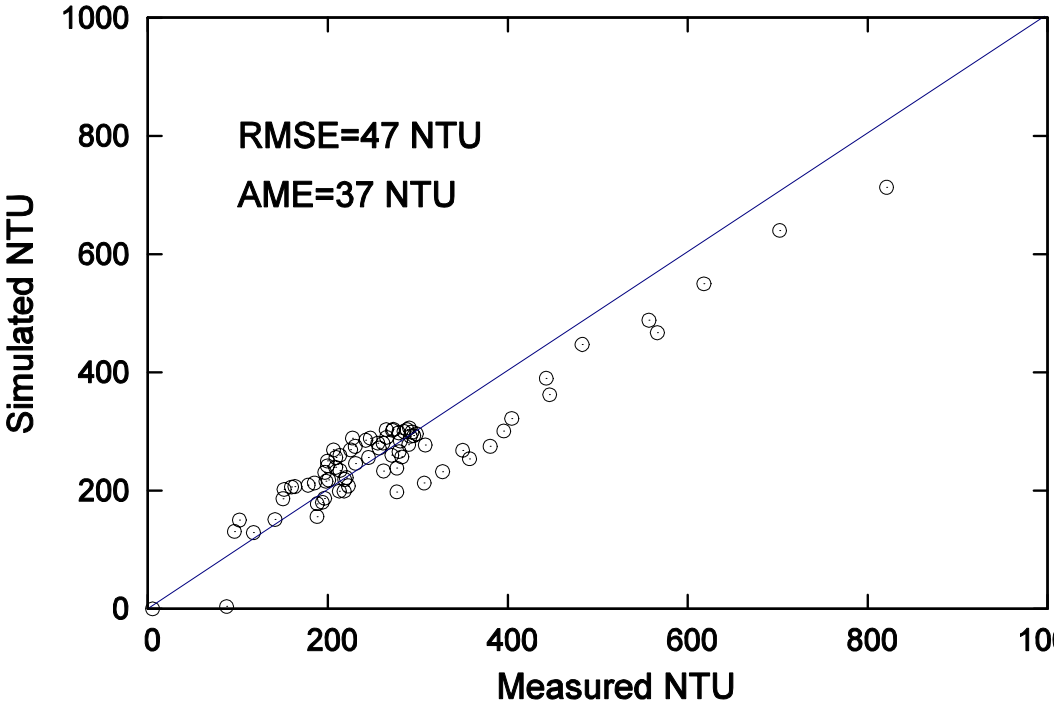

(b) Using the data presented in Figure 6.13

Figure 6.16 Quantitative evaluation of errors using AME and RMSE.

6.3.3 Parametric Analysis

A parametric analysis is performed to investigate the influence of important parameters: (1) sediment particle size; (2) sediment concentration; and (3) seasonal reservoir stratification on the fate of density currents in Imha Reservoir.

Effect of Sediment Particle Size

The simulations are carried out with different particle sizes and the responses of the turbid density currents are examined. The water inflows and temperature, and sediment inflows at the inlet point (G2), are set equal to the field measurements during Typhoon Ewiniar in July 2006.

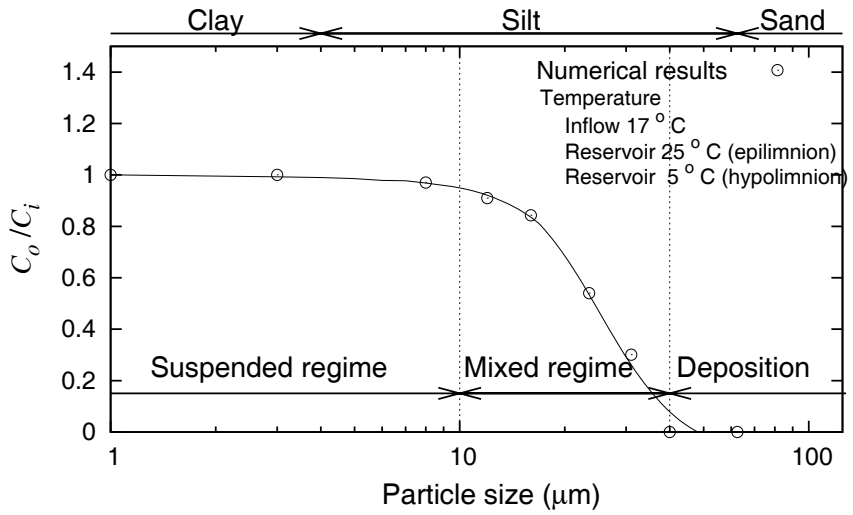

Figure 6.17 Sediment delivery ratio (C_o/C_i) as a function of particle size. C_i is the incoming sediment load from the inlet point (G2). C_o is the sediment concentration horizontally transported to Imha dam wall (G4) only along the thermocline (EL. 125-135m, see Figure 5.11).

Figure 6.17 shows the sediment concentration delivered to the dam wall (G4) along the initial thermocline level (EL. 125~135 m) as a function of particle size. It clearly indicates that the particle size affects the dynamics of turbid density currents entering the reservoir. The delivery ratio C_o/C_i decreases primarily with the increasing particle size. However, when particle size d_s is less than 10 μm, the incoming sediment concentration from the reservoir inlet (G2) will be

transported without concentration reduction due to sediment deposition. It is assumed that the settling velocity of $d_s < 10\,\mu\mathrm{m}$ is sufficiently small and negligible. In contrast, if the sediment particles become larger, they may rapidly decrease the concentration of the turbid density currents by the particles' deposition. When the particle sizes d_s are greater than $40\,\mu\mathrm{m}$, they will rapidly settle before reaching the Imha Dam (G4). However, most of them probably settle while they pass through riverine or transitional zone. Thus, it is assumed that the horizontally intrusive turbid currents (i.e., interflows) do not contain the large particles in the lacustrine zone. In other word, the turbid inflows entering the reservoir may consist of various particle sizes, but only very small size particles can be transported to the dam wall by interflows. As a result, if most of the turbid density currents belong to the interflow regime, the effect of sediment particle size on simulation results can be negligible.

Effect of Sediment Load

When river inflows containing high sediment concentration enter a reservoir, the concentration probably influences the formation and propagation of density currents. We performed numerical simulations to evaluate the response of density flows to the changes of incoming sediment concentration from G2. The sediment inflows were assumed to consist of only very small size particles less than $1.0\,\mu\mathrm{m}$ so that the buoyancy loss due to their deposition could be neglected. The inflows and associated temperature entering the reservoir at G2 were specified to be equal to the field measurements during Typhoon Ewiniar. The initial thermal stratification of the reservoir was specified to be identical to the temperature profile measured on July 10, 2006.

Figure 6.18 presents three flow regimes determining the intrusion types of density currents: (1) the river inflows will form interflows when the sediment concentration C_i is less than 2000 mg/l; (2) when C_i is between 2000 mg/l and 3000 mg/l, they will form multiple intrusions (i.e., interflows and underflows); and (3) when C_i is greater than 3000 mg/l, they will plunge and

propagate as underflows. These threshold values (2000 mg/l and 3000 mg/l) can be used to practically predict the formation of turbid density currents, flow type, and intrusion level in Imha Reservoir.

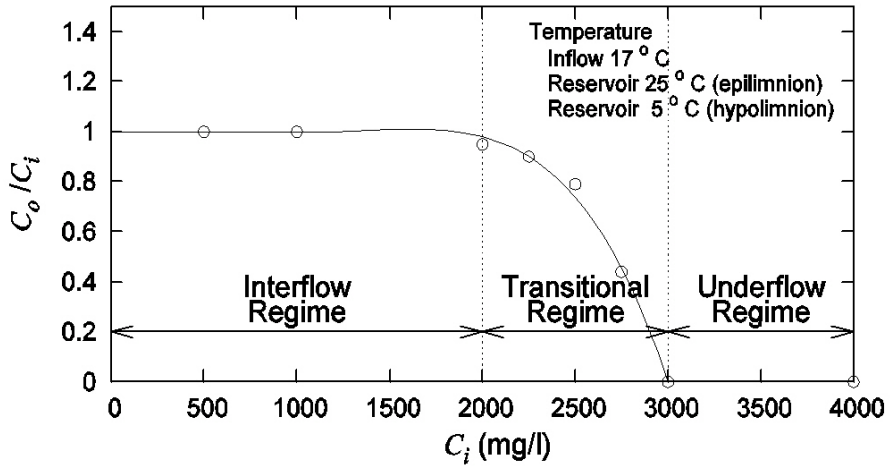

Figure 6.18 Propagation types of turbid density currents, classified into three flow regimes based on their sediment loads.

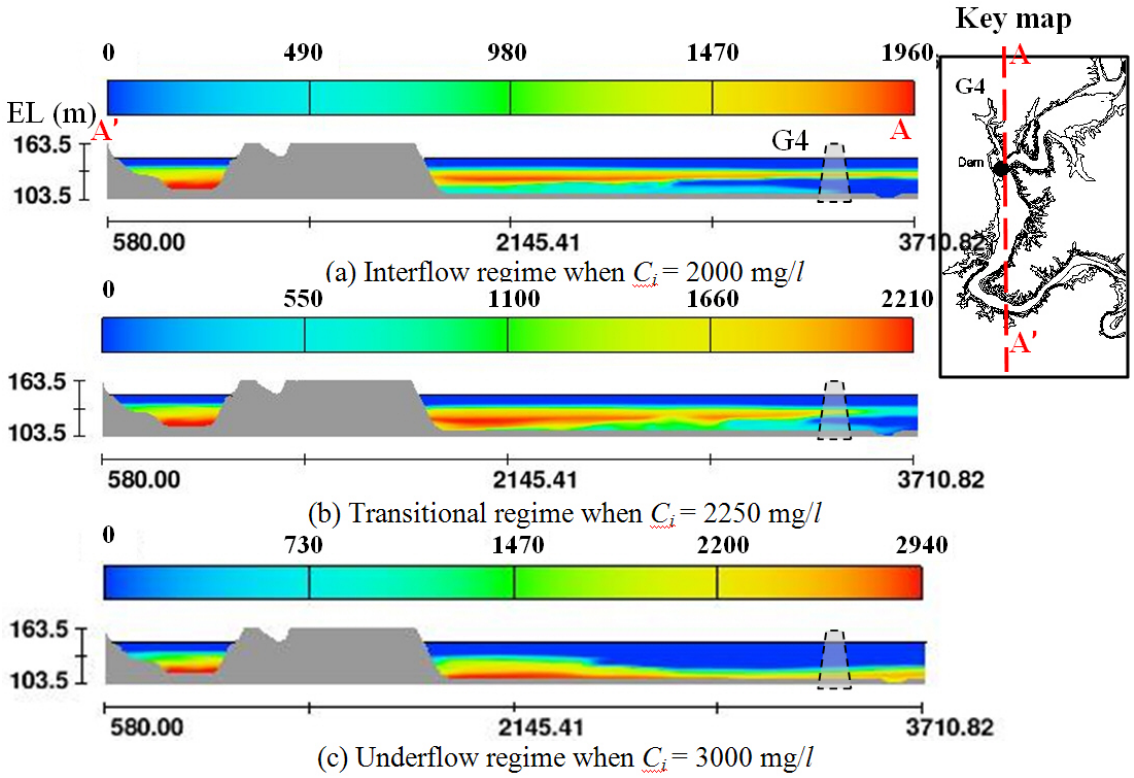

Figure 6.19 Longitudinal transects from Imha Dam wall (G4) to approximately 3.0 km upstream, showing intrusion types as a function of concentration.

In the interflow regime (C_i < 2000 mg/l), it is assumed that the dominant factor determining intrusion level will be the inflow temperature rather than the sediment concentration. During Typhoon Ewiniar, the tributary temperature drop observed during the typhoon was 7~8 ^{o}C compared to the temperature of the epilimnion (see Figure 5.8), and leading to water density increases of 1.6~1.7 kg/㎥. In addition to the temperature drop, the sediment concentration ranged from 500 to 2000 mg/l in the interflow regime, which could lead to the density increase of 0.3~1.2 kg/㎥. Considering the maximum sediment concentrations observed during typhoons reached just up to 1000 mg/l, the inflow temperature will be a most important parameter to demine intrusion level of turbid density currents.

Effect of Seasonal Stratification

We explore the effect of seasonal thermal structure of the reservoir on the turbid density currents. Density currents are generally developed because of the density differences between inflows and the receiving reservoir. Figure 6.20 shows the seasonal variation between the inflow temperatures and reservoir temperatures during 2006. It provides a reasonable prediction for the intrusion level of turbid density currents.

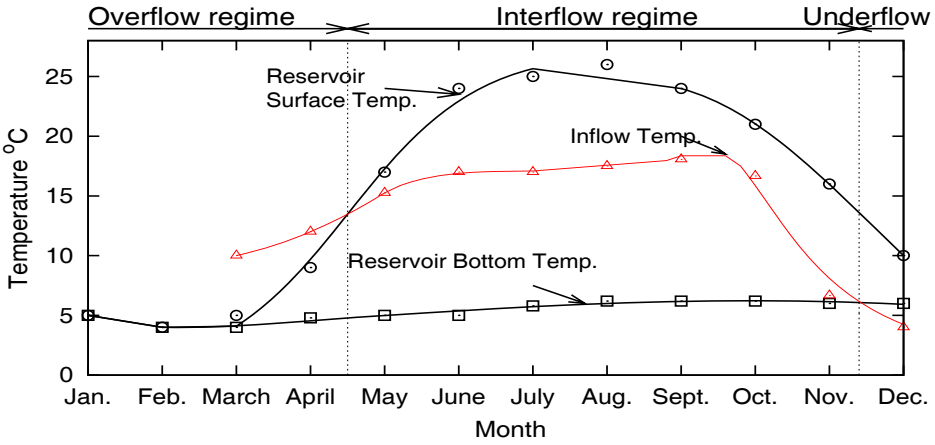

Figure 6.20 Seasonal variation in the temperature of inflows and the reservoir, measured during 2006. The temperatures of the reservoir were monthly averaged values, while the inflow temperatures were measured right after rainfall events.

Until the early spring, the reservoir was still colder than the river inflows. The river inflows in March could form overflow when they enter the reservoir with negligible sediment load because their densities are lighter than their surrounding reservoir water. In contrast, in December, the reservoir is still warmer than the river inflows. So, the propagation pattern can be expected to be underflows when they enter the reservoir in the winter period. After April, the thermal stratification occurs and then the reservoir becomes strongly stratified into three zones. In the summer period, it was observed that the temperatures of river inflows entering the reservoir were colder than the epilimnion of the reservoir (i.e., near the surface), while warmer than the hypolimnion (i.e., near the bottom). This relationship between the summer stratification and the temperature of the river inflows determines the intrusion level and generally, in the summer period, the inflows form interflow propagating horizontally along the thermocline.

In order to test the validity of the above mentioned hypothesis, we carried out numerical simulations considering the monthly thermal structure of the reservoir and the monthly temperature of the river inflows based on the field measurements. The river inflows with sediment loads for specifying boundary conditions for the numerical simulations were set to be identical to the conditions during Typhoon Ewiniar. Numerical results demonstrate that the summer stratification is strongly connected with the formation of turbid interflows in the reservoir, as shown in Figure 6.21. Comparatively, winter conditions will typically produce underflows without turbidity problems and spring conditions will develop overflows.

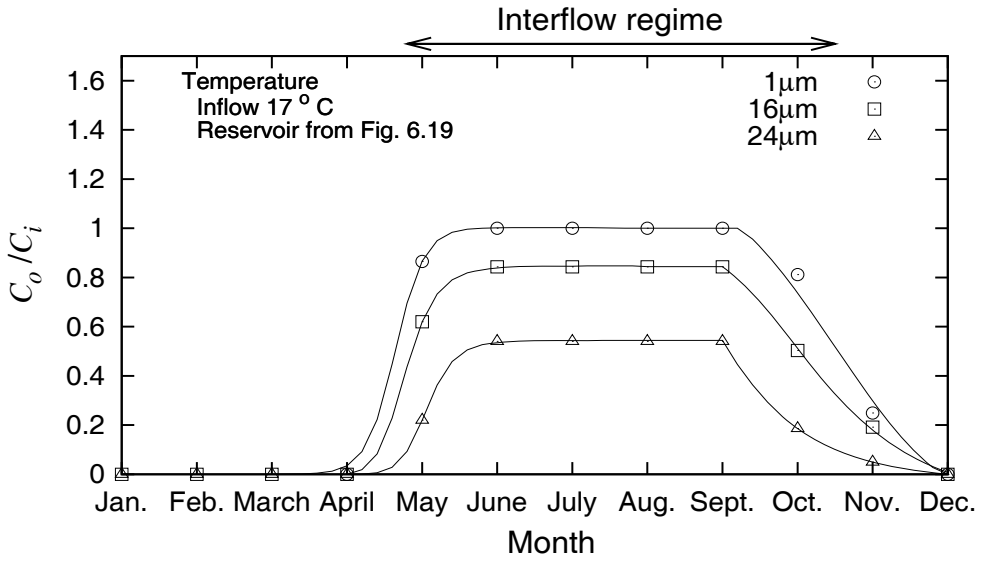

Figure 6.21 Effect of seasonal variations of thermal structure in the reservoir and inflow temperature on the turbid density currents. C_i is the sediment concentration of inflows entering the reservoir. C_o is the sediment concentration horizontally transported to the dam wall only along the thermocline (EL. 125~135 m, see Figure 5.11).

6.4 Conclusions

In this chapter, we applied the three-dimensional numerical model that is suitable for simulating turbid density currents horizontally intruding into the morphologically complex reservoir. This model can present 3-dimensioal predictions in temporal and spatial evolution with the longitudinal dispersion and the lateral mixing in meander loops. The model used here includes the particle dynamics algorithm that we developed to incorporate the effect of particle settling and density difference due to both sediment particles and fluid temperature.

SS-NTU relationships were developed from the field data at G2 and G4 and adequately adjusted through calibration. Application of the numerical model to turbid density flows in Imha Reservoir with SS/NTU = 1.0 at G4 and SS/NTU = 0.4 provided a good agreement with field measurements. The simulation results were compared with field data and showed good quantitative agreement for predicting the intrusive celerity and intrusion depth of turbid density currents

propagating into Imha Reservoir. AME and RMSE for water temperature profiles were calculated to be 1.0 ^{o}C and 1.3 ^{o}C, respectively. The average AME and RMSE were 37 and 47 NTU between the measured and the simulated NTU at G3, G4, and G5.

We numerically investigated the effect of wind-driven mixing on thermal structures of the reservoir during the typhoon. The numerical simulations showed that the tilted interfacial layers between the epilimnion and the thermocline occurred during the typhoon, but they did not contribute to significant change in the structure of stratification. Thus, the effect of wind-driven forces during the typhoon can be negligible during the simulation periods.

We derived (see Appendix A.3) and tested the analytical solution to estimate the intrusive celerity and depth of turbid density currents. The analytical solution provided a practical prediction of the celerity and depth of intrusive turbid density currents compared to field measurements. It was estimated that the sediment transport rate by the density currents during the typhoon reached approximately 50,000 tons/day.

We showed the response of density flows to the important parameters: (1) sediment particle sizes; (2) sediment concentration; and (3) seasonal stratification structure. Figure 6.17 clearly indicates that when the particle sizes d_s are less than $10\,\mu\text{m}$, the sediment inflows at the inlet point (G2) will be transported to the dam wall (G2) by interflows in suspension. When the particle sizes d_s are greater than $40\,\mu\text{m}$, they will rapidly settle before reaching the Imha Dam wall. Figure 6.18 presents three density flow regimes differing in the sediment concentration: (1) the density inflows will form interflows when the sediment concentration C_i is less than 2000 mg/l; (2) when C_i is between 2000 mg/l and 3000 mg/l, they will form multiple intrusions; (3) when C_i is greater than 3000 mg/l, they will form underflows. Figure 6.21 demonstrates that the summer stratification is strongly connected with the formation of interflows in the reservoir. This relationship between the summer stratification and the temperature of the river inflows determines the seasonal intrusion type and intrusion level.

Chapter 7

Conclusions

This dissertation provides a detailed analysis of turbid density flow regimes and propagation dynamics of the density currents in Imha Reservoir during Typhoon Ewiniar. We present highly resolved 3-D numerical simulations to investigate the propagation of density flows resulting from the complicated reservoir morphometry and various mixing processes. The influences of inflow characteristics and reservoir thermal structures on the turbid density currents intruding into Imha Reservoir were studied. A series of numerical simulations of lock-exchange currents was also carried out to test and validate the numerical model with and without the new particle dynamics algorithm. The main results obtained from this research are summarized as the following:

1. The finite-volume lock-exchange simulations were performed under the conditions identical to the laboratory experiments presented in the literature (Sutherland *et al.* 2004; Britter and Simpson 1981; Bolster *et al.* 2008). The simulated intrusive speeds were compared with the laboratory experiments and analytical solutions. The temporal evolutions were well illustrated with images taken from both the experiments and the numerical simulations, as shown in Figure 4.4. It is clear that the RANS with RNG $k-\varepsilon$ and LES method predict well the dynamics of IGC. Figure 4.5 shows that the numerical results compare very well with experimental measurements and the analytical solutions presented in Sutherland *et al.* (2004), Lowe *et al.* (2002), and Benjamin (1968). The simulations of IGC intruding into a stratified fluid were compared to the theoretical calculations and show good agreements with the solutions proposed by Bolster *et al.* (2008).

2. We developed a new particle dynamics algorithm that can be coupled with the FLOW-3D to simulate PDGC. The particle dynamics algorithm builds upon the original FLOW-3D code in two ways: (1) improves the original buoyant flow model in allowing the FLOW-3D code to compute simultaneously the changes in density via particle deposition, mixing, advection, and water temperature; and (2) includes multiple sediment sizes in mixtures as a function of particle size. This allows the simultaneous simulations of turbid density currents comprising different particle sizes. The experimental measurements of Gladstone *et al.* (1998) were used to validate the modified FLOW-3D model with the particle dynamics algorithm. Figure 4.16 indicates that the FLOW-3D model successfully captured the decreasing propagation speed due to the different deposition rates of different particle sizes. We extended our simulations to clarify the effect of particle sizes on the propagation dynamics of density currents and presented flow regimes describing the effect of particle size: (1) when d_s is less than about 10 μm, the particle-driven density currents belong to the suspended regime where all sediments can remain suspended and density currents travel long distances; (2) when $d_s > 40\ \mu$m, particles rapidly settle, resulting in a rapid loss in forward momentum and vanishing density currents; and (3) when $10\ \mu\text{m} < d_s < 40\ \mu$m, some particles will settle quickly, but others remain suspended for a long time, which affects the propagation dynamics of the density currents.
3. We proposed the turbidity current modeling framework suitable for Imha Reservoir. It was developed for use of turbidity and temperature data transmitted from the real-time monitoring system. The particle dynamics algorithm is used to simulate turbid density currents consisting of different particle sizes and validated against field measurements of Imha Reservoir. In the field validation, AME and RMSE for the prediction in water temperature profiles were calculated to be 1.0 ^{o}C and 1.3 ^{o}C, respectively. For turbidity simulations, the average AME

and RMSE were 37 and 47 NTU between the simulated and the measured turbidity at station G3, G4, and G5.

4. Analytical solutions to estimate the intrusive celerity and depth of turbid density currents were derived and compared to field measurements. It was also approximately estimated that the sediment transport rate by the turbid interflows reached approximately 50,000 tons/day during Typhoon Ewiniar. A detailed parametric analysis at Imha Reservoir showed that when the particle sizes d_s are less than $10\,\mu\mathrm{m}$, the sediment inflows at the inlet point (G2) will be transported to Imha Dam (G4) by interflows in suspension. In this regime, the density currents can be treated as non-particulate flows. When the particle sizes d_s are greater than $40\,\mu\mathrm{m}$, they will rapidly settle before reaching the Imha Dam. Therefore, highly concentrated turbid interflows occur only when d_s is less than the threshold value of $10\,\mu\mathrm{m}$. Figure 6.18 presents three density flow regimes differing in sediment concentration: (1) the river inflows will form interflows when the sediment concentration C_i is less than 2000 mg/l; (2) when C_i is between 2000 mg/l and 3000 mg/l, they will form multiple intrusions; and (3) when C_i is greater 3000 mg/l, they will plunge and propagate as underflows. Therefore, highly concentrated turbid interflows could not occur when C_i is more than the threshold value of 3000 mg/l. We also showed the response of density flows to seasonal thermal structure of the reservoir. Figure 6.21 demonstrates that the summer stratification is strongly connected with the formation of interflows in the reservoir. This relationship between the summer stratification and temperature of the river inflows contributes to determining the seasonal intrusion type and level when the density inflows enter the reservoir. In this parametric study, we presented the range of values ($10\,\mu\mathrm{m} < d_s < 40\,\mu\mathrm{m}$ and $2000\ \mathrm{mg}/l < C_i < 3000\ \mathrm{mg}/l$) that provide practical predictions for the type of density currents to be expected at Imha Reservoir.

REFERENCES

Adams, E., Stolzenbach, K., and Harleman, D. (1975). "Near and Far Field Analysis of Buoyant Surface Discharges into Large Bodies of Water." *Technical Rep. No. 205, R.M. Parsons Laboratory for Water Resources and Hydrodynamics*.

Ahlfeld, D., Joaquin, A., Tobiason, J., and Mas, D. (2003). "Case Study: Impact of Reservoir Stratification on Interflow Travel Time." *Journal of Hydraulic Engineering*, 129(12), 966.

Akiyama, J., and Stefan, H. G. (1984). "Plunging Flow into a Reservoir: Theory." *Journal of Hydraulic Engineering*, 110(4), 484.

Alavian, V., Jirka, G. H., Denton, R. A., and Johnson, M.C. (1992). "Density Currents Entering Lakes and Reservoirs." *Journal of Hydraulic Engineering*, 118(11), 1464-1489.

Antar, N., and Moodie, T. B. (2003). "Weakly Nonhydrostatic Effects in Compositionally-Driven Gravity Flows." *Studies in Applied Mathematics*, 111(2), 239-267.

Ardjosoediro, I., and Ramnarine, I. W. (2002). "The Influence of Turbidity on Growth, Feed Conversion and Survivorship of the Jamaica Red Tilapia Strain." *Aquaculture*, 212(1-4), 159-165.

Bae, D., Jung, I., and Chang, H. (2008). "Long-term Trend of Precipitation and Runoff in Korean River." *Hydrological Processes*, 2644- 2656.

Balistrieri, L., Tempel, R., Stillings, L., and Shevenell, L. (2006). "Modeling Spatial and Temporal Variations in Temperature and Salinity during Stratification and Overturn in Dexter Pit Lake, Tuscarora, Nevada, USA." *Applied Geochemistry*, 21(7), 1184-1203.

Bell, V., George, D., Moore, R., and Parker, J. (2006). "Using a 1-D Mixing Model to Simulate the Vertical Flux of Heat and Oxygen in a Lake Subject to Episodic Mixing." *Ecological Modelling*, 190(1-2), 41-54.

Benjamin, T. B. (1968). "Gravity Currents and Related Phenomena." *Journal of Fluid Mechanics,* 31(02), 209–248.

Bolster, D., Hang, A., and Linden, P. (2008). "The Front Speed of Intrusions into a Continuously Stratified Medium." *Journal of Fluid Mechanics,* 594, 369–377.

Britter, R. E., and Linden, P. F. (2006). "The Motion of the Front of a Gravity Current Travelling down an Incline." *Journal of Fluid Mechanics*, 99(03), 531.

Britter, R. E., and Simpson, J. E. (1981). "A Note on the Structure of the Head of an Intrusive Gravity Current." *Journal of Fluid Mechanics*, 112, 459-466.

Cantero, M. I., Garcia, M. H., Buscaglia, G. C., Bombardelli, F. A., and Dari, E. A. (2003). "Multidimensional CFD Simulation of a Discontinuous Density Current." *Proc. XXX IAHR Congress*, 405-412.

Cesare, D. G., Boillat, J.L., and Schleiss, A. J. (2006). "Circulation in Stratified Lakes due to Flood-induced Turbidity Currents." *Journal of Environmental Engineering*, 132(11), 1508-1517.

Chen, X. (2005). "A Comparison of Hydrostatic and Nonhydrostatic Pressure Components in Seiche Oscillations." *Mathematical and Computer Modelling*, 41(8-9), 887-902.

Chen, Y. J. C., Wu, S. C., Lee, B. S., and Hung, C. C. (2006). "Behavior of Storm-Induced Suspension Interflow in Subtropical Feitsui Reservoir, Taiwan." *Limnology and Oceanography*, 51(2), 1125–1133.

Cheng, R. T., and Casulli, V. (2001). "Evaluation of the UnTRIM Model for 3-D Tidal Circulation." In: Proc. of the 7th International Conference on Estuarine and Coastal Modeling. St. Petersburg, FL, 628-642.

Cheong, H.-B., Kuenen, J.J.P., Linden, P.F. (2006). "The Front Speed of Intrusive Gravity Currents." *Journal of Fluid Mechanics*, 552, 1-11.

Chikita, K., and Okumura, Y. (1990). "Dynamics of Turbidity Currents Measured in Katsurazawa Reservoir, Hokkaido, Japan." *Journal of Hydrology*, 117(1-4), 323-338.

Choi, S.U., and García, M. H. (2002). "k–ε Turbulence Modeling of Density Currents Developing Two Dimensionally on a Slope." *Journal of Hydraulic Engineering*, 128(1), 55.

Chung, S. W., Hipsey, M.R., and Imberger, J. (2009). "Modelling the Propagation of Turbid Density Inflows into a Stratified Lake: Daecheong Reservoir, Korea." *Environmental Modelling & Software*, Elsevier Ltd, 24(12), 1467-1482.

Chung, S.W., and Gu, R. (1998). "Two-Dimensional Simulations of Contaminant Currents in Stratified Reservoir." *Journal of Hydraulic Engineering*, 124(7), 704.

Cole, T. M., and Wells, S. A. (2006). *CE-QUAL-W2: A Two-Dimensional, Laterally Averaged, Hydrodynamic and Water Quality Model, Version 3*," Instruction Report EL-06-01. Vicksburg, MS.

Crosa, G., Castelli, E., Gentili, G., and Espa, P. (2009). "Effects of Suspended Sediments from Reservoir Flushing on Fish and Macroinvertebrates in an Alpine Stream." *Aquatic Sciences*, 72(1), 85-95.

Dai, A., Cantero, M. I., and Garcia, M. H. (2009). "Analysis of Plunging Flows." *Journal of Hydraulic Research*, 47(5), 638-642.

De Rooij, F., Linden, P., and Dalziel, S. B. (1999). "Saline and Particle-driven Interfacial Intrusions." *Journal of Fluid Mechanics,* 389, 303–334.

Dermissis, V., and Partheniades, E. (1984). "Interfacial Resistance in Stratified Flows." *Journal of Waterway, Port, Coastal and Ocean Engineering*, 110(2), 231-250.

Effler, S., Prestigiacomo, A., Peng, F., Bulygina, K., and Smith, D. (2006). "Resolution of Turbidity Patterns from Runoff Events in a Water Supply Reservoir, and the Advantages of In Situ Beam Attenuation Measurements." *Lake and Reservoir Management*, 22(1), 79-93.

Elder, R. A., and Wunderlich, W. O. (1972). "Inflow Density Currents in TVA Reservoirs." Proceedings of International Symposium on Stratified Flows, ASCE, 221-235.

Elliott, Z. and Venayagamoorthy, S. K. (2011). "Evaluation of turbulent Prandtl (Schmidt) number parameterizations for stably stratified environmental flows." Dynamics of Atmospheres and Oceans, 51 (2011), 137-150.

Ellison, T. H., and Turner, J. S. (1959). "Turbulent Entrainment in Stratified Flows." *Journal of Fluid Mechanics*, 6(03), 423-448.

Fang, X. (2004). "Simulation of Thermal/dissolved Oxygen Habitat for Fishes in Lakes under Different Climate Scenarios Part 1. Cool-water Fish in the Contiguous US." *Ecological Modelling*, 172(1), 13-37.

Farrell, G. J., and Stefan, H. G. (1986). "Buoyancy Induced Plunging Flow into Reservoirs and Coastal Regions." National Science Foundation Washington, D.C. 20550, Minnepolis, Minnesota 55414.

Farrell, G. J., and Stefan, H. G. (1988). "Mathematical Modeling of Plunging Reservoir Flows." *Journal of Hydraulic Research*, 26(5), 525-537.

Faust, K. M., and Plate, E. J. (1984). "Experimental Investigation of Intrusive Gravity Currents Entering Stably Stratified Fluids." *Journal of Hydraulic Research*, 22(5), 315-325.

Fernandez, R. L., and Imberger, J. (2006). "Bed Roughness Induced Entrainment in a High Richardson Number Underflow." *Journal of Hydraulic Research*, 44(6), 725-738.

Fischer, H. U. B., List, E. J. O., Koh, R. C. Y., Imberger, Jorg, and Brooks, N. H. (1979). *Mixing in Inland and Coastal Waters*. Academic Press Inc.

Fleenor, W. E. (2001). Effects and Control of Plunging Inflows on Reservoir Hydrodynamics and Downstream Releases [Dissertation]. University of California Davis.

FLOW-3D (2007) User guide and manual release 9.3, Flow Science Inc, Santa Fe, NM.

Ford, D. E., and Johnson, M. C. (1983). "An Assessment of Reservoir Density Currents and Inflow Processes." Technical Report E-83-7, U.S. Army Engineer Waterways Experiment Station, Vicksburg, MS., NTIS No. AD A137 303

Fringer, O. B, Gerritsen, M. G, Street, R. L (2006) "An Unstructured-grid, Finite-Volume, Nonhydrostatic, Parallel Coastal Ocean Simulator. " *Ocean Modelling* 14, 139-173.

Gelda, R. K., and Effler, S. W. (2007). "Simulation of Operations and Water Quality Performance of Reservoir Multilevel Intake Configurations." *Journal of Water Resources Planning and Management*, 133(1), 78.

Geyer, W. R., and Smith, J. D. (1987). "Shear Instability in a Highly Stratified Estuary." *Journal of Physical Oceanography*.

Gill, A. E. (1982). *Atmosphere-ocean Dynamics. Philosophical Transactions. Series A*, Mathematical, Physical, and Engineering Sciences, Academic Press, New York.

Gladstone, C., Phillips, J. C., and Sparks, R. S. J. (1998). "Experiments on Bidisperse, Constant-Volume Gravity Currents: Propagation and Sediment Deposition." *Sedimentology*, 45(5), 833-843.

Gladstone, C., and Pritchard, D. (2010). "Patterns of Deposition from Experimental Turbidity Currents with Reversing Buoyancy." *Sedimentology*, 57(1), 53-84.

Gosink, J. (1987). "Northern Lake and Reservoir Modeling." *Cold Regions Science and Technology*, Elsevier, 13(3), 281–300.

Gu, R., Mccutcheon, S. C., and Wang, P. (1996). "Modeling Reservoir Density Underflow and Interflow from a Chemical Spill." *Water Resources Research*, 32(3), 695-705.

Hamrick, J. M. (1992). "A Three-Dimensional Environmental Fluid Dynamics Computer Code: Theoretical and Computational Aspects." *The College of William and Mary, Virginia Institute of Marine Science. Special Report 317*.

Han, S., Lee, Y., Seo, E., Shim, J., and Lee, J. (2007). "The Influence of Muddy Water in Imha Reservoir on the Ichthyofauna and Fish Growth." *Journal of Life Science*, 17(8), 1104-1110.

Harleman, D., and Stolzenbach, K. (1972). "Fluid Mechanics of Heat Disposal from Power Generation." *Annual Review of Fluid Mechanics*, 4, 7–32.

Hauenstein, W., and Dracos, T. (1984). “Investigation of Plunging Density Currents Generated by Inflows in Lakes.” *Journal of Hydraulic Research*, 22(3), 157-179.

Hebbert, B., Patterson, J., Loh, I., and Imberger, J. (1979). “Collie river Underflow into the Wellington Reservoir.” *Journal of the Hydraulics Division*, 105(5), 533–545.

Henley, W. F., Patterson, M. A., Neves, R. J., and Lemly, A. D. (2000). “Effects of Sedimentation and Turbidity on Lotic Food Webs: A Concise Review for Natural Resource Managers.” *Reviews in Fisheries Science*, 8(2), 125-139.

Hirt, C. W., and Nichols, B. D. (1981) “Volume of Fluid (VOF) Method for the Dynamics of Free Boundaries.” Journal of Computational Physics, 39, 1-11.

Hirt, C. W. (1993). “Volume-Fraction Techniques: Powerful Tools for Wind Engineering.” Journal of Wind Engineering and Industrial Aerodynamics, 46 & 47:327-338.

Hirt, C. W., and Sicilian, J. M. (1985) “A Porosity Technique for the Definition of Obstacles in Rectangular-Cell Meshes.” *Proceedings of the Fourth International Conference of Numerical Ship Hydrodynamics*, National Academy of Science, Washington, D.C., 450.

Hodges, B., and Dallimore, C. (2007). *Estuary, Lake and Coastal Ocean Model: ELCOM v2.2 User Manual*.

Hodges, B.R. (2009). “Hydrodynamical Modeling.” *In: Gene E. Likens, (Editor) Encyclopedia of Inland Waters. Oxford: Elsevier.*, 1, 613-627.

Holyer, J. Y., and Huppert, H. E. (1980). “Gravity Currents Entering a Two-layer Fluid.” *Journal of Fluid Mechanics*, 100(04), 739-767.

Hopfinger, E. (1978). “Buoyancy Effects on the Large Scale Structure of Free Turbulent Shear Flows.” *Structure and Mechanisms of Turbulence I;Proceedings of the Symposium on Turbulence*, Springer, 65–85.

Huppert, H. E. and Simpson, J. E. (1980). “The Slumping of Gravity Currents. ” *Journal of Fluid Mechanics*, 99, 785–799.

Hürzeler, B., Imberger, J, and Ivey, G. (1996). “Dynamics of Turbidity Current with Reversing Buoyancy.” *Journal of Hydraulic Engineering*, 122(5), 230-236.

Imberger, J., Thompson, R., and Fandry, C. (1976). “Selective Withdrawal from a Finite Rectangular Tank.” *Journal of Fluid Mechanics,* 78(03), 489–512.

Jain, S. C. (1981). “Plunging Phenomena in Reservoirs.” *Symposium on Surface Water Impoundments, ASCE, MN*, 1249-1257.

Johnson, N. M., and Merritt, D. H. (1979). "Convective and Advective Circulation of Lake Powell, Utah-Arizona, during 1972–1975." *Water Resources Research*, 15(4), 873.

Julien, P. Y. (1998). *Erosion and Sedimentation*. Cambridge University Press, New York.

K-water. (2004). "Study on the Effectiveness of Flocculants to Increase Particle Settling Velocity." Korea Water Resources Corporation (Imha office).

K-water. (2007). "Investigation of the Relationship between Turbid Water and Water Quality in Imha Reservoir; Technical Note." Korea Water Resources Corporation (Imha office).

Kao, T. (1977). "Density Currents and Their Applications." *Journal of the Hydraulics Division*, 103(HY5), 543-555.

Keulegan, G. H. (1949). "Interfacial Instability and Mixing in Stratified Flows." *Journal of Research of the National Bureau of Standards*, 43, 487–500.

Keulegan, G. H. (1957). Thirteenth Progress Report on Model Laws for Density Currents an Experimental Study of the Motion of Saline Water from Locks into Fresh Water Channels.U.S. Natl. Bur. Standards Rept. 5168

Kim, H. S. (2006). Soil Erosion Modeling Using RUSLE and Gis on the Imha Watershed, South Korea[Thesis]. Civil Engineering, Colorado State University.

Kirk, J. T. O. (1985). "Effects of Suspensoids (Turbidity) on Penetration of Solar Radiation in Aquatic Ecosystems." *Hydrobiologia*, 125(1), 195-208.

Koh, R. (1976). "Buoyancy-driven Gravitational Spreading." *Proceedings of the Coastal Engineering Conference*, 15, 2956-2975.

Komar, P. D. (1973). "Continuity of Turbidity Current Flow and Systematic Variations in Deep-Sea Channel Morphology." *Geological Society of America Bulletin*, 84(10), 3329-3337.

Kuenen, P. H. (1952). "Estimated Size of the Grand Banks Turbidity Current." *American Journal of Science*, 250, 874-884.

Kullenberg, B. (1954). "Remarks on the Grand Banks Turbidity Current." *Deep Sea Research (1953)*, 1(4), 203-210.

Lai, Y. G., Weber, L. J., and Patel, V. C. (2003). "Nonhydrostatic Three-Dimensional Model for Hydraulic Flow Simulation . I : Formulation and Verification." *Journal of Hydraulic Engineering*, 129(3), 196-205.

Laval, B., Imberger, J., Hodges, B.R., and Stocker, R. (2003). “Modeling Circulation in Lakes: Spatial and Temporal Variations.” *Limnology and Oceanography*, JSTOR, 48(3), 983–994.

Lee, G and Cho, G. (2004) “Evaluation of Gis-based Soil Erosion Amount with Turbid Water Data” *Korean Society for Geospatial Information System,* 12(4) 75-81.

Lee, H., and Yu, W. (1997). “Experimental Study of Reservoir Turbidity Current.” *Journal of Hydraulic Engineering*, 123(6), 520-528.

Liu, J., and Lou, P. (2005). "Study on Turbidity Outflow Problems at the Shimokodori Dam.” World Water & Environmental Resources Congress 2005, Anchorage, USA, May 15-20.

Lofquist, K. (1960). “Flow and Stress near an Interface between Stratified Liquids.” *Physics of Fluids*, 3(2), 158-175.

Lowe, R. J., Linden, P. F., and Rottman, J. W. (2002). “A Laboratory Study of the Velocity Structure in an Intrusive Gravity Current.” *Journal of Fluid Mechanics*, 456, 33-48.

Maxworthy, T., Leilich, J., and Simpson, J. (2002). “The Propagation of a Gravity Current into a Linearly Stratified Fluid.” *Journal of Fluid*, 453, 371-394.

Middleton, G V. (1993). “Sediment Deposition from Turbidity Currents.” *Annual Review of Earth and Planetary Sciences*, 21(1), 89-114.

Middleton, G.V. (1966 a). “Experiments on Density and Turbidity Currents: I. Motion of the Head.” *Canadian Journal of Earth Sciences*, NRC Research Press, 3(5), 627–637.

Middleton, G.V. (1996 b). “Experiments on Density and Turbidity Currents: II. Uniform Flow of Density Currents.” *Canadian Journal of Earth Sciences*, NRC Research Press, 3(5), 627–637.

Miles, J. W. (1961). “On the Stability of Heterogeneous Shear Flows.” *Journal of Fluid Mechanics*, 10(04), 496-508.

Miles, J. W., and Howard, L. N. (2006). “Note on a Heterogeneous Shear Flow.” *Journal of Fluid Mechanics*, 20(02), 331.

Morris, G. L., and Fan, J. (1998). *Reservoir Sedimentation Handbook*. McGraw-Hill Book Co., New York.

Parker, G., Garcia, M., Fukushima, Y., and Yu, W. (1987). “Experiments on Turbidity Currents over an Erodible Bed.” *Journal of Hydraulic Research*, 25(1), 123-147.

Parker, Gary, and Toniolo, H. (2007). "Note on the Analysis of Plunging of Density Flows." *Journal of Hydraulic Engineering*, 133(6), 690.

Patterson, M. D., Simpson, J. E., Dalziel, S. B., and Nikiforakis, N. (2005). "Numerical Modelling of Two-dimensional and Axisymmetric Gravity Currents." *International Journal for Numerical Methods in Fluids*, 47(10-11), 1221-1227.

Polk, E. M., Benedict, B. A., and Parker, F. L. (1971). "Cooling Water Density Wedges in Streams." *Journal of the Hydraulics Division*, 97(10), 1639–1652.

Quay, P., Broecker, W., and Hesslein, R. D. (1980). "Vertical Diffusion Rates Determined by Tritium Tracer Experiments in the Thermocline and Hypolimnion of Two Lakes." *American Society of Limnology and Oceanography*, 25(2), 201-218.

Richardson, L. (1920). "The Supply of Energy from and to Atmospheric Eddies." *Proceedings of the Royal Society of London. Series A,*, 97(686), 354-373.

Rodi, W. (1987). "Example of Calculation Methods for Flow and Mixing in Stratified flows." *Journal of Geophysical Research*, 92(C5), 5305-5328.

Safaie, B. (1979). "Mixing of Buoyant Surface Jet over Sloping Bottom." *Journal of the Waterway Port Coastal and Ocean Division*, 105(4), 357-373.

Savage, S. B., and Brimberg, J. (1975). "Analysis of Plunging Phenomena in Water Reservoirs." *Journal of Hydraulic Research*, 13(2), 187-205.

Shin, M., Lee, J., and Seo, E. (2009). "Effect of Muddy Water on the Fishes in Imha Reservoir." *Journal of Life Science*, 19(8), 1112-1118.

Simpson, J. E. (1987). *Gravity Currents: In the Environment and the Laboratory.* Cambridge University Press, New York.

Singh, B., and Shah, C. R. (1971). "Plunging Phenomenon of Density Currents in Reservoirs." *La Houille Blanche*, 26(1), 59-64.

Smagorinsky, J. (1963). "General Circulation Experiments with the Primitive Equations. I. The Basic Experiment." *Monthly Weather Review*, 91(3), 99-164.

Smith, V. H., Tilman, G. D., and Nekola, J. C. (1999). "Eutrophication: Impacts of Excess Nutrient Inputs on Freshwater, Marine, and Terrestrial Ecosystems." *Environmental pollution*, 100, 179-96.

Stigebrandt, A. (1978). "Dynamics of an Ice Covered Lake with Through-Flow." *Nordic Hydrology*, 9, 219-244.

Sutherland, B. R., Kyba, P. J., and Flynn, M. R. (2004). “Intrusive Gravity Currents in Two-layer Fluids.” *Journal of Fluid Mechanics*, 514, 327-353.

Taylor, A. G. I. (1931). “Effect of Variation in Density on the Stability of Superposed Streams of Fluid.” *Preceedings of the Royal Society of London. Series A.*, 132(820), 499-523.

Tetra Tech Inc. (2007). “The Environmental Fluid Dynamics Code User Manual US EPA Version 1.” *Tetra Tech, Inc.*

Turner, J. (1979). *Buoyancy effects in fluids*. Cambridge University Press, New York.

Ungarish, M. (2006). “On Gravity Currents in a Linearly Stratified Ambient: A Generalization of Benjamin's Steady-state Propagation Results.” *Journal of Fluid Mechanics*, 548, 49-68.

Van Houten, R. J. (1976). Hydrodynamics of Contained Oil Slicks [Dissertation]. Ocean Engineering, Massachusetts Institute of Technology.

Von Kármán, T. (1940). “The Engineer Grapples with Nonlinear Problems.” *Bulletin of the American Mathematical Society*, 46(8), 615-684.

Wadzuk, B. M., and Hodges, B. R. (2004). “Hydrostatic and Non-hydrostatic Internal Wave Models.” *CRWR Online Report 04-09, The University of Texas at Austin*, 83 pages.

Weilbeer, H., and Jankowski, J. (2000). “A Three-Dimensional Non-Hydrostatic Model for Free Surface Flows–Development, Verification and Limitations.” *Proc. Of 6th International Conference Estuarine and Coastal Modeling*, 162–177.

Wells, M., and Nadarajah, P. (2008). “The Intrusion Depth of Density Currents Flowing into Stratified Water Bodies.” *Journal of Physical Oceanography*, 39(8), 1935.

Wilkinson, D. L. (1972). “Dynamics of Contained Oil Slicks.” *Journal of the hydraulic division*, 98(6), 1013-1030.

Williams, N. (2007). “Modeling Dissolved Oxygen in Lake Powell using CE-QUAL-W2 [Theis].” *Brigham Young University*.

Yakhot, V., and Orszag, S. A. (1986). “Renormalization Group Analysis of Turbulence. I. Basic Theory.” *Journal of Scientific Computing*, Springer, 1(1), 3–51.

Yick, K. Y., Torres, C. R., Peacock, T., and Stocker, R. (2009). “Enhanced Drag of a Sphere Settling in a Stratified Fluid at Small Reynolds Numbers.” *Journal of Fluid Mechanics*, 632, 49.

Yoon, S.W., Chung, S.W., and Choi, J.K. (2008). "Variation of Inflow Density Currents with Different Flood Magnitude in Daecheong Reservoir." *Journal of Korea Water Resources Association*, 41(12), 1219-1230.

Yum, K. T., Cho, Y. D., Kim, J. Y., Ban, Y. J., and Jin, B. (2008). "Interdisciplinary Research for Pre-prevention Measures of Turbid Water with Watershed Units." *Proceedings of the Korea Water Resources Association Conference*, 544-549.

Çalışkan, A., and Elçi, Ş. (2008). "Effects of Selective Withdrawal on Hydrodynamics of a Stratified Reservoir." *Water Resources Management*, 23(7), 1257-1273.

Appendix Ⅰ

Date/time	Sec	Rain-fall (mm)	Total Inflow (CMS)	WSL (m)	Observed measurements					Modeling Input	
					G4 (NTU)	G3 (NTU)	G2 (NTU)	G1 (NTU)	Water depth at G2 (m)	SS (mg/l)	Tempera ture (^{o}C)
2006-07-10 1:00	3600	0.0	109.2	138.9					1.8		20.3
2006-07-10 2:00	7200	0.0	83.6	138.9	2.2			87.6	1.8	35	20.3
2006-07-10 3:00	10800	0.0	136.6	139.0					1.7	0	20.3
2006-07-10 4:00	14400	0.0	110.5	139.0	2.3			71.8	1.7	29	20.3
2006-07-10 5:00	18000	0.0	110.8	139.1					1.7	0	20.3
2006-07-10 6:00	21600	0.1	110.8	139.1	2.1	0.0		74.1	1.7	30	20.3
2006-07-10 7:00	25200	0.5	84.7	139.1					1.7	0	20.3
2006-07-10 8:00	28800	1.3	111.3	139.2	1.9			65.5	1.7	26	20.07
2006-07-10 9:00	32400	1.8	84.7	139.2				57.4	1.7	23	19.98
2006-07-10 10:00	36000	5.3	84.9	139.2				57.2	1.7	23	19.93
2006-07-10 11:00	39600	5.9	110.4	139.3				53.7	1.7	22	19.91
2006-07-10 12:00	43200	4.7	129.4	139.3	2.1			48.9	1.7	20	19.91
2006-07-10 13:00	46800	8.2	83.9	139.3				48.0	1.7	19	19.94
2006-07-10 14:00	50400	8.6	164.9	139.4				52.4	1.7	21	19.96
2006-07-10 15:00	54000	15.0	139.2	139.4				97.5	1.8	39	20.01
2006-07-10 16:00	57600	21.2	312.2	139.5	1.9			1323.2	2.3	529	20.15
2006-07-10 17:00	61200	5.6	423.8	139.6				2389.5	3.1	956	18.98
2006-07-10 18:00	64800	7.2	1317.3	140.1	2.3			2389.5	3.8	956	18.93
2006-07-10 19:00	68400	8.9	2392.9	140.9				2114.8	3.8	846	18.40
2006-07-10 20:00	72000	3.8	2652.9	141.8	2.3		2586.9	2389.6	4.7	956	18.37
2006-07-10 21:00	75600	1.3	2388.2	142.6				2145.3	4.7	858	18.00
2006-07-10 22:00	79200	0.0	2280.1	143.3	2.2		2443.6	1901.1	4.6	761	17.60
2006-07-10 23:00	82800	0.0	2152.6	143.9				1656.9	4.6	663	17.25
2006-07-11 0:00	86400	0.0	1937.3	144.5	5.1			1412.7	3.9	565	17.03
2006-07-11 1:00	90000	0.2	1593.7	144.9				981.3	3.5	393	16.83
2006-07-11 2:00	93600	0.3	1334.8	145.3	21.1			785.3	3.2	314	16.69
2006-07-11 3:00	97200	0.0	1098.4	145.6				704.6	2.9	282	16.65
2006-07-11 4:00	100800	0.0	927.0	145.9	101.7			618.8	2.8	248	16.65
2006-07-11 5:00	104400	0.0	786.5	146.1				517.5	2.8	207	16.67
2006-07-11 6:00	108000	0.0	641.8	146.2	193.9			412.5	2.4	165	16.74
2006-07-11 7:00	111600	0.0	570.7	146.4				357.6	2.4	143	16.84
2006-07-11 8:00	115200	0.0	497.3	146.5	196.3			358.5	2.4	143	16.95
2006-07-11 9:00	118800	0.0	461.5	146.6				256.7	2.3	103	17.10
2006-07-11 10:00	122400	0.0	425.4	146.7	220.6			213.2	2.2	85	17.24

Date/time	Sec	Rain-fall (mm)	Total Inflow (CMS)	WSL (m)	Observed measurements					Modeling Input	
					G4 (m)	G3 (m)	G2 (m)	G1 (m)	Water depth at G2 (m)	SS (mg/l)	Tempera ture
2006-07-11 11:00	126000	0.0	392.4	146.8				163.1	2.2	65	17.37
2006-07-11 12:00	129600	0.0	334.2	146.9	261.8	820.9		168.8	2.1	68	17.50
2006-07-11 13:00	133200	0.0	301.8	147.0				163.2	2.1	65	17.64
2006-07-11 14:00	136800	0.0	302.2	147.0	276.7	702.2	241.0	131.8	2.1	53	17.83
2006-07-11 15:00	140400	0.0	264.1	147.0				121.2	2.1	49	18.01
2006-07-11 16:00	144000	0.0	264.4	147.1	282.1	617.8	186.8		2.1	0	18.01
2006-07-11 17:00	147600	0.0	225.0	147.1				102.5	2.0	41	18.40
2006-07-11 18:00	151200	0.0	225.5	147.1	350.0	566.1	159.2	92.2	2.0	37	18.56
2006-07-11 19:00	154800	0.1	192.4	147.2				92.9	2.0	37	18.66
2006-07-11 20:00	158400	0.0	193.2	147.2	308.1	556.7	127.6	78.8	2.0	32	18.70
2006-07-11 21:00	162000	0.1	193.1	147.2				70.9	1.9	28	18.72
2006-07-11 22:00	165600	0.0	153.7	147.2	289.8	482.7	112.4	77.4	1.9	31	18.73
2006-07-11 23:00	169200	0.3	193.4	147.2				58.6	1.9	24	18.72
2006-07-12 0:00	172800	0.5	153.7	147.2	280.6	442.7	104.5	58.4	1.9	23	18.71
2006-07-12 1:00	176400	0.0	154.1	147.3				52.3	1.9	21	18.69
2006-07-12 2:00	180000	0.4	114.3	147.3	242.1	446.4	83.9	56.7	1.9	23	18.67
2006-07-12 3:00	183600	0.0	153.7	147.3				44.1	1.9	18	18.66
2006-07-12 4:00	187200	0.2	114.3	147.3	247.2	404.3	76.5	40.8	1.8	16	18.63
2006-07-12 5:00	190800	0.5	154.0	147.3				46.8	1.8	19	18.60
2006-07-12 6:00	194400	2.7	154.0	147.3	227.4	395.3	69.6	35.3	1.8	14	18.57
2006-07-12 7:00	198000	1.9	114.3	147.3				36.3	1.8	15	18.56
2006-07-12 8:00	201600	1.1	114.3	147.3		380.5	60.7	32.8	1.8	13	18.58
2006-07-12 9:00	205200	0.5	114.3	147.3				27.7	1.8	11	18.63
2006-07-12 10:00	208800	0.4	153.8	147.3	255.4	357.5	55.0	26.1	1.8	11	18.70
2006-07-12 11:00	212400	0.2	114.3	147.3				29.1	1.8	12	18.93
2006-07-12 12:00	216000	0.0	114.3	147.3	230.2	327.4	51.2	29.9	1.8	12	19.26
2006-07-12 13:00	219600	0.0	114.3	147.3				27.1	1.8	11	19.68
2006-07-12 14:00	223200	0.0	114.3	147.3	206.3	307.0	48.2	23.0	1.8	9	20.15
2006-07-12 15:00	226800	0.0	114.4	147.3				22.6	1.8	9	20.55
2006-07-12 16:00	230400	0.1	114.3	147.3	225.2	276.6	45.0	25.0	1.8	10	20.87
2006-07-12 17:00	234000	1.0	90.4	147.3				22.7	1.8	9	20.99
2006-07-12 18:00	237600	2.8	115.0	147.3	213.3	266.9	43.4	23.5	1.8	9	21.07
2006-07-12 19:00	241200	1.2	231.0	147.3				24.5	1.8	10	21.20
2006-07-12 20:00	244800	6.2	231.0	147.4	208.9		40.1	18.3	1.8	7	21.30

Date/time	Sec	Rain-fall (mm)	Total Inflow (CMS)	WSL (m)	Observed measurements					Modeling Input	
					G4 (m)	G3 (m)	G2 (m)	G1 (m)	Water depth at G2 (m)	SS (mg/l)	Tempera ture
2006-07-12 21:00	248400	6.3	351.0	147.4				23.4	1.8	9	21.4
2006-07-12 22:00	252000	2.0	551.2	147.5	199.5		40.4	44.4	1.8	18	21.3
2006-07-12 23:00	255600	0.5	634.1	147.7				119.4	1.8	48	21.4
2006-07-13 0:00	259200	0.0	353.9	147.7	199.5		246.9	329.5	1.8	132	21.3
2006-07-13 1:00	262800	0.0	435.6	147.8				434.8	1.8	174	20.5
2006-07-13 2:00	266400	0.0	355.5	147.9	208.7		296.8	387.0	1.8	155	20.0
2006-07-13 3:00	270000	0.0	356.1	147.9				380.5	1.8	152	19.8
2006-07-13 4:00	273600	0.0	275.4	148.0	196.7		419.8	380.1	1.8	152	19.5
2006-07-13 5:00	277200	0.0	194.1	148.0				341.5	1.8	137	19.1
2006-07-13 6:00	280800	0.0	153.3	148.0	200.8		375.8	247.0	1.8	99	18.8
2006-07-13 7:00	284400	0.0	153.4	148.0				191.3	1.8	77	18.7
2006-07-13 8:00	288000	0.1	194.2	148.0	197.8		344.4	166.2	1.8	67	18.7
2006-07-13 9:00	291600	0.0	153.5	148.0				147.5	1.8	59	19.0
2006-07-13 10:00	295200	0.0	153.8	148.0	184.9		248.0	96.0	1.8	38	19.2
2006-07-13 11:00	298800	0.0	317.4	148.1				85.1	2.1	34	19.6
2006-07-13 12:00	302400	0.0	153.9	148.1	178.1		180.1	77.5	2.0	31	19.9
2006-07-13 13:00	306000	0.0	235.9	148.1				64.5	2.0	26	20.3
2006-07-13 14:00	309600	0.0	153.9	148.1	163.2		135.3	76.3	2.0	31	20.6
2006-07-13 15:00	313200	0.0	112.8	148.1				60.5	2.0	24	21.0
2006-07-13 16:00	316800	0.0	153.9	148.2	159.6		109.5	56.7	2.0	23	21.2
2006-07-13 17:00	320400	0.0	153.9	148.2				50.8	1.9	20	21.6
2006-07-13 18:00	324000	0.3	153.9	148.2	151.2		91.0	45.5	1.9	18	21.8
2006-07-13 19:00	327600	0.4	153.9	148.2				43.8	1.9	18	21.8
2006-07-13 20:00	331200	0.0	112.8	148.2	150.0		81.2	38.9	1.9	16	21.9
2006-07-13 21:00	334800	0.0	153.9	148.2				41.2	1.9	17	21.9
2006-07-13 22:00	338400	0.2	112.8	148.2	162.8		71.4	38.0	1.9	15	21.9
2006-07-13 23:00	342000	0.0	112.9	148.2				41.8	1.8	17	21.9
2006-07-14 0:00	345600	0.0	112.9	148.2	158.5		62.4	35.8	1.8	14	21.9
2006-07-14 1:00	349200	0.0	112.9	148.2				32.4	1.8	13	21.9

Appendix Ⅱ

In this section, we explored the effect of the turbulent Schmidt (or Prandtl) number ($Sc_t = \nu_t / \Gamma_t$) on the dynamics of the gravity currents. In the numerical model of the gravity currents based on RANS equations and turbulence model (e.g. RNG $k-\varepsilon$), the turbulent diffusive fluxes of a scalar (Γ_t) were modeled with the help of the ratio of an eddy viscosity to the turbulent Schmidt number. The ratio of Γ_t and ν_t is generally reasonably constant although the ratio vary depending on the relationship between the shear and the buoyancy in stratified flows. The relationship in stratified flows can be characterized in terms of the gradient Richardson number (Ri) .

Based on the experimental data and numerical simulations, many researchers presented the value of the Sc_t ranged from 0.5-1.0 for neutrally stratified flows. For the stable stratified flows, the strength of stratification, however, influences the value of Sc_t. Elliott and Venayagamoorthy (2011) evaluated the turbulent Prandtl number as a function of the gradient Richardson number (Ri) using four different models (see Figure A.1).

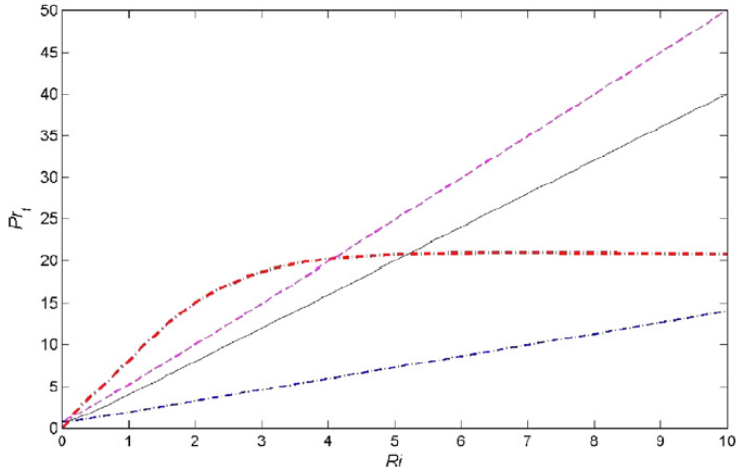

Figure A.1 The turbulent Prandtl number as a function of *Ri* using different models (From Elliott and Venayagamoorthy, 2011)

Figure A.1 presented the strong dependence of vertical turbulent diffusivity on the gradient Richardson number; it illustrates four different models in which an increase in the gradient Richardson number results in a decrease in the vertical turbulent diffusivities for scalars.

In order to investigate the effect of Sc_t on the propagation dynamics of gravity currents, we conducted the numerical simulations with the value of Sc_t in which it ranged from 0.2 to 50. Figure A.2 illustrates that the propagation speed of the gravity current, determined from the slope of the lines, decreases with decreasing Sc_t. The decreasing of the Schmidt number means increasing turbulent diffusivity leading to the density decrease in the gravity current (i.e. the loss of buoyancy, resulting in velocity decrease as shown in Figure A.2).

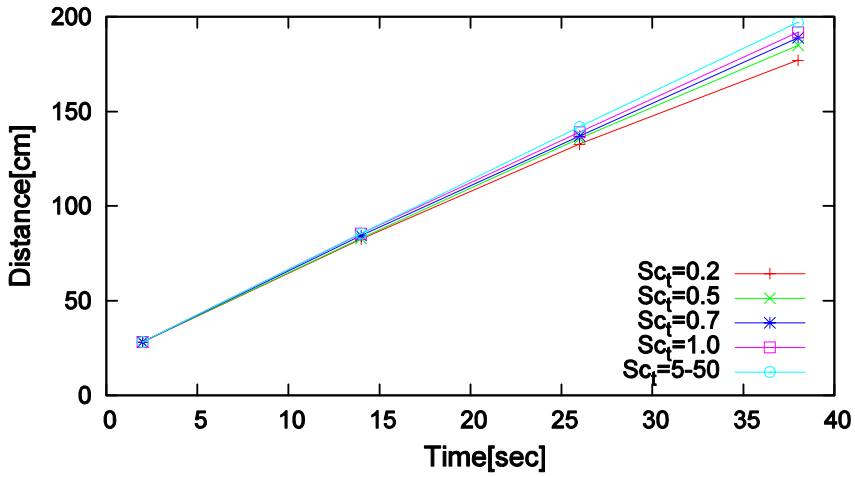

Figure A.2 Effect of Schmidt number on the traveling distance.

Figure A.3 provides the detailed information on the effect of the Sc_t on the turbulent mixing of in stratified fluids. No significant changes in density contour patterns were observed when the value of Sc_t was larger than 5. The simulations were compared with the experiments of Sutherland *et al.* (2004) to present the values of Sc_t that are most suitable for intrusive gravity currents. The value of 5 or larger than 5 was found as a suitable turbulent Schmidt number for the simulation of intrusive gravity currents.

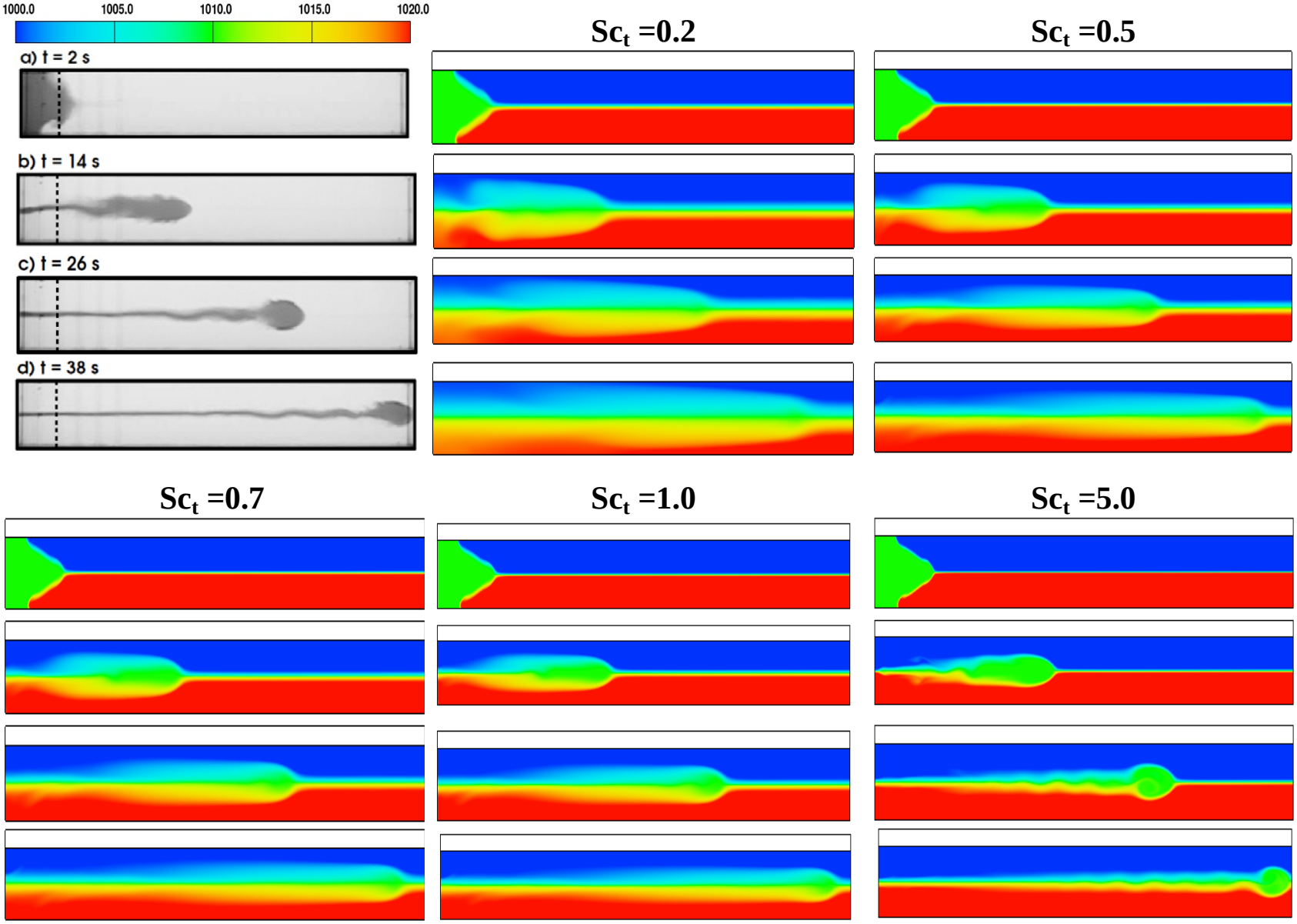
1000.0
1005.0
1010.0
1015.0
1020.0
a) t = 2 s
b) t = 14 s
c) t = 26 s
d) t = 38 s
Sc$_t$ =0.2
Sc$_t$ =0.5
Sc$_t$ =0.7
Sc$_t$ =1.0
Sc$_t$ =5.0

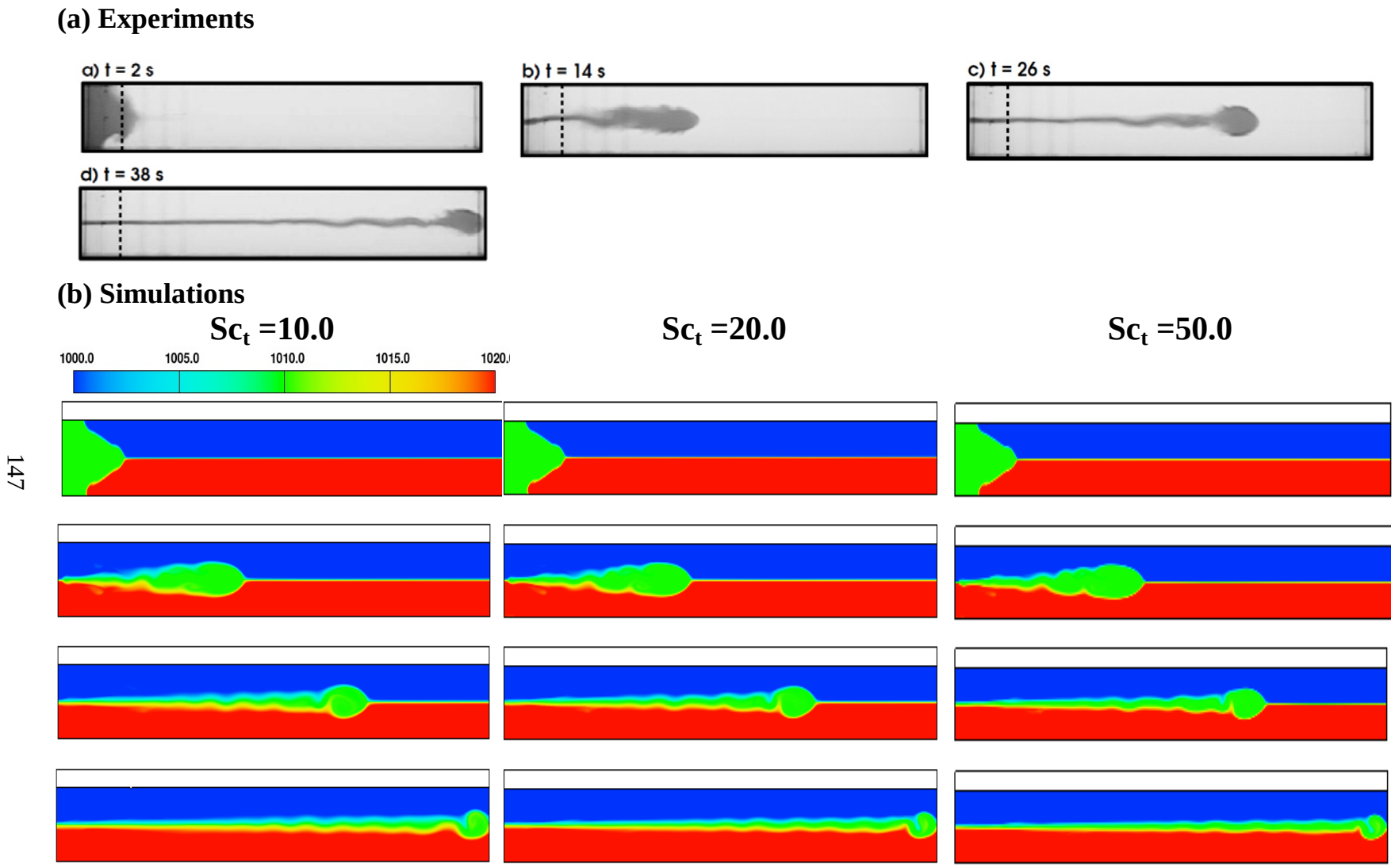

Figure A.3 Snapshots of intrusive gravity currents in numerical simulations with changing the Schmidt numbers. (a) The images taken for the laboratory experiments (Sutherland et al ,2004) ; (b) Simulation results.

Appendix Ⅲ

We derive an analytical solution to estimate the intrusive speed of turbid density currents propagating into a reservoir. It is assumed that the inflow and reservoir width are constant. The equations consist of the continuity equation and an empirical solution. The solution of these equations presents the celerity and height of intrusive density currents entering into a reservoir. The effects of a reservoir storage and the reduced gravity are reflected by changes in the intrusive celerity and height of gravity currents as they propagate from a reservoir inlet to a dam wall.

The continuity relationship defining the conservation of fluid mass:

$$\frac{\partial Q_d}{\partial A} + \frac{\partial A_d}{\partial t} = 0 \tag{A.1}$$

where Q_d is the inflow of a density current and A_d is the cross sectional area of a density current.

When considering conservation mass in a one-dimensional reservoir (see Figure A.4) with a constant width. Equations (A.1) can be written as

$$\frac{Q_d - Q_2}{L} = W\frac{dh}{dt} \tag{A.2}$$

$$Q_d = Wh_dU_d = LW\frac{dh}{dt} \tag{A.3}$$

where Q_d is the inflow of a density current and Q_2 is the discharge at a dam. W is the width of a reservoir. h_d is the depth of a density current and L is the length of a reservoir. $\Delta h / \Delta t$ indicates the rate of change of reservoir surface elevation during a flood event. C is a coefficient ($C \approx 0.8 - 1.0$).

The propagation speed can be defined as a general form:

$$U_d = C\sqrt{g' h_d} \tag{A.4}$$

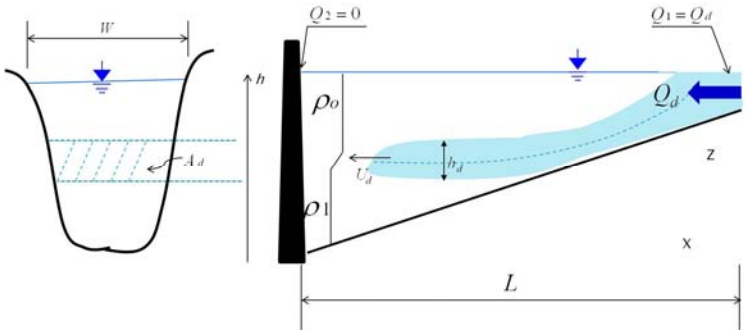

Figure A.4 Sketch of 1-D continuity for a intrusive density current in a reservoir.

We obtain from Equation (A.3) that $U_d = \frac{L}{h_d}\frac{dh}{dt}$. Substituting this into Equation (A.4) yields

$$h_d = \left[\frac{L^2}{g'}\left(\frac{\Delta h}{\Delta t}\right)^2 \frac{1}{C^2}\right]^{1/3} \tag{A.5}$$

Benjamin (1968) found that the value of C that ranges from 1 to 0.5 when the h_d / H increases from 0 to 0.5 where H indicates total water depth. Keulegan (1957) suggested that C= 0.76. Middleton (1996a) performed experiments on density currents formed by plastic beads and salt solution and proposed that C = 0.75. Numerical simulations are carried out for intrusive density currents propagating horizontally into a reservoir with a unit width. We investigate the effect of unit discharge q and excess density $\Delta\rho / \rho$ on the C . Figure A.5 shows that the value of C approaches to 0.8 as the inflow increases.

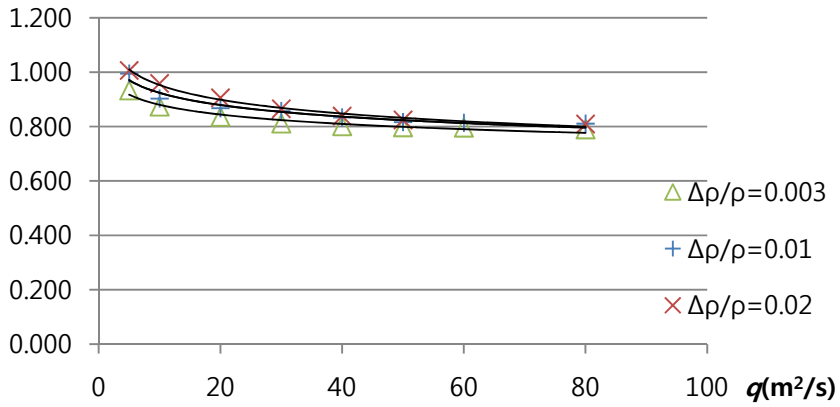

Figure A.5 Variation of C with inflow discharge Q and excess density $\Delta\rho / \rho$.

Those relationships (Equation A.4 and A.5) are very useful in the prediction of the celerity and intrusion height of intrusive turbid density currents. We estimated the celerity and height of the turbid density current propagating into Imha Reservoir during Typhoon Ewiniar using the analytical solutions. Table A.1 shows that the analytical solution provides a good prediction of the celerity of intrusive turbid density currents in Imha Reservoir.

Table A.1 Average celerity traveling from G2 to G4 (18 km), computed using the analytical solution.

	Distance	C	Average celerity	Intrusion height at G4
Field measurement	18000 (G2 to G4)	-	0.23 m/s	10-15 m
Analytical solution	30000 m (Reservoir length)	from Figure A.5 C = 0.8	0.31 m/s	11.6 m
		Benjamin (1968) C = 0.7	0.28 m/s	12.7 m
		Kao (1977) C = 1.0	0.19 m/s	18.6 m

1) Benjamin (1968)

Considering the energy-conserving flow, he obtained the formula predicting the propagation velocity as a function of the fractional depth (h_d / H).

$$C = \frac{U_d}{\sqrt{g' h_d}} = \frac{1}{\sqrt{2}} \left(\frac{(H - h_d)(2H - h_d)}{H(H + h_d)} \right)^{1/2} \tag{A.6}$$

where $g' = 0.5 g(\rho_1 - \rho_o)/\rho_0$. ρ_1 = 999.95 kg/m^3 at 6 ^{o}C (hypolimnion) and ρ_o = 997.30 kg/m^3 at 24 ^{o}C (epilimnion). Therefore $g' = 0.013$ m/s^2. When $h_d / H = 10\text{m}/36\text{m} = 0.28$, $C = 0.7$ from Equation (A.6). We finally obtain from Equation (A.4) and (A.5) that

$$h_d = \left[\frac{L^2}{g'} \left(\frac{\Delta h}{\Delta t} \right)^2 \frac{1}{C^2} \right]^{1/3} = \left[\frac{30000^2}{0.013} (0.00012)^2 \frac{1}{0.7^2} \right]^{1/3} = 12.7 \text{ m} \quad \text{and}$$

$$U_d = C\sqrt{g' h_d} = 0.7\sqrt{0.013 \times 12.7} = 0.28 \text{ m/s}.$$

2) Kao (1977)

Kao (1977) derived the front propagating speed along a sharp interface between two homogeneous fluids on the basis of the Bernoulli theorem, given by

$$U_d = \sqrt{2\frac{\rho_1 - \rho_d}{\rho_d}\frac{\rho_d - \rho_o}{\rho_1 - \rho_o} g\, h_d} \qquad \text{(A.7)}$$

where ρ_1 = 999.95 kg/m^3 at 6 ^{o}C (hypolimnion) and ρ_o = 997.30 kg/m^3 at 24 ^{o}C (epilimnion). ρ_d =999.40 kg/m^3. Here, $g' = 2\frac{\rho_1 - \rho_d}{\rho_d}\frac{\rho_d - \rho_o}{\rho_1 - \rho_o} g = 2\frac{999.95 - 999.4}{999.4}\frac{999.4 - 997.3}{999.95 - 997.3} 9.81 = 0.002$

Therefore, we obtain from Equation (A.4) and (A.5) that

$$h_d = \left[\frac{L^2}{g'}\left(\frac{\Delta h}{\Delta t}\right)^2 \frac{1}{C^2}\right]^{1/3} = \left[\frac{30000^2}{0.002}(0.00012)^2 \frac{1}{1.00^2}\right]^{1/3} = 18.6\text{m} \quad \text{and}$$

$$U_d = C\sqrt{g' h_d} = 1.0\sqrt{0.002 \times 18.6} = 0.19\,\text{m/s}.$$

3) From Figure A.5 (based on the numerical simulations)

We employed $C = 0.8$. We finally obtain from Equation (A.4) and (A.5) that

$$h_d = \left[\frac{L^2}{g'}\left(\frac{\Delta h}{\Delta t}\right)^2 \frac{1}{C^2}\right]^{1/3} = \left[\frac{30000^2}{0.013}(0.00012)^2 \frac{1}{0.8^2}\right]^{1/3} = 11.6\,\text{m} \quad \text{and}$$

$$U_d = C\sqrt{g' h_d} = 0.8\sqrt{0.013 \times 11.6} = 0.31\,\text{m/s}.$$

We approximately estimate the rate of sediment transport by the turbid density current during Typhoon Ewiniar. If the average width and C_v of the density currents assumed to be W_d = 500 m and $C_v = 0.0002$ or $C = 500\,\text{mg}/l$, the discharge of the density currents is $Q_d = U_d\, h_d\, W$ $= 0.23 \times 10 \times 500 = 1{,}150\,\text{m}^3/\text{s}$ and that of sediment $Q_{sd} = Q_d\, C_v = 0.23$ m^3/s ,which is approximately identical to a sediment transport rate of 50,000 tons/day. This sediment transport rate 50,000 tons/day estimated during Ewiniar is nearly equal to 45,300 tons/day during Typhoon Maemi in 2003, presented by Lee and Cho (2004).